Modelization of the interactions between turbine and sediment transport, using the Blade Element Momentum Theory

Fatima Khaled

Normandie Université

THÈSE

Pour obtenir le diplôme de doctorat

Spécialité MECANIQUE DES FLUIDES, ENERGETIQUE, THERMIQUE, COMBUSTION, ACOUSTIQUE

Préparée au sein de l'Université de Caen Normandie

Modelization of the interactions between turbine and sediment transport, using the Blade Element Momentum Theory

Présentée et soutenue par
FATIMA KHALED

Thèse soutenue le 30/08/2021 devant le jury composé de		
MME SANDRINE AUBRUN	Professeur des universités, École Centrale de Nantes	Rapporteur du jury
M. JULIEN CHAUCHAT	Maître de conférences HDR, Université Grenoble Alpes	Rapporteur du jury
M. FERHAT HADRI	Maître de conférences, Université de Versailles Saint-Quentin	Membre du jury
M. ABDELLATIF OUAHSINE	Professeur des universités, Univ Technologique de Compiegne - UTC	Membre du jury
M. NICOLAS GOURDAIN	Professeur des universités, ISAE-SUPAERO	Président du jury
M. YANN MEAR	Professeur des universités, INTECHMER Cherbourg	Directeur de thèse
M. SYLVAIN GUILLOU	Professeur des universités, Université Caen Normandie	Co-directeur de thèse

Thèse dirigée par YANN MEAR et SYLVAIN GUILLOU, Laboratoire universitaire des sciences appliquées de cherbourg (Caen)

UNIVERSITÉ CAEN NORMANDIE

ED 591 PSIME

LUSAC

Cette thèse a été effectuée en collaboration avec le Laboratoire d'Ingénierie des Systèmes de Versailles et le Laboratoire Universitaire des Sciences Appliquées de Cherbourg.

et a été financée par l'Université de Caen et le Conseil Départemental de la Manche.

Les calculs ont été réalisé sur le serveur Myria du Centre Regional Informatique et d'Applications Numeriques de Normandie (CRIANN).

à ma belle rose Rose,

Remerciements

Ce travail est le fruit d'une collaboration entre le Laboratoire Universitaire des Sciences Appliquées de Cherbourg (LUSAC) et le Laboratoire d'Ingénierie des Systèmes de Versailles (LISV). Il a été financé d'abord par l'Etat libanais puis par l'Université de Caen et le Conseil Départemental de la Manche. Tout au long de mon travail de la thèse, j'ai reçu beaucoup de soutien et d'assistance.

Je voudrais tout d'abord remercier mon premier directeur de thèse, le professeur Yann Méar du Cnam Intechmer, dont l'expertise a été inestimable dans les démarches administratives et les questions de recherche. Merci pour vos encouragements et vos commentaires perspicaces qui m'ont poussé à aiguiser ma réflexion et à amener mon travail à un niveau supérieur.

Quant à mon deuxième directeur, le professeur Sylvain Guillou du LUSAC, je tiens à le remercier très sincèrement et de tout mon coeur pour son soutien patient et ses expériences non seulement scientifiques dans la méthodologie de la thèse mais aussi sociales. Je vous remercie pour votre encadrement de qualité et votre suivi continu durant mon travail aussi votre encouragement lors des chutes. Votre comportement modeste avec vos thésards rend le travail avec vous très intéressant et excitant.

Je tiens à remercier également mon encadrant, le maitre de conférences Ferhat Hadri au LISV, pour son effort et ses aides au début de la thèse et son encouragement continu durant mon travail.

Merci à l'équipe de CRIANN-Myria pour nous fournir l'opportunité de réaliser nos simulations en très bonnes conditions (mémoire, CPU...) merci aussi pour leur service et leur réponse immédiate à nos questions.

Je remercie particulièrement Madame Alina Santa Cruz, maitre de conférence au LUSAC pour son acceuil précieux lors de mon arrivée à Cherbourg, merci également à Madame Frédérique Guillou pour sa présence impressionnante. L'ambiance au labo LUSAC fut amicale et motivante en raison de la présence de mes collègues Lydia, Philippe, Paul, Nasteho, Hai-Yen ...

Enfin, je remercie profondément mon père Ahmad et ma mère Badrié, mes soeurs et mes frères en particulier Rossy, pour leurs conseils avisés et leur écoute attentive. Vous

êtes toujours là pour moi. Un merci très particulier est dédié à ma petite famille, mon mari Ahmad et ma fille Rose, je n'aurais pas pu terminer cette thèse sans votre soutien. J'embrasse tous les gens qui ont fourni de bonnes conditions pour finir ma thèse. Gros bisous à Amjoudi!

Contents

1 Introduction **1**

1.1 On the need of Energy . . . 1
1.2 Renewable energy . . . 2
1.2.1 Overview . . . 2
1.2.2 Types of Renewable energy . . . 2
1.2.3 Marine Renewable Energy (MRE) . . . 3
1.2.4 Energy of Rivers . . . 4
1.3 Hydrokinetic turbines . . . 6
1.3.1 Some manufactured stream turbines . . . 6
1.3.1.1 Tidal turbines . . . 6
1.3.1.2 River turbines . . . 8
1.4 Interactions with environment . . . 9
1.4.1 Wake effects . . . 10
1.4.1.1 Interaction with ambient turbulence . . . 11
1.4.1.2 Turbine-turbine interaction, effects of confinement between turbines . . . 13
1.4.2 Turbine-sediment interaction . . . 15
1.4.2.1 Definition of the sediments . . . 16
1.4.2.2 Modes of transport of sediments . . . 16
1.5 Modeling of interaction turbine-sediments . . . 20
1.5.1 State of art . . . 20
1.6 Aim of the thesis . . . 26

2 Modeling of transport of sediments **27**

2.1 Introduction . . . 27
2.2 Mathematical formulation . . . 27
2.2.1 Turbulence averaged two phase flow . . . 27
2.2.2 Fluid phase shear stress . . . 29
2.2.2.1 Mixture viscosity . . . 30

2.2.2.2 Turbulence modeling . . . 30
2.2.3 Particle phase stress . . . 32
2.2.3.1 Kinetic theory for granular flow . . . 33
2.2.3.2 Dense granular flow rheology . . . 34
2.3 Numerical Implementation . . . 36
2.3.1 Model validation. . . . 37
2.4 Summary . . . 39

3 Modeling of the turbine **41**
3.1 Introduction . . . 41
3.2 Hydrodynamic models . . . 41
3.2.1 Actuator Disk . . . 41
3.2.2 Blade Element Momentum Theory . . . 45
3.2.2.1 Blade Element Theory . . . 45
3.2.2.2 Momentum Theory on each blade element . . . 47
3.3 Numerical implementation in OpenFOAM . . . 48
3.3.1 Overview of RANS solvers in OpenFOAM . . . 49
3.3.2 RotorDiskSource . . . 51
3.3.3 Modifications in rotorDiskSource . . . 53
3.4 Validation . . . 54
3.4.1 Experimental Setup . . . 54
3.4.2 Numerical Setup . . . 57
3.4.3 Validation result . . . 59
3.5 Coupling BEMT with two-phase model . . . 63
3.6 Summary . . . 63

4 Local scour near an axial-flow turbine **65**
4.1 Introduction . . . 65
4.2 Experimental setup . . . 66
4.3 Numerical setup . . . 66
4.4 Effects of different turbine's modeling on bed pattern . . . 69
4.4.1 Temporal Evolution of the local scour . . . 69
4.4.2 Morphodynamic impact of the turbine . . . 72
4.4.2.1 Effects of different turbine models on turbine's wake . . . 73
4.5 Summary . . . 77

5 Blockage Effects on turbine-sediments interactions **79**
5.1 Scour-Sensitivity to channel width configurations . . . 80

5.1.1 Computational mesh . . . 81
5.1.2 Boundary conditions . . . 81
5.2 Results . . . 82
5.2.1 Impact of the turbine on the bottom topography with comparison to baseline conditions . . . 83
5.2.2 Temporal evolution . . . 84
5.2.3 Spatial evolution . . . 87
5.3 On the existence of a limit in this behavior . . . 93
5.3.1 Temporal evolution . . . 94
5.3.2 Spatial evolution . . . 96
5.4 Summary . . . 99

6 Interaction between hydrokinetic turbines and large scale bedforms 101
6.1 Introduction . . . 101
6.2 Numerical Setup . . . 101
6.2.1 Computational mesh . . . 102
6.2.2 Boundary Conditions . . . 102
6.3 Results . . . 103
6.3.1 Wake characterization . . . 103
6.3.2 Turbines-sediments interaction . . . 106
6.4 Summary . . . 118

7 Conclusions and perspectives 119
7.1 Le besoin d'énergie . . . 133
7.2 Energies renouvelables . . . 134
7.2.1 Types des énergies renouvelables . . . 134
7.2.2 Énergie marine renouvelable (EMR) . . . 134
7.2.3 Energie des rivières . . . 135
7.3 Turbines hydrocinétiques . . . 135
7.4 Interactions avec l'environnement . . . 135
7.4.1 Interaction turbine-sédiment . . . 135
7.4.2 État de l'art . . . 136
7.5 Objectif de la thèse . . . 136
7.6 Méthodologie . . . 137
7.6.1 Modèle multiphasique Euler-Euler . . . 137
7.6.2 Modèles Hydrodynamiques : BEMT et AD . . . 139
7.6.2.1 La théorie du disque d'action AD . . . 139
7.6.2.2 La théorie des éléments des pales BEMT . . . 140

7.6.3 Implémentation numérique des modèles et validation. 140
7.6.3.1 Modèle diphasique 140
7.6.3.2 Modèle hydrodynamique 141
7.6.3.3 Couplage entre les deux modèles 141
7.7 Effets du confinement sur l'interaction turbine/fond sédimentaire 142
7.8 Effet de la distance inter-turbines sur l'évolution du fond sableux 142
7.9 Conclusion générale et perspectives. 143

List of Figures

1.1 Consumption-based CO_2 in the world by 2018 (Rabain, 2019). 2

1.2 Primary energy consumption rate per type in 2019 by SDES. TOTAL: 2893 TWh, and 339 TWh for RE (REN21). 3

1.3 European tidal potential according to the variation of the tidal currents (in dark red: high currents) (AQUARET). 4

1.4 Location and distribution of rivers in France (The rivers in red have a module greater than 100 m3/s) (EDF). 5

1.5 Horizontal and vertical axis hydrokinetic turbines (Ladokun et al., 2018). 6

1.6 Four hydrokinetic vertical turbines in the Rhone (HydroQuest). 8

1.7 Interactions between stressors and receptors, like changes in water surface processes, underwater noise, electromagnetic fields, mooring process, collision risk, and changes in habitats (Shields, 1936). 9

1.8 Definition of wake characteristics (Nicholas and P.E., 2016). 11

1.9 Representation of the marine and fluvial conditions where horizontal axis hydrokinetic turbines operate in (Ouro, 2017). 12

1.10 Axial velocity contouring (top): downstream the second turbine with inter distance of $4d$, at $TSR = 3.67$ and $U_\infty = 0.8m/s$ for $I_\infty = 3\%$ (left) and $I_\infty = 15\%$ (right); (down): downstream the single turbine at $TSR = 3.67$ and $U_\infty = 0.8m/s$ for $I_\infty = 3\%$ (left) and $I_\infty = 15\%$ (right). 14

1.11 Schematic of the hydrodynamics of an array of tidal turbines (Ouro et al., 2019). 15

17figure.caption.20

18figure.caption.21

1.14 Top view of a river (left), 1: original path of stream water, 2: modified path of stream water due to sediment transport, 3: scouring and erosion, 4: deposition term; Parallel view of a river showing 1: water, 2: mobile sediments, 3: fixed bottom, v: flow velocity, Q: flow rate, h: depth of water, h_s: thickness of bed-load [2]. 18

1.15 Three different modes of transport (https://www.gunt.de/). 19

1.16 Photo of single turbine with bedforms during experiments of Hill et al. (2015). 22

1.17 Final topography for the clear water experiments (left): single (top), $4d$ (middle), and $7d$ (bottom). Color scale represents normalized scour (dark colors) and deposition (light colors). Final topography for the live bed experiments (right): single (top), $4d$ (middle), and $7d$ (bottom). Flow is from left to right (Hill et al., 2015). 22

2.1 Sediment concentration contour at different times during the scour process using a $k-\omega$ turbulence model and the granular rheology (Chauchat et al., 2017). 37

2.2 Sediment bed profiles at 11s using a $k-\epsilon$ turbulence model (Chauchat et al., 2017). 38

3.1 Stream tube passing through a turbine represented by an actuator disk. . . 42

3.2 Power and drag coefficients in function of the induction factor a. 44

3.3 Flow velocities and forces acting on the blade by BEMT.$V = V_{axial}(1-a)$, V_θ are the axial and tangential velocity components, β is the blade twist angle, α the angle of attack, ϕ the inflow angle. 47

50figure.caption.34

51figure.caption.35

3.6 Photograph of the IFREMER tunnel and honeycomb for adjusting the turbulence intensity rate (Maganga, 2011). 54

3.7 Experimental turbine used in the IFREMER experiments (Mycek et al., 2014). 57

3.8 Initial state and position of the disc in the channel. 58

3.9 Mesh configuration of the disc using structured hexahedral cells. 58

3.10 Variation of Power coefficient in function of TSR factor. 59

3.11 Map of the (up): dimensionless axial velocity downstream the turbine in the wake and of the (down): axial turbulence intensity I_{2d} downstream the turbine in the wake for TSR = 3.67. 60

3.12 Vertical profiles of the axial velocity dimensionless by the fluid velocity (U_x/U_∞), downstream the turbine; blue for numerical BEMT results and red for the measurements of Mycek et al. (2014). 61

3.13 Vertical profiles of the mean turbulence intensity I_2d, downstream the turbine; blue for numerical BEMT results and red for the measurements of Mycek et al. (2014). 62

4.1 Photo of the model and the instrumentation used in the experiments of Hill et al. (2015). 66
4.2 Initial state of the domain, position of the disc at $3m$ from the inlet and the sheet layer of sands on the bottom (grey color). 67
4.3 Computed contours of bed elevations relative to the initial flat bed at different time instants for Blade Element Momentum Theory. 70
4.4 Computed contours of bed elevations relative to the initial flat bed at different time instants for Actuator disk theory. 71
4.5 Comparison of computed time series of bed elevation relative to the initial flat bed at $0.1d$ downstream from the rotor and at (a) z = 0, (b) z = $0.2d$, (c) $z = 0.4d$ and (d) $z = 0.6d$ (turbine is located at $z = 0$ in the spanwise direction): measurements by Hill et al. (2015) (triangle); multiphase Euler-Euler with BEMT (black circle); multiphase Euler-Euler with AD (red circle); LES by Yang et al. (2017) (square). 72
4.6 Comparison of computed cross-sections contours of bed elevations y/d (a,b) and shear stress τ_{yz}, between $BEMT$ and AD theories at $t = 3$ min. 73
4.7 Comparison of computed vertical profiles of axial velocity between AD and BEMT at $1d, 3d, 5d, 7d$ and $9d$ turbine downstream locations. 74
4.8 Comparison of computed vertical profiles of transverse velocity between AD and BEMT at $1d, 3d, 5d, 7d$ and $9D$ turbine downstream locations. . . 75
4.9 Axial profiles of streamwise velocity for (a) Actuator Disk Theory and (b) Blade Element Momentum Theory at $t = 3$ min. 76
4.10 Velocity field in the (y,z) plans colored by the fluid vorticity at $t = 3$ min for BEMT (a) under the turbine and (b) $1d$ from the turbine location. . . . 76

5.1 Initial state of domain, position of the disc and the sheet layer of sands on the bottom (red color) and the three cross-sections (dashed-white lines) used for the configurations, a, b and c are the length, depth and width of the hydrodynamic channel respectively. 82
5.2 Normalized elevations of the bottom (y/d) for baseline case (right) and in the presence of the turbine (left) for configuration A. (a,b) $t = 0$ s, (c,d) t = 40 s (e,f) $t = 60$ s. 83
5.3 Normalized elevations of the bottom (y/d) for baseline case (right) and in the presence of the turbine (left) for configuration B. (a,b) $t = 0$ s, (c,d) t = 40 s (e,f) $t = 60$ s. 84
5.4 Temporal evolution of normalized bed elevation (y/d) with and without the turbine at (a,c) S_1 and (b,d) S_2 respectively for A (upper) and for B (lower). 85

5.5 Temporal evolution of bed shear stress with and without the turbine at section (a,c) S_1, (b,d) S_2 respectively for A (upper) and B (lower). 86
5.6 Velocity field in the (y,z) plans colored by the fluid vorticity. 87
5.7 Spatial evolution of bed elevation with and without the turbine at (a,b) sections S_1 and S_2 on t = 40 s and (c,d) sections S_1 and S_2 on t = 100 s for configurations A (black) and B (blue). 88
5.8 Spatial evolution of shear stress (τ_{yz}) at (a,c) section S_1 and (b,d) section S_2 on t = 40 s (upper) and t = 100 s (lower) for configurations A (black) and B (blue). 89
5.9 Vertical profiles of velocity , normalized by the mean velocity of the fluid upstream the turbine, U_f at sections S_1 (a) and S_2 (b) for configurations A and B on t = 40 s. 89
5.10 ISO-contouring of the axial vorticity in cross sections areas S_1 (a) and S_2 (b) for configuration B on t = 40 s. 90
5.11 Cross sectional profiles at y = 0 m of (a,c) sediment concentration ϕ and (b,d) shear stress τ_{yz} at sections (a,b) S_1 and (c,d) S_2, on t = 40 s and 100 s. 91
5.12 Axial evolution of bed morphology y/d on the bottom of the channel with and without the turbine for configurations A and B on t = 40 s and t = 100 s. 92
5.13 Difference in dimensionless bed elevation between the baseline and turbine results on S_1 and S_2, the erosion is represented in negative values. (a): temporal evolution of ($\Delta y/d$), (b): spatial evolution of ($\Delta y/d$). . . . 92
5.14 ISO-contouring of the axial vorticity in cross section area S_1 for cases A (a) and B (b) at t = 40 s. 93
5.15 Position of the disk due to the different channel's widths of all configurations in cross-sections (see table 5.4). 94
5.16 Temporal evolution of normalized bed elevation (y/d) for all configurations under the turbine on S_1. 95
5.17 Maps of normalized bed elevation (y/d) for different six blockage ratios configurations; (a) 6d, (b) 5d, (c) 4d, (d) 2.5d, (e) 1.5d, (f) 1d. at t = 130 s. 96
5.18 Spatial evolution of bed elevation for the five configurations on a) S_1 and b) S_2 at t = 40 s. 97
5.19 Spatial evolution of shear stress (τ_{yz}) on a) S_1 and b) S_2 at t = 40 s. 97
5.20 ISO-contouring of the axial vorticity in cross sections areas S_1 (a) and S_2 (b) for all configurations. 98

6.1 Initial state of domain, position of the turbines (T_1 and T_2), logarithmic profile of the fluid velocity at inlet, the sheet layer of sands on the bottom (yellow color); d_i is the inter-turbines distance (see table 6.1). 103

6.2 Spatial evolution of bed elevation with the presence of two turbines apart with different d_i for configurations A_1 (a), A_2 (b), A_3 (c) and A_4 (d). . . . 104

6.3 Vertical profiles of velocity, normalized by the mean velocity of the fluid U_f upstream the turbines T_1 and T_2 for all configurations, at $0.2d$ (black), $1d$ (blue) and $2d$ (red), $7d$ (green). 105

6.4 ISO-contouring of the axial vorticity near the turbines T_1 and T_2 for all configurations, at $0.2d$, $1d$ and $2d$. 106

6.5 Normalized elevations of the bottom (y/d) with and without the turbines; (a) baseline case, (b) d_i = $4d$, (c) d_i = $7d$, (d) d_i = $10d$ and (e) d_i = $13d$ at 60 s. 108

6.6 Spatial evolution of bed shear stress with and without the turbines; (a) baseline case, (b) d_i = $4d$, (c) d_i = $7d$, (d) d_i = $10d$ and (e) d_i = $13d$ at 60 s. 109

6.7 Spatial evolution of bed shear stress in (y,z) plane below the two turbines for configurations A_1 (a,b), A_2 (c,d), A_3 (e,f) and A_4 (g,h). 110

6.8 Spatial evolution of the bed elevation at t = 60 s with the turbine (+) and without the turbine (-) at the cross sections of the turbine's position x' (a), x'' (b); (c) and (d): at $1d$ downstream T_1 and T_2 respectively; (e) and (f): at $2d$ downstream T_1 and T_2 respectively; black, blue, red and green colors correspond to the 4d, 7d, 10d and 13d configurations respectively. . 113

6.9 Spatial evolution of the shear stress (τ_{yz}) on t = 60 s with the turbine (+) and without the turbine (triangles) at the cross sections of the turbine's position x' (a), x'' (b); (c) and (d): at $1d$ downstream T_1 and T_2 respectively; (e) and (f): at $2d$ downstream T_1 and T_2 respectively; black, blue, red and green colors correspond to the 4d, 7d, 10d and 13d configurations respectively. 114

6.10 Spatial evolution of the shear stress (τ_{yz}) on t = 60 s near the second turbine T_2 (+) at the turbine's position $x' = 0d$ for all configurations. . . . 115

6.11 Spatial evolution of bed elevation with the presence of two turbines apart with different d_i for configurations A_1 (a), A_2 (b), A_3 (c) and A_4 (d). . . . 116

6.12 Dimensionless bed elevation along the axis of the channel for the four configurations; d_i = $4d$ (black plus), $7d$ (blue circle), $10d$ (red triangle) and $13d$ (green square) such as $X = (x - x_1)/d$ and x_1 = 1.5 cm. 117

6.13 Difference of the dimensionless axial bed elevation between the baseline conditions and the results of presence of the turbine for the four configurations; $d_i = 4d$ (black plus), $7d$ (blue circle), $10d$ (red triangle) and $13d$ (green square) such as $X = (x - x_1)/d$ and $x_1 = 1.5$ cm. 117

7.1 Schematic showing the interactions between dune generated turbulence and axial-flow hydrokinetic turbines (Hill et al., 2014). 121

7.2 Topography of seven turbine staggered array installed in migrating sand ripple topography ($d50$ = 0.42 mm) (Hill et al., 2014). 121

List of Tables

1.1 Examples of different hydrokinetic technologies. 7

3.1 List of standard OpenFOAM flow solvers 49
3.2 Detailed blade profile description implemented in rotorDiskSource. . . . 53
3.3 Detailed blade profile description. 55
3.4 Detailed blade profile description, $angle\ of\ attack\ (deg)$, c_d, c_l 56
3.5 Description of parameters used in Mycek et al. (2014) experiment; U_∞: flow velocity, TSR: Tip Speed Ratio (ω d/2U_∞), TI: Turbulence Intensity. 58

4.1 Numerical hydrodynamic properties for the configurations $A*$ and $B*$ where a, b, c are the dimensions of the channel, a is the domain length in the x-direction, b is the water depth and c is the length in y-direction. x' is the position of the turbine, TI is the turbulent intensity. 67
4.2 Numerical properties for the configurations $A*$ and $B*$ where s is the initial thickness of sand sheet and d_s is the mean sand diameter. Note that u_* is the bed friction velocity lower than the critical value to avoid the flow effect on the sediment transport. 68
4.3 Tip-Speed-Ratio values of the configurations $A*$ and $B*$. 68
4.4 Different models of sediment transport used in the simulations for configurations $A*$ and $B*$. 68

5.1 Numerical properties for configurations A and B where $c/2$ is the distance between the center of the turbine and the lateral edge of the channel. . . . 80
5.2 Numerical hydrodynamic properties for configurations A and B where x' is the position of the turbine from the inlet, d is the turbine's diameter, TI is the turbulent intensity, U_∞ is the mean upstream velocity of the fluid. Note that the Froude number is Fr = 0.466. 80
5.3 Numerical sediment properties for configurations A and B where ϕ is the initial volume fraction of the sediments, s is the initial thickness of sand sheet and d_s is the mean sand diameter. Note that the Froude number is Fr = 0.466. 81

5.4 Numerical properties for configurations A, B, C, D, E and F where $c/2$ is the distance between the center of the turbine and the lateral edge of the channel. 94

6.1 Numerical hydrodynamic properties for configurations A_1, A_2, A_3 and A_4 where a, b, c are the dimensions of the channel, x' is the position of the first turbine, TI is the turbulent intensity. 102

6.2 Numerical hydrodynamic properties for configurations A_1, A_2, A_3 and A_4 where x' and x'' are the position of the first and second turbine respectively from the inlet, d_i is the distance inter-turbines. 102

6.3 Summary of the boundary conditions implemented in the simulation of all configurations: zG = zeroGradient, iO = inletOutlet, fV = fixedValue, FP = fluxPressure, hP = hydrostatic pressure and logP = logarithmic profile. 103

6.4 Position of the cross sections near T_1 and T_2 for each configuration. . . . 111

Chapter 1

Introduction

1.1 On the need of Energy

The global population growth is estimated by the United Nations (UN), from 7.6 billion in 2017 to 9.7 billion by 2050 (UICN, 2014). Hence, electricity demand is growing about twice as fast as overall energy consumption and is expected to increase by more than half by 2040. The challenge to meet this growing demand, while preventing as much as possible the harmful emissions of greenhouse gases, is substantial. The carbon dioxide concentrations found in global atmosphere are increased nowadays 70% more than the average increase since 2010 due to the combustion of fossil fuels which contributes massively to a global warming. Then, the various models of the Intergovernmental Panel on Climate Change (IPCC) predict an increase in the global average surface temperature ranging from 1.5 to over 4°C till the end of the 21st century. The consequence is that the average sea level could exceed one metre in the beginning of the 22nd century, which may affect 270 million people living in coastal regions.

Along with the challenges of meeting growing demand and reducing greenhouse gas emissions, the population needs also a cleaner air. According to the World Health Organization (WHO), the dangers of polluted air are increasing, they estimate that around seven million people die prematurely from air pollution. The principle reasons are the industrial sources such as power generation and the harmful emissions from transport vehicles, that could be avoided also by the use of electricity.

Therefore, various governments pledged after the 2015 Paris Agreement, to tackle climate change issues and achieve sustainable development of such plans to decarbonise. The objective is to exploit an alternative source of energy to fossil fuels. The Nuclear energy could be a solution since it has a minor impact on global warming, but major concerns remain over the safety of power plants, the disposal of radioactive waste and its dependence on uranium resources.

In response to this situation, Renewable Energy (RE) is the forefront concern, a variety of types of RE are increasingly being used, they are produced locally, thus limiting dependence on imports from other countries, and creating jobs.

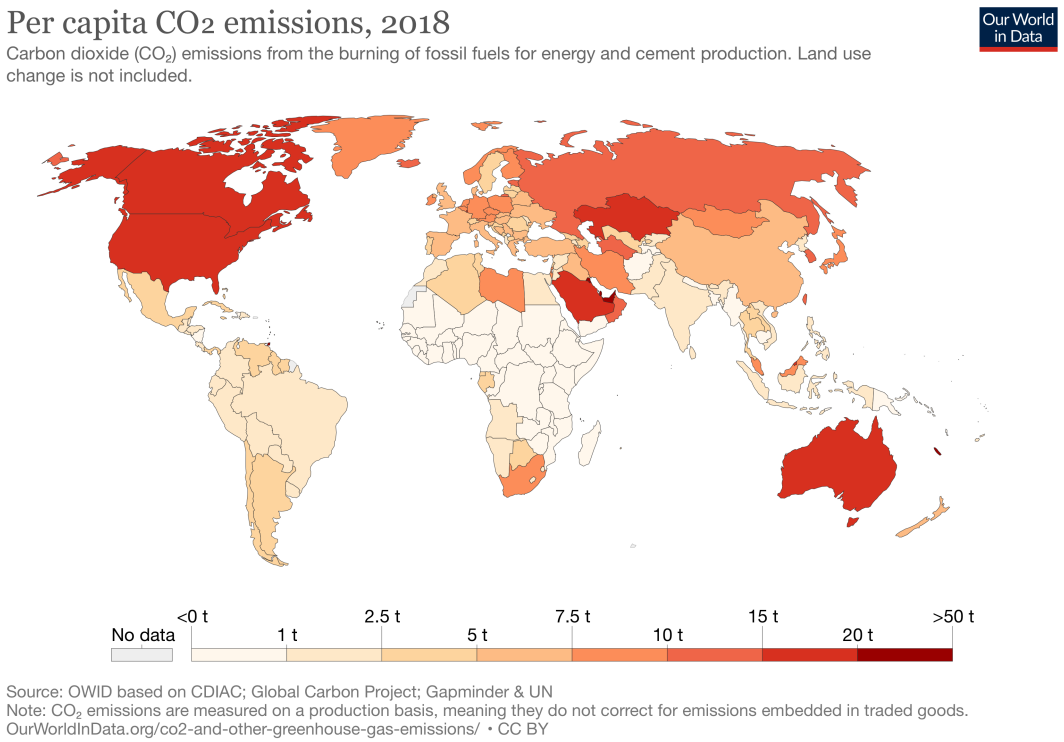

Fig. 1.1: Consumption-based CO_2 in the world by 2018 (Rabain, 2019).

1.2 Renewable energy

1.2.1 Overview

The Renewable Energies (RE) are derived from natural processes in perpetual renewal. Renewable energies represent 11.7% of primary energy consumption and 17.2% of gross final energy consumption in France in 2019 (fig. 1.2). These parts have been increasing steadily for the past ten years. The significant growth in the primary production of RE since 2005 ($+72\%$) is mainly due to the rise of biofuels, heat pumps and the wind industry. France has therefore undertaken to reduce its greenhouse gas emissions by a factor of four by 2050 and increase the RE production to 40% in 2030.

1.2.2 Types of Renewable energy

There are several forms of RE, including energy generated by the sun (photovoltaic or thermal), wind (wind power), water from rivers and oceans (hydro power), biomass

which is solid (wood and waste of biological origin), liquid (biofuels) or gas (biogas) as well as the heat of the earth (geothermal energy). Purely electric renewable energies include hydrokinetic energy, wind energy and solar photovoltaic.

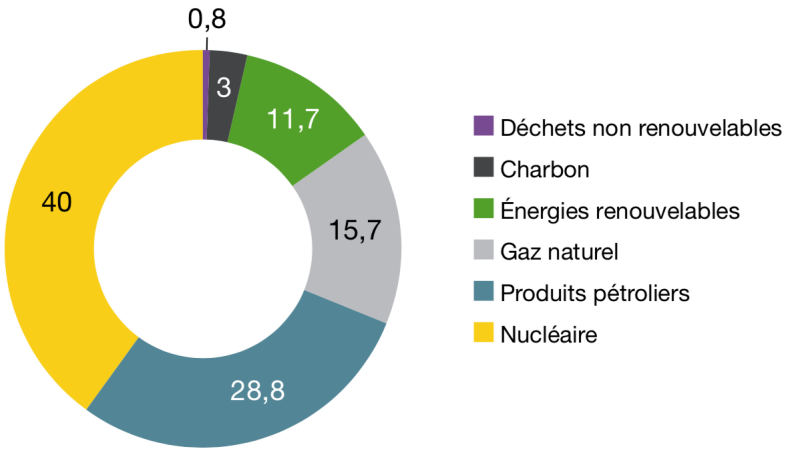

Fig. 1.2: Primary energy consumption rate per type in 2019 by SDES. TOTAL: 2893 TWh, and 339 TWh for RE (REN21).

Wind power generation has steadily increased since it started in the last decades. In 2019, the gross generation increased to 34.6 TWh, up of 21% compared to 2018. This sharp increase is due to a very favorable weather conditions in 2019. The size of the installations is quite diverse, as they can vary from a micro-wind turbine of some kW to a farm of turbines with a power in order of MW (Rabain, 2019).

With more than 2000 installations, France is, along with Sweden, one of the main producers of hydropower in the European Union. In 2019, hydropower represented 51% of gross renewable electricity production in France. Marine and Fluvial Renewable Energies represent the major in hydropower sector, due to their several advantages presented in the next section.

1.2.3 Marine Renewable Energy (MRE)

The potential energy of the oceans is significant. Indeed, on a global scale, the oceans cover 71% of the planet. As a locally derived energy source, MRE generated from waves, tides, and rivers is more predictable, consistent, and continuous than either wind or solar power.

The deployment of renewable marine energies on a large scale, in France, is essential to the achievement of the objective of 5.2 to 6.2 GW of MRE in 2028 (the other European countries have already installed more than 23 GW in 2020).

Various systems have been developed to harness this energy. Some techniques are currently in use, others are still being investigated or tested. Current turbines are sub-

merged or semi-submerged in the water, they are moved by the kinetic energy of the high currents. As each of these systems requires very specific physical conditions, there are several types of sources in the oceans. Within the European Union, offshore wind farms currently supply 0.3% of total electricity demand: according to the European Wind Energy Association's (EWEA) Oceans of Opportunity report, this could reach 16% by 2030. The potential development is therefore enormous.

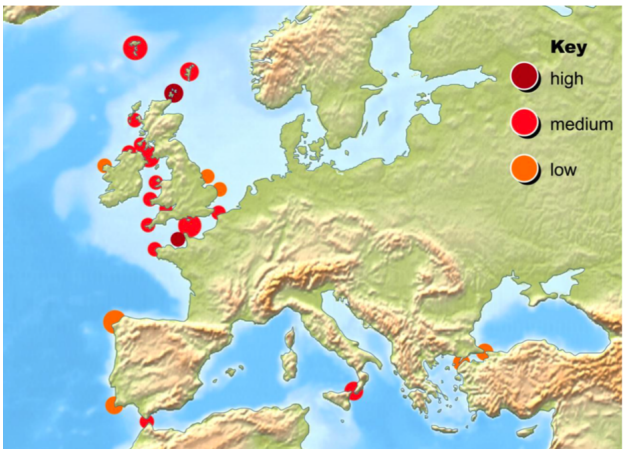

Fig. 1.3: European tidal potential according to the variation of the tidal currents (in dark red: high currents) (AQUARET).

Globally, the kinetic power of the technologically exploitable tidal currents is estimated between 75 and 100 GW in the shallow coastal waters bordering Canada, Brazil, New Zealand and northern Europe. At the North European continental shelf, the United Kingdom and France have the most important site of the exploitable tidal power resource, it is estimated at 11 GW. France represents 20% of this potential (fig. 1.3), it includes a fraction of one of the largest deposits in Europe, the Alderney Race ("Raz Blanchard" in French). It capitalizes 75 of the national potential resource, it is located in the centre of the English channel with a current velocity greater than $5m/s$ in medium spring water conditions (fig. 1.3). The Race of Fromveur is the second French tidal stream potential with a current velocity greater than $4m/s$. It is followed by the Paimpol Bréhat site, in the Côtes d'Armor region of Brittany which has been undergoing field tests since the summer of 2012.

1.2.4 Energy of Rivers

Global fluvial energy potential is around 50 GW. The French potential is at least of 254 MW and is located mainly in Brittany, in Pays de la Loire, New Aquitaine and on the Rhône.

The necessary conditions to install hydrokinetic turbines in rivers are a water velocity greater than $1.5m/s$ and a water depth greater than one meter. To benefit from the series effect (significant energy production and reduction in manufacturing costs), the objective is to install parks of several machines, sometimes several hundred machines and consequently for rivers with large sections and high currents. The module, used to determine approximately the discharge, corresponds to the summary of the average annual flow of a river over a reference period, typically ten years. Rivers with module greater than 100 m3/s considered to be the most interesting area for installing the hydrokinetic turbines. Figure 1.4 is a map of French rivers with those with a modulus greater than $100m3/s$ colored in red. In France, many rivers have interesting characteristics for the installation of hydrokinetic turbines.

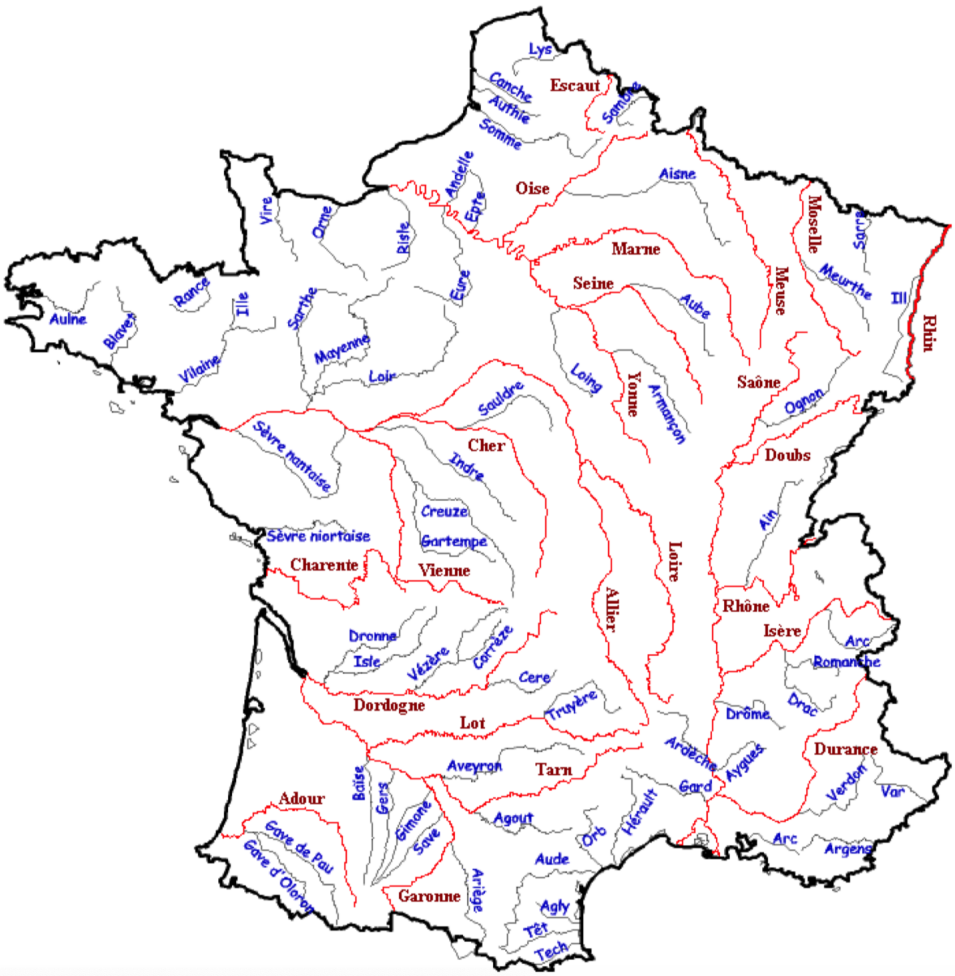

Fig. 1.4: Location and distribution of rivers in France (The rivers in red have a module greater than 100 m3/s) (EDF).

1.3 Hydrokinetic turbines

The operation of an hydrokinetic turbine is based on a principle similar to wind turbines. Where the latter capture the kinetic energy of the wind, hydrokinetic turbines use the same process to harness the kinetic energy of streams, like tidal currents and rivers. Since the density of water is 800 times higher than that of air, turbines installed in high-current areas are smaller in size than wind turbines of the same power.

The turbine receives the energy of the stream and transforms it into mechanical movement which is converted into electrical energy. Systems can stay afloat with an anchor point, or be placed below the surface. This then passes through the connection of a given electrical network. Depending on needs and installation capacities, it is thus possible to adapt the size of the turbines. They can be micro-generators for small rivers, or even generators capable of producing several megawatts for sites where the current is particularly important, such as in high current rivers or in tidal currents sites. They can take different forms: vertical or horizontal axis turbines (fig. 1.5), but also oscillating devices.

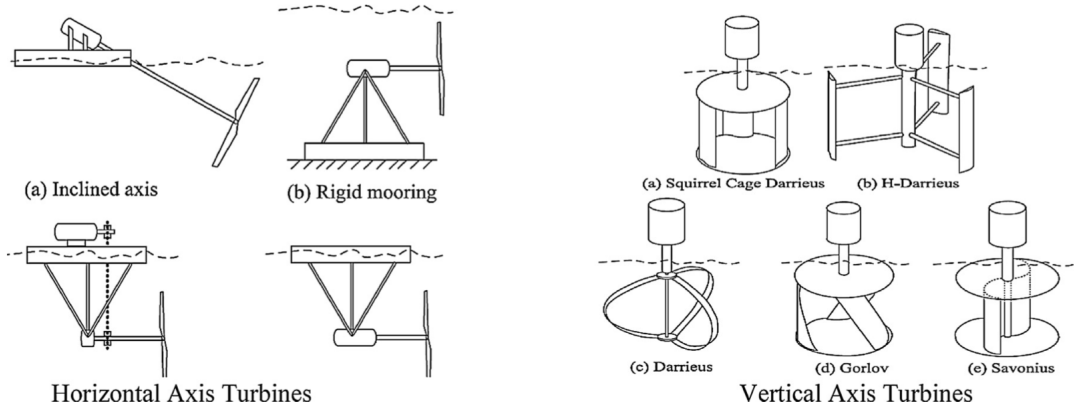

Fig. 1.5: Horizontal and vertical axis hydrokinetic turbines (Ladokun et al., 2018).

1.3.1 Some manufactured stream turbines

1.3.1.1 Tidal turbines

Technologically, the studies of the tidal turbines with an horizontal axis are more advanced than those of turbines with a vertical axis, which have so far been little tested in real conditions (Ladokun et al., 2018). Unlike wind turbines whose nacelle rotates with the wind, the axis of rotation of current turbines is generally fixed. Beyond the number, shape and dimensions of the blades, the main differences between operational turbines lie in the number of rotors: single (Sabella D10, table1.1) or double (SEAGEN, table1.1), the absence or presence of a fairing like the OpenHydro and Kaipara Harbor

models (table1.1), and finally the positioning of the rotor in the water column.

Table 1.1: Examples of different hydrokinetic technologies.

Illustration	Project	Power (MW)	d (m)	Prototype tested in
	Andritz	1	23	Norway(2003-2009)
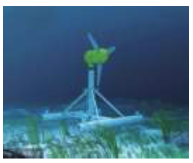	Siemens	1	16	Korea(2007), EMEC(2011)
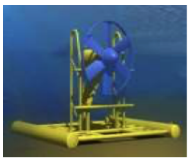	Sabella	0.2-2	3-15	Bénodet(2008-2009)
	OpenHydro	0.5-2	6-16	EMEC(2008), Bréhat(2011)
	SeaGen	1.2	2*16	Bristol(2009), Island(2008)
	Atlantis	1	18	EMEC(2010)
	Alstom	1	18-20	EMEC(2010-2013)

1.3.1.2 River turbines

There are several French manufacturers, one of them is HydroQuest. The project issued from 'Voies Navigables de France' (VNF) and operated mainly by HydroQuest, consisted on installing for the first time, a farm of four tidal turbines in the Rhône river, Lyon (France) at the end of 2018 for a period of 18 years (fig. 1.6). With its 320 kW of installed power, they can together supply 400 domiciles. This achievement is the first in the river sector, which requires specific river conditions to be efficient. The farm has been providing electricity since the end of December 2018.

Fig. 1.6: Four hydrokinetic vertical turbines in the Rhone (HydroQuest).

The advantage of this kind of turbine lies on the low impact on the environment since they are based on a floating barge moored at the bottom of the river, do not require heavy infrastructure and do not hinder the movement of fish.

HydroQuest have installed also a larger farm of river turbines in the Haut-Rhône, between Lyon and Geneva at the end of 2019. The farm is composed of 39 turbines, arranged in 13 rows of 3 units each, supplying a 2 MW of electricity.

Hydrotube/Energiea is an other French developer, they installed a floating hydrokinetic turbine in the Garonne by Hydrotube at the middle of 2015. It could reach a power of from 5 to 20 kW depending on the current velocity of the river.

1.4 Interactions with environment

Accelerating marine hydrokinetic renewable energy development towards endurance requires investigating interactions between the converter and its surrounding physical environment.

In order to exploit fully the opportunities for renewable power generation, it is necessary to be aware of (and to adjust to) a wide range of environmental disturbances in the vicinity of the power generation installations themselves. We define the interaction between stressors and receptors. The stressors that appear to present the greatest risk include the moving blades on turbines, as well as potential interactions with mooring lines, anchors or foundations, power export cables, and the emissions and interactions that can result from any of these parts (Copping et al., 2020). The receptors include the marine and riverine animals living in and traversing the vicinity of an MRE development, such as the habitats into which the devices are deployed, and oceanographic processes, such as the natural movement of waters, wave heights, sediment transport, and the concentrations of dissolved gases and nutrients that support marine life (Copping et al., 2020). It is the interaction of stressors and receptors that is discussed here (fig. 1.7) :

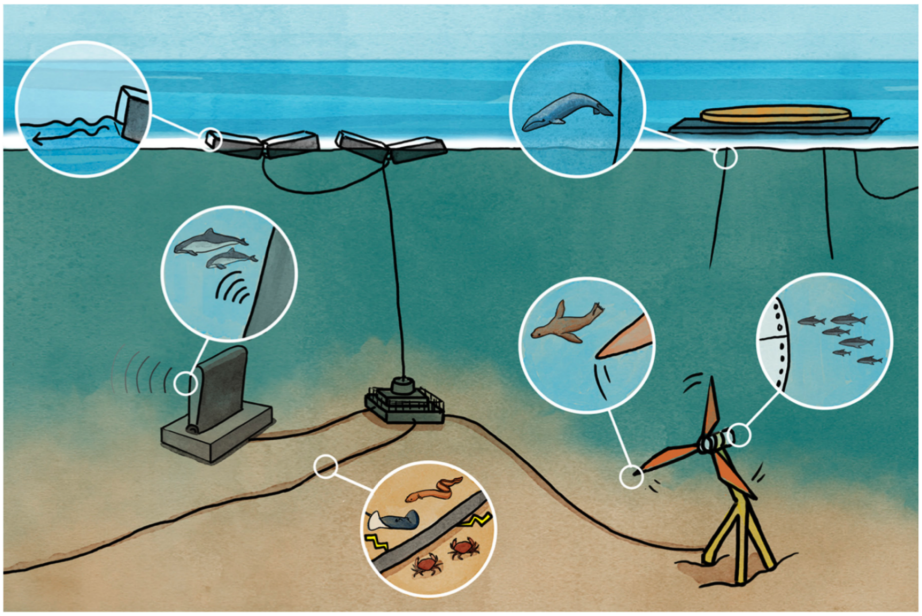

Fig. 1.7: Interactions between stressors and receptors, like changes in water surface processes, underwater noise, electromagnetic fields, mooring process, collision risk, and changes in habitats (Shields, 1936).

1. Noise and vibration: The rotation of the turbine by marine currents induces vibrations that travel through the water. However, the study of the Sabella D3 prototype turbine in South Finistere, has not demonstrated significant impacts on the

behaviour of fish presented there. So even with absence of turbines, high-current areas already experience intense hydrodynamic noise.

2. Habitat: This concerns the anchoring of electrical cables mainly in the presence of strong currents. The impacts on benthos are tied to the destruction of the habitat at the site, and the possible displacement of the more mobile species.

3. Chemical inputs: Water turbines are likely to cause impacts related to anti-fouling treatments used to prevent the colonization of machines by marine organisms, or anti-corrosion devices.

4. Barrier effect and collision risks: Marine current turbines form an obstacle in the water column with which marine mammals, fish and diving birds may possibly collide. This risk depends on the structure and diameter of the turbine, but also on the species in question, its size, and its ability to move and identify the obstacle, as well as environmental conditions such as current speed and visibility. The risk of collisions is certainly present, and the avoidance of areas frequented by marine mammals for the establishment of marine current turbines should be favoured where possible. A 16 m diameter turbine (such as Open Hydro, TGL, etc.) operating at 15 rpm (round per minute), has a blade tip speed of 12.5 m/s. To avoid the blades, animals require a swimming speed in the same range as the current and be able to detect the obstacle early enough and anticipate blade rotation.

1.4.1 Wake effects

By extracting energy from currents, an hydrokinetic turbine generates a wake. This is an area in which the flow is disturbed and the velocities are reduced due to the extraction of the energy. This wake interacts with its environment, but also with the turbine itself. Often, the near wake and the far wake are retained (fig. 1.8).
The nearby wake is characterized by a strong shear gradient and high intensity of turbulence. The length of this zone varies depending on many factors such as the intensity of the turbulence of the incident flow, the diameter of the rotor. The length varies in the range of 1 to 4 diameters (Chamorro et al., 2015) (fig. 1.8).
Near wake local impacts on the performance and the physical process of power extraction and sediment impact, otherwise, far wake research is more focused on the interactions between the turbines when they are placed in farm and regional impacts.
The far wake begins when the sheared fluid layers reach the central axis of the flow. At this level, the axis velocity profiles are similar. The far wake retains the effect of the presence of the turbine, inducing a local reduction in flow velocity. In the context of turbine's

farm, this is the concerned area to minimize interactions between wakes.

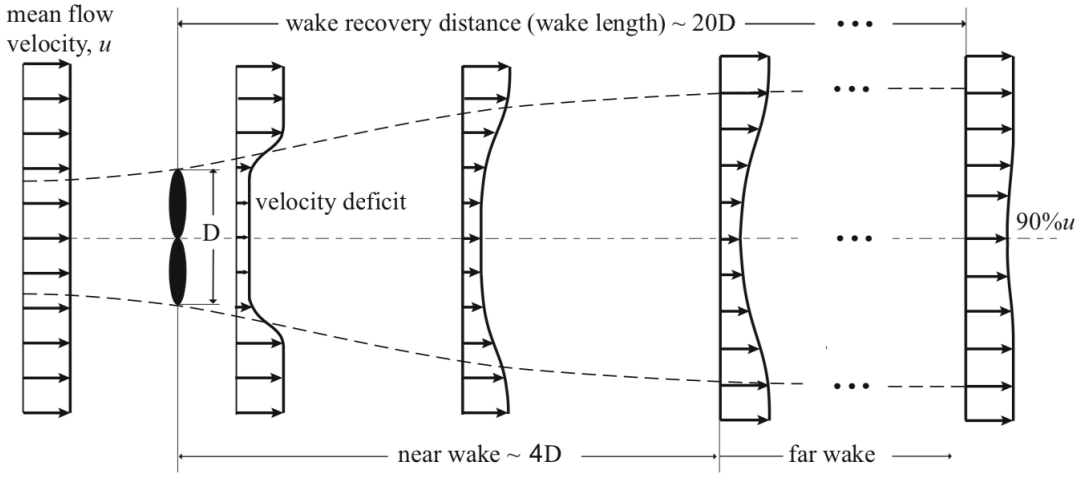

Fig. 1.8: Definition of wake characteristics (Nicholas and P.E., 2016).

Therefore, the main points that must be taken into consideration regarding the wake effects are as follows:

- Wake characteristics: velocity deficit and recovery; turbulence intensity, recovery, and structures.
- Effect of rotor design and performance on wake characteristics.
- Effect of ambient turbulence on the wake.
- Effect of channel blockage (or inter-turbine spacing) on wake characteristics.

In the following sections, the effects of ambient turbulence and the blockage ratios are studied.

1.4.1.1 Interaction with ambient turbulence

The operation of a hydrokinetic turbine is governed by the characteristics of the incident flow. The effects of the rate of ambient flow turbulence on the operation of a turbine and the wake generated must be determined (Maganga, 2011).

A turbulent flow is a chaotic flow in which vortex structures of various sizes and shapes are constantly evolving. These structures are the source of the fluctuations of the velocity $\tilde{u}$. They can be defined as being a region of space where one of the characteristic quantities of the flow shows a strong correlation with itself or another characteristic over an area or a time much greater than the smallest scales of the flow (fig. 1.9).

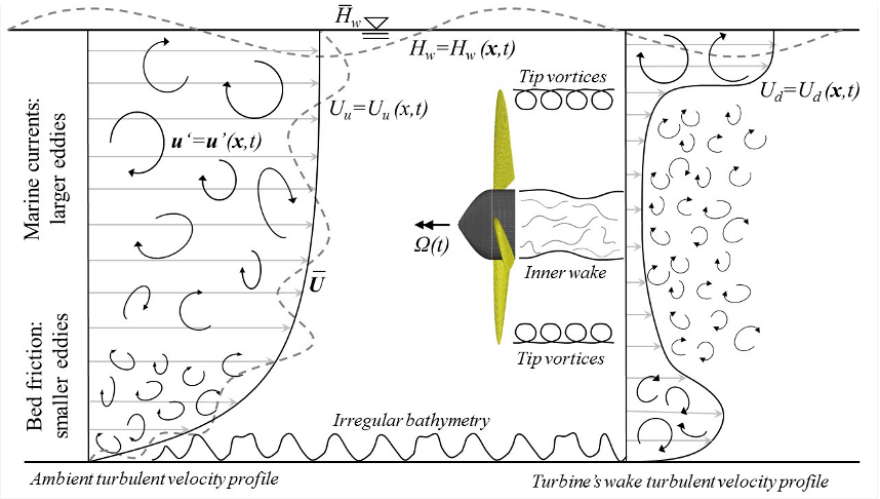

Fig. 1.9: Representation of the marine and fluvial conditions where horizontal axis hydrokinetic turbines operate in (Ouro, 2017).

The turbulent flows are unsteady and difficult to characterize at any given time. One solution consists in averaging the macroscopic physical quantities of these flows over sufficiently long times. These quantities are, for example, the average velocity U_∞ and the average of the fluctuations of the velocity $\tilde{u}_\infty$. Here we can define the Turbulence Intensity (TI) which is one of the indicators of turbulence in a flow passing through a turbine, and is defined as the standard deviation of the flow velocity fluctuations divided by the average flow velocity (see eq.1.1). In the wake of a turbine, the intensity of turbulence has two origins: ambient turbulence and turbulence caused by the shear of the rotor blades. The intensity of ambient turbulence at sea or in the oceans depends on the bathymetry, the boundary layer on the bottom, the altitude considered and the swell.

$$TI_\infty = 100\sqrt{\frac{\frac{1}{3}[\sigma^2(\tilde{u}_\infty)+\sigma^2(\tilde{v}_\infty)+\sigma^2(\tilde{w}_\infty)]}{U_\infty^2+V_\infty^2+W_\infty^2}} \tag{1.1}$$

where the velocity U_∞, V_∞, W_∞ are the components of the upstream velocity vector U_∞. The chaotic nature of the turbulence makes it extremely difficult to predict and that is why it is still the subject of much research today (Grondeau et al., 2020; Mycek et al., 2014; Maganga, 2011).

Numerous studies by (Sentchev et al., 2019; Clark et al., 2015) carried out on the influence of the ambient turbulence rate on the behavior of turbines by impacting both their performance and their structural integrity. Such as (Kaiser et al., 2003) and (MacLeod et al., 2002), it is shown regarding the wind turbines in general that the turbulence decreases with the distance downstream of the turbine and that the velocity deficit decreases

as quickly as the intensity of turbulence of the upstream flow is great. These studies also show that axial force fluctuations increase with the intensity of turbulence, and they predict faster flow recovery in areas of the highest turbulence intensity.

Concerning the hydrokinetic turbines, functional turbines have been deployed on certain sites such as Paimpol-Bréhat in french Brittany. Lawrence et al. (2009) present current measurements, bathymetry and waves at the EMEC site in Orkney (UK). The results they obtained showed that this site has good tidal potential with average speeds ranging from 1.3 to 3.5 m/s. Generally, in the marine environment, the ambient turbulence rate varies with the speed of the current in the area and the type of bottom.It is important to note that the intensity of turbulence at sea can go beyond by 50% (Maganga, 2011). Blackmore et al. (2016) and Stallard et al. (2013) have shown that the presence of turbulence could cause variations in the power and drag coefficients which can have a considerable impact on the fatigue of the blades, the gearbox and the electric generator, hence, influence the design of the machine.

The tests carried out in the IFREMER test basin at 'Boulogne Sur Mer' by Mycek et al. (2014) on a three bladed axial flow turbine show that when the ambient turbulence intensity went from 3% to 15%, the average performance of the turbine is degraded by a maximum of 10%. For an ambient turbulence rate of 3%, the influence of the turbine is always visible at a distance of 10 diameters behind the machine. On the other hand, for a turbulent intensity of 15%, the wake of the turbine disappears at 6 diameters (fig. 1.10), with only 5% of velocity deficit and a rate of turbulence perfectly returned to its initial value. At this distance, the flow no longer presents any coherent patterns. Thus, installing a second turbine could almost provide the same conditions as the upstream turbine, with only 15% of available power deficit corresponding to 5% of velocity deficit.

1.4.1.2 Turbine-turbine interaction, effects of confinement between turbines

Figure 1.11 shows an overview of the main flow phenomena developed in arrays of hydrokinetic turbines deployed in several rows in a staggered way as it is accepted to be more efficient than aline layouts (Ouro et al., 2019). A series of experimentation tests by Mycek et al. (2014) to demonstrate the existence of interaction effects between two aligned hydrokinetic turbines with different inter-turbine distances, thus the downstream turbine suffers considerably from the presence of the upstream turbine. They observed that with TI = 3%, the performance of the second turbine is degraded to 50% compared to the performance of a single turbine, even with a inter-turbine distance of $12d$.

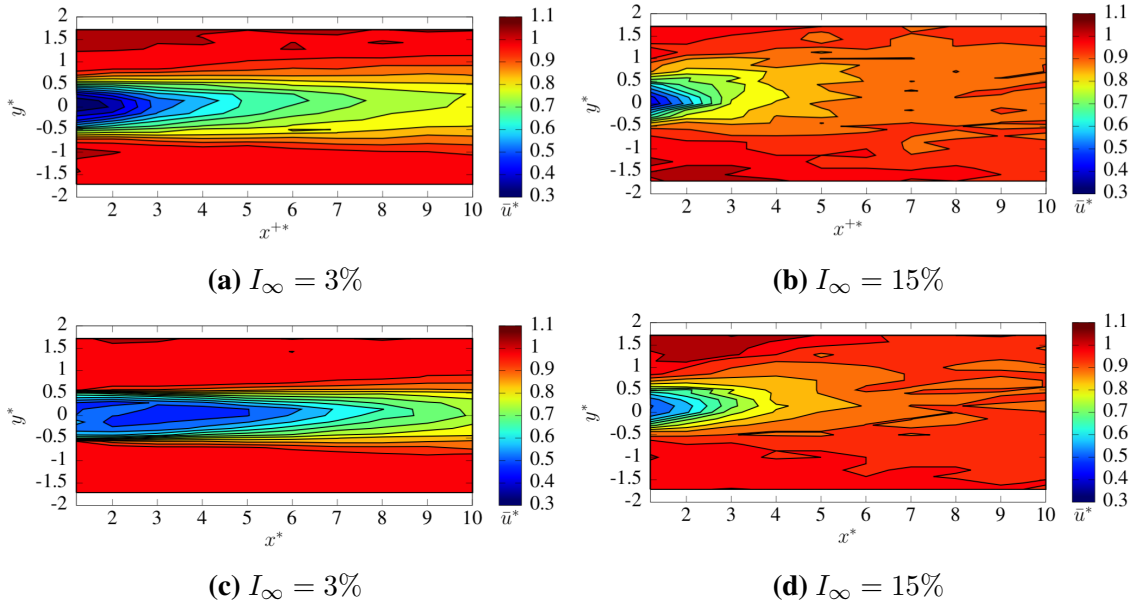

(a) $I_\infty = 3\%$ **(b)** $I_\infty = 15\%$

(c) $I_\infty = 3\%$ **(d)** $I_\infty = 15\%$

Fig. 1.10: Axial velocity contouring (top): downstream the second turbine with inter distance of $4d$, at $TSR = 3.67$ and $U_\infty = 0.8m/s$ for $I_\infty = 3\%$ (left) and $I_\infty = 15\%$ (right); (down): downstream the single turbine at $TSR = 3.67$ and $U_\infty = 0.8m/s$ for $I_\infty = 3\%$ (left) and $I_\infty = 15\%$ (right).

Otherwise, with TI = 15%, the similar behavior to that of a single turbine is almost found as soon as the distance exceeds six diameters. This distance indeed corresponds to the area where the flow begins to regain its homogeneity in terms of turbulence rate. Thus, a higher rate of ambient turbulence appears to be therefore more suitable for the installation of a turbine farm. Hence, to study the interaction between many axial flow turbines installed in a farm, Nguyen (2015) have modeled the impact of spacing between 10 machines arranged in staggered rows on their performance. These machines are subjected to a constant current for dimensions comparable to those of the Alderney Race. It was observed that the confinement existing between the machines of the first line, induces a slight effect of velocity acceleration and implies that the central machines of the second line have a power slightly higher than that which is available for the machines placed at the end of the line. The cases studied previously highlight that the increase in the longitudinal spacing allows better recovery of velocities in the wake of the machines on the first line. Same observation has been made by Stallard et al. (2013). Chawdhary et al. (2017) performed experimental tests and high-fidelity simulations of three turbines sharing a triangular-shaped support structure and observed that the overall power output of these devices is higher in such close arrangement than if placed individually.

Note that a downstream turbine, aligned axially in the wake of a first turbine, does not behave as if it was placed in an undisturbed flow exhibiting an equivalent rate of ambient turbulence. This is due to the coherent structures of small to medium scales that develop

in the wake of a turbine.

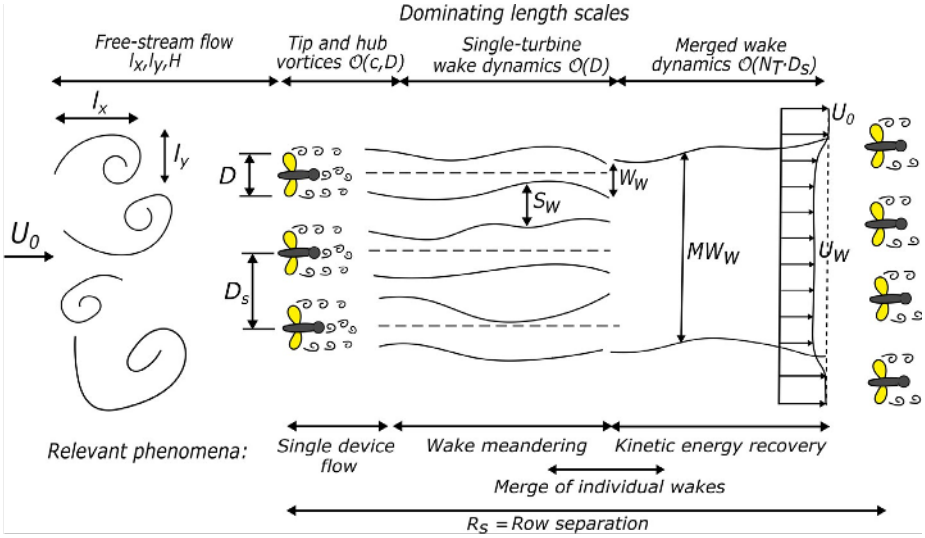

Fig. 1.11: Schematic of the hydrodynamics of an array of tidal turbines (Ouro et al., 2019).

1.4.2 Turbine-sediment interaction

It is known that flow passing turbine support structure combined with the rotation of the turbine rotors produces a turbulent downstream wake that can be sufficiently energetic to disturb the stability of the sediments on the sea bed on which the turbine is constructed and affect the sediment suspension. This may have significant impact on the sea and river floor topography and changes of suspended sediment in water. The presence of the turbine could accelerate the flow and lead to a local scour (Xia et al., 2010). It is crucial to ensure the structural safety of the turbine to avoid interruption of energy transmission. In addition, the sediment transport due to the presence of the turbine, could have negative environmental impacts. This may lead to the change of the site's topography which could result in negative consequences for the environment. Hydro-sedimentary modifications can locally modify beneath habitats. For a large number of turbines, a long-range effect on sediment transit could disrupt habitats several kilometres away. This could be the case of hydraulic dunes, which play an essential role as nurseries for certain fish species). Exploring the turbine-sediments interactions demands intensive research studies in the form of either experiments, or numerical simulations or even in situ configurations.

This part of the manuscript attempts to draw up a state of the art of knowledge of sediment transport in the presence of the turbine. The basic principles of this physical phenomenon and the different modes of sediment transport will be detailed first. Then we provide the interaction turbine-sediments in the next state of art part.

1.4.2.1 Definition of the sediments

Sediments are a collection of particles resulting the alteration of continental geological formations and whose erosion, transport and deposition are controlled by physical processes such as wind, water or ice. The sediments have a great diversity (size, shape). In the literature, many size classifications have been proposed. Since the sediments have different behavior, dynamics and reactions to environmental stresses depending on their size, we will not find the same kinds of sediments close or far from the erosion zone. The heavier sediments will be those that move the least distance between the erosion zone and the deposition zone. In coastal environments, the sediments are smaller than the order of a few millimeters and are mainly sands. In a river environment, there are also coarser sediments such as gravel (of the order of ten millimeters) or large pebbles (several tens of millimeters).

Particle size is not the only parameter influencing the behavior of sediments. The finer the sediments, the more organic matter content is important. This makes it possible to distinguish between non-cohesive and cohesive sediments. The non-cohesive particles are independent of each other and their movements are made individually, this is the case of pebbles. The particles will tend to agglomerate under the effect of attractive molecular forces to form aggregates, this is the flocculation (Chauchat et al., 2017). The cohesive sediments respond differently comparing to non-cohesive ones against the environmental stresses (current, waves, etc.), this is the case with mud, for example. In this thesis work, only the non-cohesive sand-type sediments are considered.

1.4.2.2 Modes of transport of sediments

This part is devoted to the study of sediments transported by a flow. The purpose is first to understand the various modes of sediment transport, the mechanisms that generate this transport, and their modeling. Sediment transport occurs differently depending on the nature of the sediment and the size of the grain, at varying levels of depth and proximity to the bottom.

Figure 1.12 shows the forces acting on non-cohesive particles. The fluid force is decomposed into an upward vertical buoyant force (lift) and a frictional force of the water on the sediments, horizontal in the direction of flow (drag). For sediment transport, this force must be sufficient to compensate for both the force of gravity to which the sediments are subjected and the friction force of the sediments in contact with the bottom.

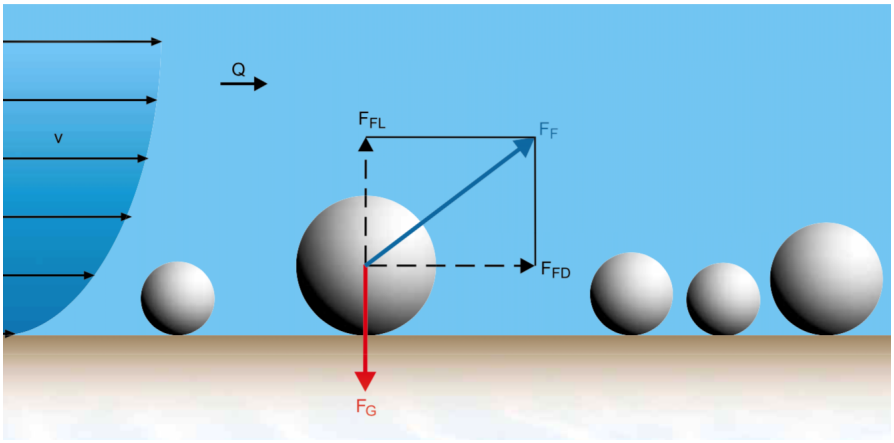

Fig. 1.12: Forces acting on a non-cohesive particle that is part of the bed; v: flow velocity, Q: flow rate, F_G: gravity force, F_{FL}: lift force, F_{FD}: drag force [1].

The transport can be in the form of bed-load (with permanent or interrupted contact with the sediment bed by rolling, sliding, or saltation (fig. 1.13) and suspended-load (without contact with the sediment bed) depending essentially on two parameters: the shear stress rate and the grain size of sediments. In the suspended load, sediment concentration is low and the suspension of particles is driven due to their interactions with turbulent eddies. In the near bed region, the sediment concentration is much more higher, about 60% in term of volume fraction. The riverine waves generate currents whose energy allows the begining of the detachment of the sediments and their transport all along the stream water (fig. 1.14a and 1.14b).

The currents in rivers, canals and coastal areas are often accompanied by sediment transport. Sediment transport consists of suspended sediment transport and bedload transport.

Bedload transport takes place in the area near the bed (fig. 1.14b) and is therefore a very important factor in shaping the river bed (fig. 1.14a). In natural running waters, erosion and sedimentation processes alternate continuously and characterize the bedload regime of the stretch of stream. Bedload transport is the benchmark component of flow behavior in canals. Sediments that settle (land) or are transported (erosion or scouring) can, for example, modify the flow section or the water lines (fig. 1.14a). The transport of sediments also leads to a modification of the structure of the bed (formation of wrinkles or dunes, modification of the roughness). For a river bed composed of less cohesion grains (sand), the sediment starts to move when the bed shear stress τ_b exerted by the flow is higher than the friction force between the grains, the critical shear stress τ_c. This is typically represented by a comparison between a dimensionless shear stress (τ_b*) and a dimensionless critical shear stress (τ_c*).

[1] https://www.gunt.de/

The non-dimensionalization is in order to compare the driving forces of particle motion (shear stress) to the resisting forces that would make it stationary (particle density and size).

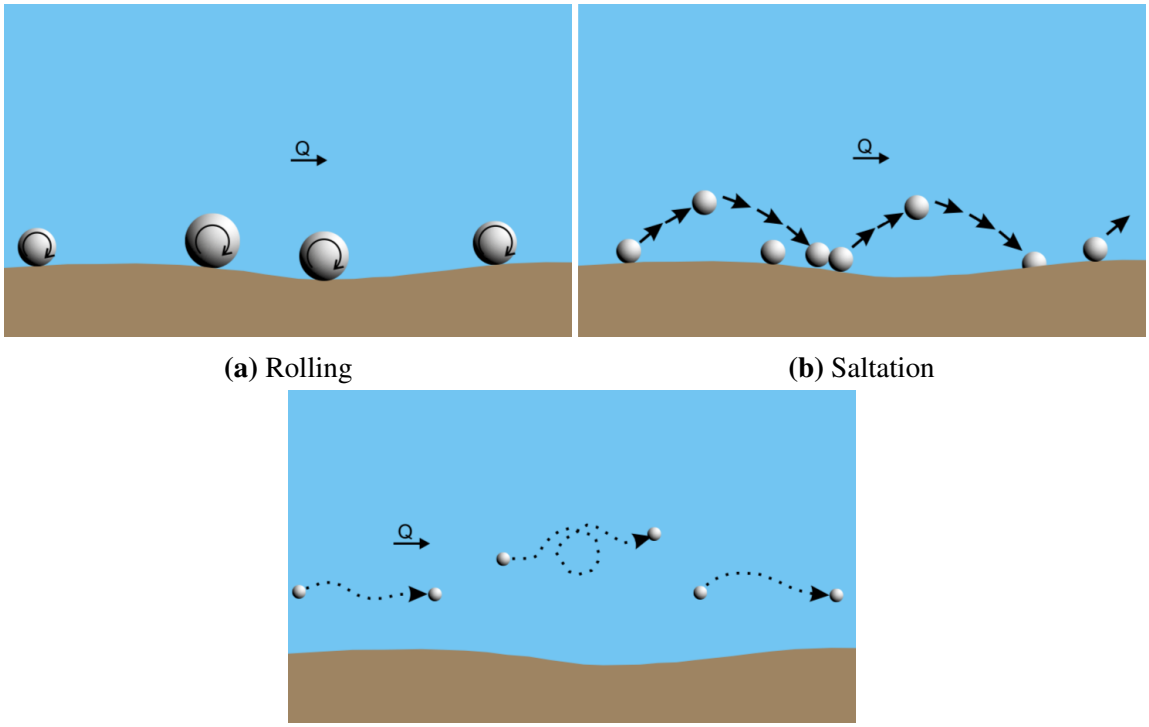

(a) Rolling **(b)** Saltation

(c) Suspension

Fig. 1.13: Three different modes of transport [2].

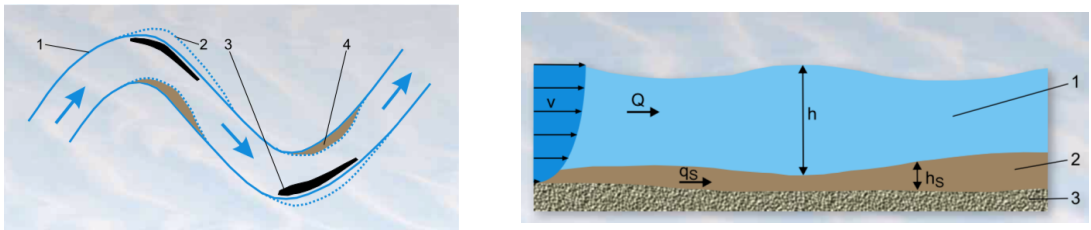

(a) **(b)**

Fig. 1.14: Top view of a river (left), 1: original path of stream water, 2: modified path of stream water due to sediment transport, 3: scouring and erosion, 4: deposition term; Parallel view of a river showing 1: water, 2: mobile sediments, 3: fixed bottom, v: flow velocity, Q: flow rate, h: depth of water, h_s: thickness of bed-load [2].

This dimensionless shear stress, $\tau*$ or θ, is called the Shields parameter (Shields, 1936) and it is defined as the ratio between the drag force and the apparent submerged

[2]https://www.gunt.de/

grains weight :

$$\theta = \frac{\tau_b}{(\rho_s - \rho_f)gd_s} \tag{1.2}$$

The sediment starts to move as soon as the Shields parameter exceeds a critical value ($\theta > \theta_c$), which depends on the density and the grain size.

For a given size of the grains, the sediments will stop moving and fall back into the bottom as soon as the tangential stress of critical deposit τ_b will be reached, in this case $\tau_b = \tau_c$. When τ_b is reached, the sediment will then fall back onto the bed. But τ_b depends on the size of the grain. Large grains fall as soon as the gravity is higher than the lift but they can remain suspended in the thrust layer through the action of vortices. That means in this case that $\tau_b > \tau_c$. It then appears a phenomenon of delay of deposit. The grains of different size will not reach the bottom at the same time.

When the sediments form a Cluster, these last have the same effect as wrinkles on the sediment surface. These wrinkles are only a few grains thick and influence the flow in the boundary layer. The streamlines are closer to each other at the top of a cluster, the flow speed is higher here (Venturi effect). As the flow velocity increases, it is possible that other grains will roll on the flow side or jump and collect at the top of the ridge. When too much grain has collected, the position becomes unstable, they slide down the cluster on the other side. This side has a steeper slope than the side faced to the flow (fig. 1.15).

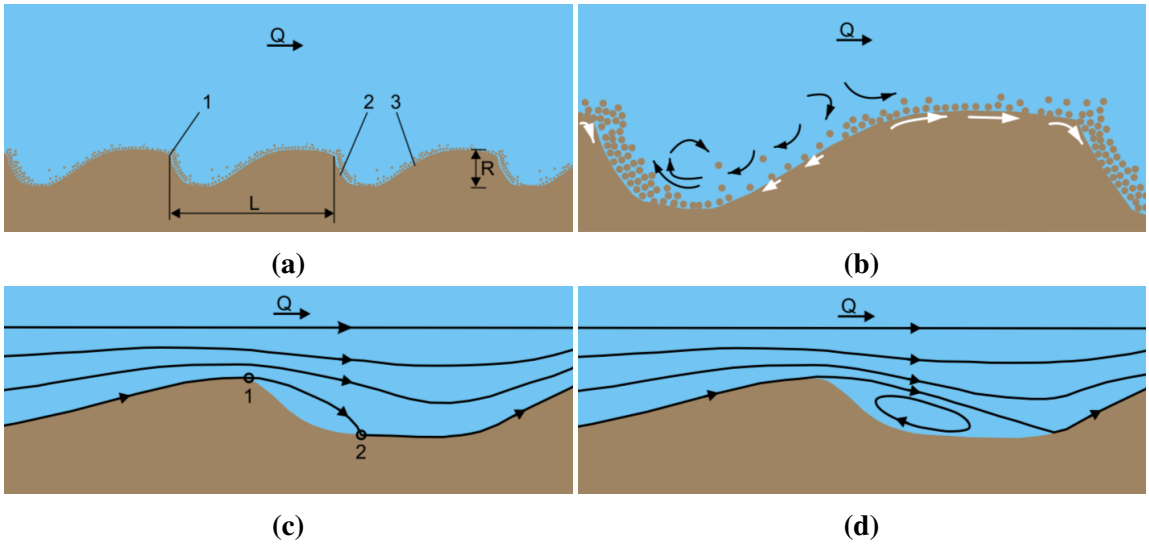

Fig. 1.15: Three different modes of transport (https://www.gunt.de/).

On the crest of the cluster, the current line on the surface of the sand detaches itself from this surface and later returns to strike it (fig. 1.15: appearance of counter-currents on the other side of the flow) . Below this current line there is what is called the separation zone. It is possible that a separation vortex will form in this area, causing a small counter

current. In addition, there is turbulence and erosion, which causes the formation of scours between the ripples. The grains of sand at the top of the sediment layer continue to be transported continuously, so that the ripples move in the direction of the flow and therefore appeared mobile (fig. 1.15).

From the modeling perspective, a complex model is required to underline the physical coupling mechanism and integrate the main transport modes of sediments. During the past two decades, the research efforts have been devoted to develop two-phase flow models for sediment transport. In the next section, we present the different models existed to modelling the interaction turbine-sediments.

1.5 Modeling of interaction turbine-sediments

1.5.1 State of art

Modeling is an interesting tool for the development of the hydrokinetic turbine's industry. There are many numerical investigations in the recent years concerning the impact of the presence of hydrokinetic turbines in the regional scale, whereas the turbines' array is represented by a bed friction or momentum sink using the Actuator disk theory (AD) (Nguyen et al., 2016). Since Batten et al. (2013) have compared the results of the actuator disc-RANS model, where the turbine forces have been derived using a blade-element approach, to experimental data measured in the wake of a scaled turbine. The comparisons show that the model is accurate and can predict up to 94% of the variation in the experimental velocity data, therefore demonstrating that the actuator disc-RANS model is an accurate approach for modelling a turbine wake. Hence, it can be applied to similar scenarios with confidence. The sediment transport is modeled using a classical approach, such as Thiebot et al. (2015) who have modeled the effect of an array of turbines on the sediment transport by placing a 290 MW tidal turbine array in the Alderney Race using a regional 2DH hydrodynamic model (Thiebot et al., 2015). They found as a result that the tidal energy extraction has a significant effect on the rate and the pattern of the bed load sediment transport rate in the regional scale. Also Fairley et al. (2015) studied the cumulative impact of HT on sediment transport in the Pentland Firth by applying a three-dimensional coupled hydrodynamic and sediment transport numerical model. They have concluded that the array implementation only has minimal effect on the baseline morphodynamics of large sandbanks. Neill et al. (2009) used large grid-cell simulations to assess the impact of an HT array on the sand banks off the northern coast of France. Their study investigated a tidal channel many kilometers long, therefore lacking their solution to simulate the near-field effects. Gillibrand et al. (2016) have simulated arrays of 1, 4 and

57 tidal turbines, each of 1.5 MW capacity using a 3D hydrodynamic model (RiCOM) (Gillibrand et al., 2016). The main effect is observed for the array of 57 turbines while increasing the near-bed velocities and and the bed shear stress, leading to a significant transport of sand.

To date, few studies exist on how HT devices modify erodible channels at its vicinity, despite the fact that it is important to develop a holistic understanding as to how these devices affect all aspects of physical environment in the local scale. Hill et al. (2015) have shown experimentally that the presence of either single or multiple turbines and the rotation of the blades affect the bed morphology (fig. 1.16 and 1.17). Musa et al. (2019) have investigated experimentally the local effect of streamwise aligned turbines on the bedload, they found as a result that the geomorphic effects are stronger with increasing shear stress due to the presence of the rotors, inducing an alternating scour-deposition phenomenon. Chen et al. (2017) have investigated the influence of rotor blade tip clearance control (distance between blades and seabed) on the scour rate of pile-supported horizontal axis tidal current turbine and also attempted to correlate time-dependent scour depth of TCT with the tip clearance. The results suggest that the decrease in tip clearance increases the scour depth. In addition, the shortest tip clearance results in the fastest and most important sediment transport. Ahmed et al. (2017) studied the fluctuating loads on tidal turbines which are important for fatigue analysis. Computational Fluid Dynamics (CFD) simulations have been performed for a geometry-resolved full-scale tidal-stream turbine and compared with experimental data from a 1 MW machine deployed at the EMEC test site in the Orkneys. They employ realistic inflow profiles of mean and turbulent velocity fields based on measurements from the deployment site. The simulated velocity field indicates that the turbine rotor influences the axial velocity and the flow turbulent structures to about one diameter (1D) upstream of the rotor, while velocity deficit and enhanced turbulence are extending beyond the 10D downstream.

However, there are very few studies that investigate by numerical simulation the local impact of turbines on sediment transport.

In this case, the turbine is represented finely by either the Blade Element Momentum Theory (BEMT) (Malki et al., 2012), or by Actuator Line approach (AL) (Apsley et al., 2018) for blades, or even by a fully resolved configuration (Grondeau et al., 2020). Yang et al. (2017) have simulated the interaction between hydrokinetic turbine and bedload sediment transport using large eddy simulation (LES) for the flow, and the Saint-Venant-Exner model (Paola and Voller, 2005) for sediment transport and Actuator Line theory for the turbine blades. A deeper scour and deposition regions are observed when imposing a higher tip speed ratio on rotors. Chen and Lam (2013) highlighted that the clearance

between rotor and seabed becomes critical in the turbine induced scour prediction. It further evidences that the height of tip clearance plays a critical role in designing scour-related units of the turbine.

Fig. 1.16: Photo of single turbine with bedforms during experiments of Hill et al. (2015).

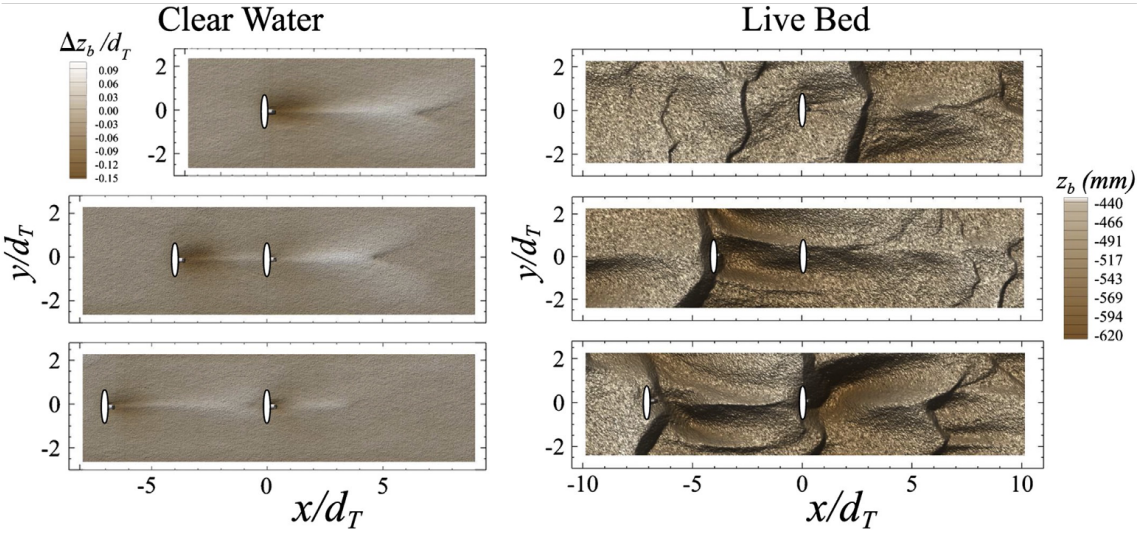

Fig. 1.17: Final topography for the clear water experiments (left): single (top), $4d$ (middle), and $7d$ (bottom). Color scale represents normalized scour (dark colors) and deposition (light colors). Final topography for the live bed experiments (right): single (top), $4d$ (middle), and $7d$ (bottom). Flow is from left to right (Hill et al., 2015).

The velocity pattern near the seabed of the turbine has been studied through three-dimensional numerical simulations (Chen and Lam, 2014). Chen and Lam (2014) studied the flow pattern between the turbine and seabed. They formulate the hypothesis that the

axial component is the largest contributor to the magnitude of velocity. Therefore, the tangential component is so insignificant that they suggest that the tangential component of velocity has no impact to the scour and deposition process.

Musa et al. (2019) derived and validated a modeling framework to predict the scour induced by hydrokinetic turbines. The model addresses the problem of bridge pier scour using the phenomenological theory of turbulence. The turbine rotor should be close enough to the sediments that the erosion is caused directly by the tip vortex shed by the turbine blades. Musa et al. (2018) investigated the effect of an array of hydro-kinetic turbines on the morpho-dynamics of river sand, they found despite that the wakes of these devices are highly turbulent, so they had a minimal impact in the sediment transport processes.

Ramirez-Mendoza (2018) have used a series of laboratory experiments and studied the impact of the presence of a horizontal-axis turbine with the flow and a mobile sediment bed. The results showed a decrease of velocity profiles about 50% throughout the water column and the flow is not recovered after a distance of 15 rotor diameters in the wake. These results may be important to have an idea about the effects on the efficiency of turbine arrays on turbine foundations and modify coastal sediment transport.

Therefore, the interaction between HT and the bed morphology in the near wake deserves more studies at the local scale. In addition, the difficulties and inaccuracies associated with the classical sediment transport modeling approach require the development of other approaches to transport modeling, which are more complete and integrate the complexity of the coupling phenomena between the different modes of sedimentary transport and hydrodynamics, especially at the grain scale (Guillou et al., 2011).

The development of a two-phase approach of sediment transport has been a very active research topic in the last decade. The equations of dynamics are solved for the two phases constituting the fluid phase (water) also the particulate phase. For the latter, the sediment is considered as a continuous phase and dispersed in the fluid. Unlike the so-called classical approach, this two-phase approach makes it possible to take into account the majority of the physical processes of sediment transport, namely the interactions between particles and fluid, the effect of fluid turbulence on the particles but also the particle-particle interactions. The two-phase approach is based on solving the conservation equations for mass and momentum for the two phases (fluid and sediment). The fluid phase is still considered as a continuous phase, but there are several ways of determining the dynamics of the particulate phase. Therefore, it is possible to describe the behavior of each particle and their interactions, that is called the Lagrangian approach (Escauriaza and Sotiropoulos, 2011). Describing the sediment in a Lagrangian way is numerically very expensive and therefore restricted to a limited number of particles (Capecelatro and Desjardins, 2013). In the literature, the two-phase models rather consist on considering a continuous approach to

describe the sediment and the fluid phases, such as the two-phase Eulerian-Eulerian models. In this case, the equations of solving the momentum for the fluid (eq. 1.3) and the sediment (eq. 1.4) are very similar to each other and based on the Navier-Stokes equations (Nagel, 2019):

$$(1-\phi)\rho^f(\frac{\partial u^f}{\partial t}+(u^f.\nabla)u^f)=-(1-\phi)\nabla p^f+(1-\phi)(f+\rho^f g)+\nabla.\tau^f-n_p f_D \tag{1.3}$$

$$\phi\rho^s(\frac{\partial u^s}{\partial t}+(u^s.\nabla)u^s)=-\phi\nabla p^f-\nabla p^s+\phi(f+\rho^s g)+\nabla.\tau^s+n_p f_D \tag{1.4}$$

where ϕ is the volume fraction of sediment, ρ^s and u^s the density and the velocity vector for sediment phase, ρ^f and u^f those for fluid phase, p^s and τ^s the pressure and shear stresses of sediment phase, p^f and τ^f those of fluid phase, g the acceleration due to gravity, f the volume forces other than gravity, f_D the forces applied by the fluid on a single particle and n_p the number of particles per unit volume. The momentum conservation equations for the fluid (eq. 1.4) and solid (eq. 1.4) phases are coupled by the term f_D which represents the interactions between the fluid and the particles. This term distinguishes these two-phase equations from the Navier-Stokes equations used for the monophasic approach. Closure models are needed to determine the granular stresses for the sediment ($p^s+\tau^s$) as well as the stresses for the fluid ($p^f+\tau^f$). The different two-phase models for sediment transport presented in the literature can be differentiated by the choices made by their authors concerning the closure models for turbulence or granular stresses. Regarding the closure models for turbulent stresses, there are several large families: RANS models (Reynolds Averaged Navier Stokes equations) called "zero-equation" such as the mixing length approach, RANS models with two equations ($k-\epsilon$, $k-\omega$) (Cheng et al., 2018b). For closure on granular constraints, a first approach based on the rheology of Bagnold (Bagnold, 1954) was used in the case of an oscillating sheet-flow by Bakhtyar et al. (2009). However, this closure model is not widely used in the literature and two other approaches are considered: the kinetic theory of granular flows (Jenkins and Savage, 1983) or the rheology of dense granular flows (Forterre and Pouliquen, 2008b). Derived from the kinetic theory of gases, the kinetic theory of granular flows was first written for dry granular flows (in air). This approach is based on the idea that interactions between particles are dominated by binary collisions. Thus, the granular stress can be determined from the fluctuations in particle phase velocities, the measurement of these fluctuations is called granular temperature. This approach is known to be unsuitable in the densest parts of the flow. The second major approach for determining

granular stresses is a dense granular flows rheology for dry granular flows. This approach is built on a dimensional analysis of a simple shear configuration (Forterre and Pouliquen, 2008b; Chauchat and Médale, 2014) and uses the inertial term I as a control parameter. This latter is the parameter controlling the coefficient of friction $\mu(I)$ making possible the link between the particle pressure and the granular shear stress necessary to close the equation of momentum of the particle phase. Most of the two-phase approaches applications are one-dimensional and use RANS closure models for turbulence. There are few two-dimensional cases (Amoudry et al., 2008; Bakhtyar et al., 2009; Cheng et al., 2016) and a very recent 3D case, using a LES for turbulence (Cheng et al., 2018b). The few multidimensional cases can be explained by the complexity of the models used for the two-phase approach as well as by their high cost, in terms of computation time. The application of the two-phase approach to various multidimensional study cases therefore involves the development of a multi-dimensional two-phase model integrating the various closure choices for both turbulence and granular constraints (Uh Zapata et al., 2018).

There has been no investigation until now concerning the effect of blockage on the sediment transport in the presence of a hydrokinetic turbine at the local scale. The blockage effects, described by Garrett and Cummins (2007) and by Nishino and Willden (2012), are studied especially on the hydrodynamic performance of turbines, such as by Consul et al. (2012). They have explored the influence of blockage on the hydrodynamic performance of a generic marine cross-flow turbine. They found that increasing in the blockage lead to an increase in power coefficient of turbine. Schluntz and Willden (2015) have studied the effect of blockage on rotor optimization using the BEM theory. Increased blockage lead to an increased optimal solidity and decreased optimal pitch in terms of blade design.

When studying the blockage effects on the turbine-sediment interaction, it is crucial then to investigate the impact of the confinement of many turbines on the transport of sediment. Hill et al. (2015) have investigated the interactions between relatively large-scale sediment dunes of 1.8 mm coarse sand and two axial flow hydrokinetic turbines. It was observed that the influence on the bed topography is only local and restricted in an area approximately $6d$ by $2d$ in the streamwise and spanwise direction, respectively (fig. 1.17). Otherwise, no blade damage was observed in any of the experiments, since the annular shear layer and local acceleration below the bottom tip of the turbine protect the rotor from potential impacts with the incoming bedforms (Hill et al., 2015).

1.6 Aim of the thesis

The aim of the thesis is to implement models integrating the presence of tidal turbines in a sedimentary seabed. For that we propose to develop procedures using the theory of the elements of blades (BEMT) to represent the tidal turbine. We apply an unsteady approach to study the interaction of the turbines with their sedimentary environment. The open source software 'OpenFOAM': Open Field Operation and Manipulation, is used during the present work.

This present contribution is divided into seven chapters, including this introductory chapter.

The second chapter presents the definitions of the mathematical theories used in the Euler-Euler multiphase approach, these theories are implemented numerically in OpenFOAM by a specific code called SedFoam derived from the TwoPhaseEulerFoam, a library in OpenFOAM (Chauchat et al., 2017), followed by a series of benchmark tests of validation executed in the litterature.

The CFD hydrodynamic models linked to the modeling of a turbine are described in the third chapter, such as the Actuator Disk model and the Blade Element Momentum Theory. The implementation of the interaction model, combining the Eulerian approach and BEMT, in OpenFOAM is shown and the most suitable tools for the code are selected. The combined code is then validated with the experimental measurements of Mycek et al. (2014) regarding the performance of the turbine and the wake distribution.

In chapter 4, we validate the combined model (presented in chapter 3) with the measurements of Hill et al. (2014) regarding the effect of the presence of the turbine on the bedload under clear water conditions. Beside the validation, the numerical results of the modeled interaction of the turbine represented by AD or BEMT and the transport of sediments are compared.

The chapter 5 is considered as a first application of the combined model. It investigates the blockage effects on the sediment transport in the presence of the turbine.

In chapter 6, the case study of two turbines in a channel is considered. Especially, the effect on the erosion/deposition close to the turbine, and the global effect on the general sediment motion.

The simulations and the calculations presented in this work, are all made on the server of CRIANN (Centre Régional Informatique et d'Application Numériques de Normandie).

Chapter 2

Modeling of transport of sediments

2.1 Introduction

This chapter recalls the hypothesis and the equations used in the two-phase Euler-Euler modelling used to simulate the sediment transport in water. The model consists of averaging the mass and momentum conservation equations to describe the time-dependent motion of the both phases. This requires defining the inter-phase momentum transfer and turbulence models for closure. The inter-phase momentum transfer is determined from the instantaneous forces acting on the dispersed phase, comprising drag, lift and virtual mass. Two ways of representing the inter-granular constraints are considered: the kinetic theory of granular flow and the rheology of dense granular flow. On the other hand, regarding the fluid constraints, the approach takes into consideration laminar or turbulent flows, and four models of turbulence such as the model mixing length (for 1D configuration only), and several models of two equations of the URANS like $k-\epsilon$, $k-\omega$ and $k-\omega 2006$.

We use the model developed by Imperial College (Nagel, 2019). Chauchat et al. (2017) and Nagel (2019) have described the different aspects of the model and integrated it numerically into OpenFOAM as a source code called 'SedFoam'. Then, the model has shown its ability to model the scouring and the deposition terms when Bonamy et al. (2017) have validated the model with several benchmarking cases. In this chapter, we recall some elements of the development, the integration and the validation of the model.

2.2 Mathematical formulation

2.2.1 Turbulence averaged two phase flow

The mathematical formulations of the Eulerian two-phase flow model is obtained by averaging the local and instantaneous mass and momentum conservation equations for

fluid and dispersed particles (Hsu et al., 2004). The mass conservation equations for the particle phase and fluid phase are written as:

$$\frac{\partial \phi}{\partial t} + \frac{\partial \phi u_i^s}{\partial x_i} = 0 \tag{2.1}$$

$$\frac{\partial (1-\phi)}{\partial t} + \frac{\partial (1-\phi) u_i^f}{\partial x_i} = 0 \tag{2.2}$$

where ϕ , and $1-\phi$ are the particle and fluid volume fractions respectively, u_i^s, u_i^f are the sediment and fluid phase velocities respectively, and the index i = 1, 2, 3 represents the streamwise, spanwise and vertical component, respectively.

Based on (Cheng et al., 2017), the momentum equations for fluid and particle phases can be written as:

$$\frac{\partial \rho^s \phi u_i^s}{\partial t} + \frac{\partial \rho^s \phi u_i^s u_j^s}{\partial x_j} = -\phi \frac{\partial p}{\partial x_i} + \phi f_i - \frac{\partial p^s}{\partial x_i} + \frac{\partial \tau_{ij}^s}{\partial x_j} + \phi \rho^s g_i + M_i^{sf} + S_i^f \tag{2.3}$$

$$\begin{aligned} \frac{\partial \rho^f (1-\phi) u_i^f)}{\partial t} + \frac{\partial \rho^f (1-\phi) u_i^f u_j^f}{\partial x_j} = -(1-\phi)\frac{\partial p}{\partial x_i} + (1-\phi) f_i + \frac{\partial \tau_{ij}^f}{\partial x_j} \\ +(1-\phi)\rho^f g_i + M_i^{fs} + S_i^s \end{aligned} \tag{2.4}$$

where ρ^s , ρ^f are the particle and the fluid densities, g_i is the gravitational acceleration, f_i is an external volume force that drives the flow, and p is the fluid pressure. τ_{ij}^f is the fluid stress (viscous stress and fluid Reynolds stresses), p^s is the normal stress of particles and τ_{ij}^s their shear stress. M_i^{sf} and M_i^{fs} are the interphase momentum transfer including the drag efforts, the drift velocity and the pressure corrections (see equations 2.5 and 2.6). S_i^f and S_i^s are the Reynolds Averaged momentum source terms representing the hydrodynamic forces imposed on the flow by the rotation of the turbine, a theory is required to determine these terms which will be explained in chapter 3.

$$M_i^{sf} = \phi(1-\phi)K(u_i^f - u_i^s) - \frac{1}{S_c}(1-\phi)K\nu_t^f \frac{\partial \phi}{\partial x_i} \tag{2.5}$$

$$M_i^{fs} = -\phi(1-\phi)K(u_i^f - u_i^s) - \frac{1}{S_c}(1-\phi)K\nu_t^f \frac{\partial \phi}{\partial x_i} \tag{2.6}$$

The two terms in 2.5 and 2.6, containing the drag parameter K and the Schmidt number S_c in right-hand side (RHS) represent the momentum coupling between the fluid phase and particle phase by drag force, the second term especially designs the fluid turbulent

suspension term, also called drift velocity by Simonin (1991). Therefrom, ν_t^b is the turbulent viscosity to be calculated using a turbulence closure. The drag parameter K is modeled following Schiller and Naumann (1933):

$$K = 0.75 C_d \frac{\rho^f}{d_{eff}} ||u^f - u^s|| \beta^{-h_{Exp}} \tag{2.7}$$

where d_{eff} is the effective sediment diameter which multiply the particle diameter by the shape factor ψ.

The drag coefficient C_d presented in equation (2.7) depends on the particulate Reynolds number $Re_p = (1-\phi) \parallel u^f - u^s \parallel d_{eff}/\nu^f$, and calculated as:

$$C_d = \begin{cases} \frac{24}{Re_p}(1 + 0.15 Re_p^{0.687}), & Re_p \leq 1000 \\ 0.44\,, & Re_p > 1000 \end{cases} \tag{2.8}$$

2.2.2 Fluid phase shear stress

The total fluid stress presented in equation (2.4) consists of a large-scale Reynolds stress component R_{ij}^{ft} and a grain-scale stress r_{ij}^f, which represents the viscous stress of the turbulence generated in the fluid between the sediment particles or induced by fluctuations of the particles:

$$\tau_{ij}^f = R_{ij}^f + r_{ij}^f = \rho^f \beta [2\nu_{Eff}^f S_{ij}^f - \frac{2}{3} k \delta_{ij}] \tag{2.9}$$

where ν_{Eff}^f is the fluid-phase effective viscosity which is the sum of the fluid eddy viscosity and the mixture viscosity, k is the turbulent kinetic energy. S_{ij}^f depends on the Favre averaged strain-rate tensor, it is well explained in Chauchat et al. (2017) . The Reynolds stress tensor R_{ij}^f is modeled as :

$$R_{ij}^f = \rho^f (1-\phi)[2\nu_t^f S_{ij}^f - \frac{2}{3} k \delta_{ij}] \tag{2.10}$$

and the viscous stress tensor r_{ij}^f :

$$r_{ij}^f = 2\rho^f (1-\phi) \nu^{mix} S_{ij}^f \tag{2.11}$$

The turbulent eddy viscosity ν_t^f and the the mixture viscosity ν^{mix} presented in equations 2.10 and 2.11 are computed using turbulence and viscosity closures respectively, incorporating sediment effects. There are several multiphase turbulence models in the litterature (Chauchat and Guillou, 2008).

2.2.2.1 Mixture viscosity

In a case of pure fluid the mixture viscosity is equal to the fluid viscosity, $\nu^{mix} = \nu^f$. But when the particles exist even in a minimal concentration, a model is required to determine the viscosity of the mixture. There exist several viscosity models in litterature :

$$\frac{\nu^{mix}}{\nu^f} = 1 + 2.5\phi \tag{2.12}$$

In this work, the model proposed by Boyer et al. (2011) is used, it is appropriate with all types of mixture, either with low volume fraction of particles or with high volume fraction of particles, the formulation of the model depends on the maximum volume fraction ϕ_{max}:

$$\frac{\nu^{mix}}{\nu^f} = 1 + 2.5\phi(1 - \frac{\phi}{\phi_{max}})^{-1} \tag{2.13}$$

2.2.2.2 Turbulence modeling

To determine the turbulent eddy viscosity ν_t^f presented in equation 2.10, a turbulence closure is required. The present contribution is performed using the linear eddy viscosity models $k-\epsilon$ and $k-\omega$ turbulence models based on the linear relation between the Reynolds shear stress and the main rate tensor in equation 2.10.

$k-\epsilon$ model

Following (Hsu et al., 2004) the fluid phase eddy viscosity ν_t^f is given by:

$$\nu_t^f = C_\mu \frac{k^2}{\epsilon} \tag{2.14}$$

where C_μ is an empirical coefficient usually equal to 0.09 and ϵ is the fluid-phase turbulent dissipation rate. k and ϵ appear in the eddy viscosity formulation, it is required to introduce balance equations for both so that they are appropriate for sand particles in water:

$$\begin{aligned} \frac{\partial k}{\partial t} + u_j^f \frac{\partial k}{\partial x_j} &= \frac{R_{ij}^{ft}}{\rho^f}\frac{\partial u_i^f}{\partial x_j} + \frac{\partial}{\partial x_j}[(\nu^f + \frac{\nu_t^f}{\sigma_k})\frac{\partial k}{\partial x_j}] - \epsilon \\ &- \frac{2K(1-t_{mf})\phi k}{\rho^f} - \frac{1}{S_c(1-\phi)}\nu_t^f \frac{\partial \phi}{\partial x_j}(\frac{\rho^s}{\rho^f} - 1)g_j \end{aligned} \tag{2.15}$$

The above k-equation is similar to the uniform fluid $k-\epsilon$ closure, the first three terms on the right hand side describe respectively production, diffusion and dissipation of TKE.

The last two terms on the RHS represent the effects induced by the presence of particles. The last term accounts for the sediment damping effect on the carrier flow turbulence through density stratification. It can be seen as the buoyancy production/dissipation due to sediment-induced density stratification (Kranenburg et al., 2014). The fourth term in RHS is a damping term that models the drag-effect on the carrier flow turbulence of sediment particles that cannot completely follow the turbulent fluid velocity fluctuations due to particle inertia. In this term, t_{mf} is a parameter to characterize the degree the particles follow the fluid fluctuation. t_{mf} is the ratio between the ensemble averaged correlation of fluid and particle velocity fluctuations and the ensemble averaged correlation of the fluid velocity fluctuation with itself. Following (Kranenburg et al., 2014), t_{mf} has a value between 0 and 1, where t_{mf} = 1 denotes completely passive particles, yielding no drag-induced turbulence damping. Chen and Wood (1985) proposed an exponential function for t_{mf}:

$$t_{mf} = e^{-B.St} \tag{2.16}$$

where B is an empirical coefficient. The degree of correlation between particles and fluid velocity fluctuations can be quantified by the Stokes number S_t:

$$S_t = \frac{t_p}{t_l} \tag{2.17}$$

where $t_p = \rho^s/((1-\phi)K)$ is the particle response time, t_l is the characteristic time scale of energetic eddies.

The rate of turbulent energy dissipation ϵ_f is assumed to be governed by an equation similar to that for a clear fluid (Elghobashi and Arab, 1983) :

$$\begin{aligned} &\frac{\partial \epsilon}{\partial t} + u_j^f \frac{\partial \epsilon}{\partial x_j} = C_{1\epsilon}\frac{\epsilon}{k}\frac{R_{ij}^{ft}}{\rho^f}\frac{\partial u_i^f}{\partial x_j} + \frac{\partial}{x_j}[(\nu^f + \frac{\nu_t^f}{\sigma_\epsilon})\frac{\partial \epsilon}{\partial x_j}] - C_{2\epsilon}\frac{\epsilon^2}{k} \\ &-C_{3\epsilon}\frac{\epsilon}{k}\frac{2K(1-t_{mf})\phi k}{\rho^f} - C_{4\epsilon}\frac{\epsilon}{S_c k(1-\phi)}\nu_t^f\frac{\partial \phi}{\partial x_j}(\frac{\rho^s}{\rho^f}-1)g_j \end{aligned} \tag{2.18}$$

Due to the lack of information regarding the appropriate values of numerical coefficients in the present $k-\epsilon$ model, the question asked here is how to include the effect of sediment on the carrier flow turbulence: Hsu et al. (2004) adopted a particle concentration and inertia dependent $C_{\epsilon 2}$, and employ the same coefficients as those implemented in the standard $k-\epsilon$ model for a clear fluid flow.

Standard $k-\omega$ model

It is well-known that the original $k-\epsilon$ model has been derived for high Reynolds number flows and is not very accurate to describe transitional flows because for moderate

Reynolds number, the flow behaves in different manners in terms of the frictional energy loss.

The two-phase $k-\omega$ turbulence model presented here is based on the work of Chauchat and Guillou (2008); Hsu et al. (2004) for the $k-\epsilon$ model presented in the previous section. Following the same method of developing the two-phase $k-\epsilon$ turbulence model for sediment transport, the modification to the equations for the fluid TKE (see equation 2.19), and the fluid specific rate of turbulent energy dissipation ω (see equation 2.20) are made by adding the effect of the particle phase presence to the clear fluid $k-\omega$ model such as the particle drag and the buoyancy terms. The particle drag-effect is computed in the fourth term in equation 2.19 and the buoyancy production/dissipation due to sediment-induced density stratification is computed in the lest term in equation 2.19.

$$\begin{aligned}\frac{\partial k}{\partial t}+u_j^f\frac{\partial k}{\partial x_j}=R_{ij}^{ft}\frac{\partial u_i^f}{\partial x_j}+\frac{\partial}{\partial x_j}[(\nu^f+\nu_t^f\sigma_k)\frac{\partial k}{\partial x_j}]-C_\mu k\omega\\ -\frac{2K(1-t_{mf})\phi k}{\rho^f}-\frac{1}{S_c(1-\phi)}\nu_t^f\frac{\partial\phi}{\partial x_j}(\frac{\rho^s}{\rho^f}-1)g_j\end{aligned} \tag{2.19}$$

$$\begin{aligned}\frac{\partial\omega}{\partial t}+u_j^f\frac{\partial\omega}{\partial x_j}=C_{1\omega}\frac{\epsilon}{k}\frac{R_{ij}^{ft}}{\nu_t^f}\frac{\partial u_i^f}{\partial x_j}+\frac{\partial}{\partial x_j}[(\nu^f+\nu_t^f\sigma_\omega)\frac{\partial\epsilon}{\partial x_j}]-C_{2\omega}\omega^2+CD_{k\omega}\\ -C_{3\omega}\frac{2K(1-t_{mf})\phi\omega}{\rho^f}-C_{4\omega}\frac{\omega}{S_ck(1-\phi)}\nu_t^f\frac{\partial\phi}{\partial x_j}(\frac{\rho^s}{\rho^f}-1)g_j\end{aligned} \tag{2.20}$$

2.2.3 Particle phase stress

The sediment pressure p^s presented in equation 2.3 is an important factor to determine the mechanisms to support a particle's immersed weight in concentrated regions of sediment transport. In this region, there are also momentum exchanges between particles due to the collisions contacts that can influence the total stress of particles in the collection. The particle phase stress involve the particle normal stress or pressure p^s and the particle shear stress τ_{ij}^s. The particle pressure is classified into two contributions: a shear-induced or collisional component p^{ss} and a permanent contact component p^{ff} (Johnson and Jackson, 1987).

$$p^s=p^{ff}+p^{ss} \tag{2.21}$$

p^{ff} represents the particle pressure due to the enduring contact between particles in a concentrated region when the particles are quasi static. This term is important to prevent the unphysical sediment concentration in the sediment bed when the sediment concentration

is close to its maximum packing limit. It is calculated as:

$$p^{ff} = \begin{cases} 0, \ \phi < \phi_{min}^{Fric} \\ Fr\frac{(\phi-\phi_{min}^{Fric})^{\eta_0}}{(\phi_{max}-\phi)^{\eta_1}}, \ \phi \geq \phi_{min}^{Fric} \end{cases} \tag{2.22}$$

where ϕ_{min}^{Fric} = 0.57, $\phi_{max} = 0.635$ for spheres and Fr, η_0 and η_1 are empirical coefficients. Many closures exist in litterature to determine the particle phase shear stress. In the modern sediment transport modeling framework, there are two major approach for modeling the particle shear stress: the kinetic theory and the dense granular flow rheology.

2.2.3.1 Kinetic theory for granular flow

Classical kinetic theory considers sheared granular bodies, in which grains are supported exclusively by mutual binary collisions. Constitutive relations are formulated for local grain stresses (normal and shear) and for a balance of grain fluctuation energy in the collisional regime.

The kinetic theory approach used in the present work, is mostly accurate for low to moderate sediment concentration configurations, it computes the binary collisions in the interactions between particles. The granular temperature Θ, which represents the particle velocity fluctuations, is the important term in this model to determine the collisional shear stresses between particles. The model is developped by Jackson (2000), Lun and Savage (1987), Ding and Gidaspow (1990) and the last one is used in the present work. The balance equation for granular temperature is:

$$\frac{3}{2}[\frac{\partial\phi\rho^s\Theta}{\partial t} + \frac{\partial\phi\rho^s u_j^s\Theta}{\partial x_j}] = P - \frac{\partial q_j}{\partial x_j} - \gamma + J_{int} \tag{2.23}$$

where $P = (-p^s\delta_{ij} + \tau_{ij}^s)\frac{\partial u_i^s}{\partial x_j}$ is the production term of granular temperature, q_j is the flux of granular temperature, γ is the energy dissipation rate due to inelastic collision and J_{int} is the production/dissipation due to the interaction with the carrier fluid phase, since the carrier flow turbulence can induce particle fluctuations.

Since the Kinetic Theory involves the modeling of particle stresses, Ding and Gidaspow (1990) have suggested the closure for particle collisional pressure:

$$p^s = \rho^s\phi[1 + 2(1+e)\phi g_{s0}]\Theta \tag{2.24}$$

where e is the coefficient of restitution during the collision. g_{s0} represents the radial distribution function that computes the crowdedness of particles, it can be calculated by:

$$g_{s0} = \frac{2-\phi}{2(1-\phi)^3} \tag{2.25}$$

Gidaspow (1994) proposed the formulation of particle collisional stress:

$$\tau^s s_{ij} = \mu^s S^s_{ij} + \lambda \frac{\partial u^s_k}{\partial x_k} \sigma_{ij} \tag{2.26}$$

where S^s_{ij} is the sediment phase strain rate tensor (Chauchat et al., 2017), μ^s is the particle shear viscosity and λ is the bulk viscosity. There are many authors in litterature that proposed closures to determine the particle shear viscosity, like the formulation of μ^s dependent on the sediment phase concentration and viscosity of the mixture. The closure proposed by Gidaspow (1994); Chauchat and Médale (2014) is used in the present work:

$$\mu^s = \rho^s d \sqrt{\Theta} [\frac{4}{5} \frac{\phi^2 g_{s0}(1+e)}{\sqrt{\pi}} + \frac{\sqrt{\pi} g_{s0}(1+e)(3e-1)\phi^2}{15(3-e)} + \frac{\sqrt{\pi}\phi}{6(3-e)}] \tag{2.27}$$

For more information regarding the other terms presented in equation (2.27), please refer to Bonamy et al. (2017); Cheng et al. (2017).

Finally, the total shear stress can be determined as a sum of the collisional-kinetic component that is calculated previously in equation (2.26, and a frictional shear stress component due to frictional contact:

$$\tau^s_{ij} = \tau^{ss}_{ij} + \tau^{ff}_{ij} \tag{2.28}$$

The frictional shear stress is added to take into account not only the collisional contact but also the interactions between particles driven by frictional shearing contact when the bed is quasi-static, it can be modeled as:

$$\tau^{ff}_{ij} = -2\rho^s \nu^s_{Fr} S^s_{ij} \tag{2.29}$$

ν^s_{Fr} presented in equation above is the frictional viscosity (Srivastava and Sundaresan, 2003):

$$\nu^s_{Fr} = \frac{p^{ff} \sin(\theta_f)}{\rho^s (||S^s||^2 + D^2_{small})^{1/2}} \tag{2.30}$$

where θ_f is the internal frictional angle.

2.2.3.2 Dense granular flow rheology

As noticed in the previous section, the kinetic theory model is more accurate for low dense flow, otherwise, this section treats the shear induced particle normal stress and shear stress modelling in the high concentrated flows in sediments, using the dense granular flow rheology or the $\mu(I)$ rheology developped by Forterre and Pouliquen (2008a);

Chauchat and Médale (2014) and applied by Bonamy et al. (2017) ...

The total particle phase shear stress can be calculated as:

$$\tau_{ij}^{s} = R_{ij}^{s} + r_{ij}^{s} \tag{2.31}$$

where R_{ij}^{s} represents a solid-phase Reynolds stress and r_{ij}^{s} is the granular stress contribution defining the interactions between particles. Since this section consists on determining the additional source terms to the turbulence model equations, to incorporate the effects of the dispersed phase on the turbulence, following Rusche these source terms are related to the coefficient C_t which is defined as the ratio of the velocity fluctuations of the dispersed phase $u_a^{'}$ to those of the continuous phase $u_b^{'}$:

$$C_t = \frac{u_a^{'}}{u_b^{'}} \tag{2.32}$$

This leads to determine the formulation of Reynolds stress and granular contributions as followings:

$$R_{ij}^{s} = \rho^{s}\phi[C_t^2 \nu_t^f S_{ij}^{s} - \frac{2}{3}C_t^2 k\sigma_{ij}] \tag{2.33}$$

$$r_{ij}^{s} = \nu_{Fr}^{s} S_{ij}^{s} \tag{2.34}$$

where ν_{Fr}^{s} is the frictional viscosity and it is defined by (Chauchat et al., 2017) as following:

$$\nu_{Fr}^{s} = min(\frac{p^{ss}\mu(I)}{\rho^{s}(||S^{s}||^2 + D_{small}^2)^{1/2}}, \nu_{max}) \tag{2.35}$$

ν_{max} is the maximum solid phase viscosity that can ensure the numerical stability when clipped with ν_{Fr}^{s}, $||S^{s}||$ is the norm of the shear rate tensor.

They have involved a computation that leads to the formulation of the shear induced pressure depending on the dilatancy law $\phi(I)$ (Boyer et al., 2011) as following:

$$p^{ss} = (\frac{B_\phi \phi}{\phi_{max} - \phi})^2 \rho^{s} d||S^{s}||^2 \tag{2.36}$$

And finally, the shear induced pressure p^{ss} can be introduced in the equation (2.21) to determine the total particle pressure p^{s}.

2.3 Numerical Implementation

The numerical implementation of the present Eulerian two-phase flow sediment transport model is involved by Bonamy et al. (2017) into a numerical code called 'SedFoam' based on an open-source finite volume CFD library providing the numerical discretization schemes, solvers and the framework of Finite Volume Method (FVM), this latter is presented in details in the next chapter. SedFoam is a two-phase Eulerian-Eulerian multidimensional code for sediment transport modeling. More precisely, it is a solver written in the OpenFOAM toolbox, coded in $C++$. SedFoam is developed by a team from the Geophysical and Industrial Flows Laboratory (France) and the Center for Coastal Applied Research at the University of Delaware (USA). SedFoam is based on the twoPhaseEulerFoam code (Rusche; Cheng et al., 2016) and compatible with several versions of OpenFOAM (Nagel, 2019). The numerical implementation is similar to the one described in (Chauchat and Guillou, 2008). The main difference is the pressure solver used. In the present numerical implementation, the pressure solver iterates on the reduced pressure p :

$$p^* = p - \rho^f gh \tag{2.37}$$

where p is the total pressure and $\rho^f gh$ is the hydrostatic pressure. This way of solving the pressure system makes the solver more stable and similar to what is done in other validated OpenFOAM solvers such as interFoam (Deshpande et al., 2012). More details concerning SedFoam is available in (Nagel, 2019).

The numerical solution procedure for the proposed two-phase flow model is outlined as follow :

1. Solve for sediment concentration ϕ ;
2. Update the volume concentration of the fluid $1 - \phi$;
3. Update the drag parameter K in the drag term ;
4. Solve for the fluid turbulence closure, update k, ϵ or ω (depending on the turbulence closure $k - \epsilon$ or $k - \omega$, and then calculate the eddy viscosity and effective fluid total viscosity ;
5. Solve for the particle phase stress (Kinetic Theory model or the dense granular rheology) ;
6. PISO-loop, solving velocity-pressure coupling for N loops.

In the above solution procedure, the velocity-pressure coupling steps are looped for N times, to avoid velocity-pressure decoupling caused by the direct solving method.

2.3.1 Model validation.

Different easy benchmarks/tutorials of one dimension are provided to illustrate the model capabilities: a sedimentation of spherical particles at low Reynolds number, the laminar bed-load problem, the turbulent sheet-flow regime. Moreover some advanced multi-dimensional cases/tutorials of two dimensions are proposed.

The most interesting benchmarks examples regarding the current subject of this thesis (since they involve the scour phenomenon), are the two dimensional scour modeling around a horizontal cylinder and the scour development downstream of an apron, following the numerical study of Cheng et al. (2017); Amoudry (2014). The sediment particles are made of medium sand, density ρ^s = 2650 kg/m^3 and diameter $d = 0.25$ mm. The fluid is water with density ρ^f = 1000 kg/m^3 and a kinematic viscosity of 10^{-6} m^2/s.

Figures 2.1 and 2.2 show the scour pattern occurred downstream the apron and under the cylinder respectively. The figure 2.1 shows two snapshots of sediment concentration contour during the scour process (t = 0 s and t = 20 s), using $k - \epsilon$ and kinetic theory. At t = 20 s, the development of a scour hole near the inlet can be identified.

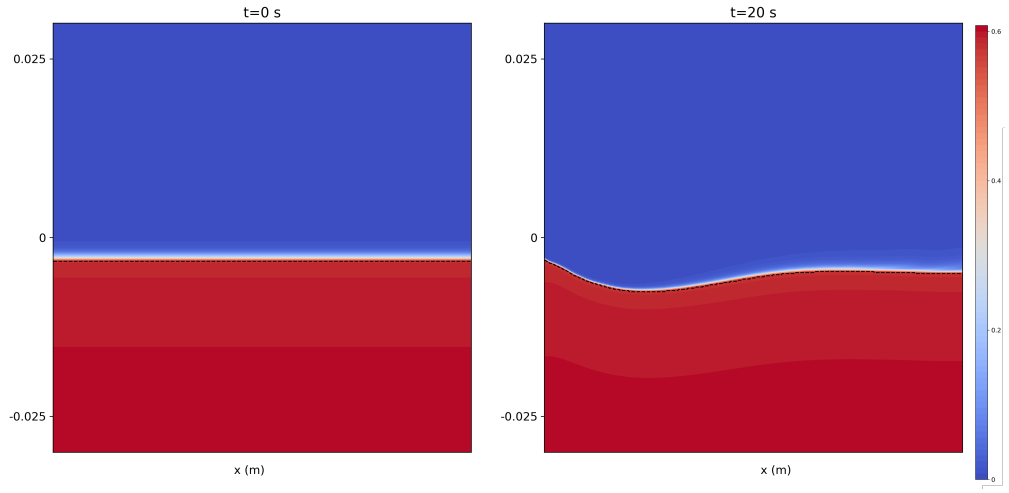

Fig. 2.1: Sediment concentration contour at different times during the scour process using a $k - \omega$ turbulence model and the granular rheology (Chauchat et al., 2017).

In the case of the $k-\epsilon$ coupled with the Kinetic Theory, ripples generated downstream of the apron are propagating. This is particularly clear at t = 20 s where a bed shape similar to a ripple can be observed. Figure 2.2 presents a good agreement between the SedFoam numerical results and the measurements of Mao (1986). A significant scour is noticed below the cylinder while a deposition term is occurred downstream the cylinder. The curves for both results follow the same evolution in each time either for the scouring or the deposition patterns. The sediments continue to erode below the cylinder during the time in fig. 2.2, the scour gets deeper and larger over time, however the deposition downstream the cylinder decreases. It means that the impact of the wake generated around the cylinder on the sediments becomes more important near its location, thus the eroded sediments have sufficient energy to be transported downstream the cylinder, although the numerical results predicted a higher elevation of deposition.

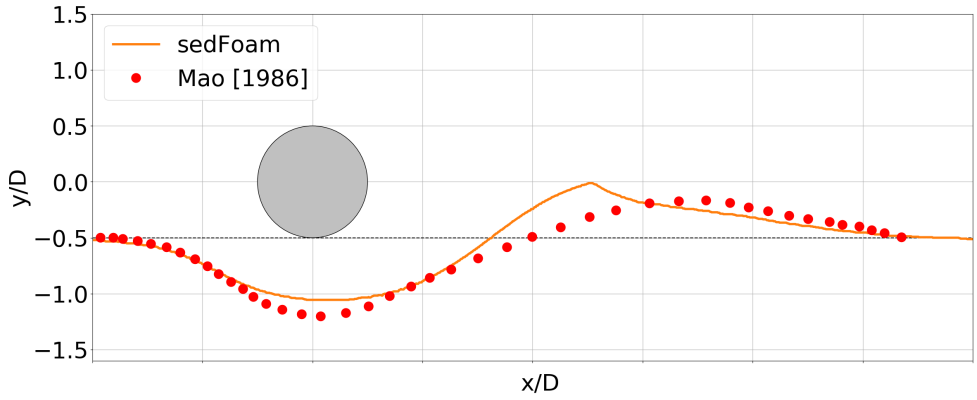

Fig. 2.2: Sediment bed profiles at 11s using a $k-\epsilon$ turbulence model (Chauchat et al., 2017).

2.4 Summary

In this chapter, the theories of the Eulerian-Eulerian two-phase flow model have been presented and a little glimpse of their implementation into a numerical code SedFoam in OpenFOAM is provided.

Also, the capability of the model SedFoam has been tested on several one and two-dimensional test cases in the literature. Hence, two applications on scour pattern are presented and they have illustrated the multi-dimensional capabilities of the solver. The scouring is well recovered by the model even if the results are sensitive to the choice of the inter-granular and turbulence models. However, rare are the applications involving the three dimensional scouring by SedFoam, chapter 4 provides the validation of the three dimensional scouring process, comparing the numerical results of a coupled model (SedFoam and the hydrodynamic models explained in chapter 3), with the experimental results of Hill et al. (2014).

Chapter 3

Modeling of the turbine

3.1 Introduction

In this chapter we present the theoretical elements that we used for the construction of a hybrid model based on the concept of the active disk of this thesis. We start with the presentation of the Actuator Disk (AD) theory, where the rotor is replaced by a disk of zero thickness and of diameter equal to the rotor. In practice, this disc will have a thickness e. Next, we present the model of Blade Element Momentum Theory (BEMT), which is used to determine the performance of the turbine and the forces applied by the flow on the turbine. Volumetric forces are calculated using the blade element theory and are distributed over a set of coaxial rings of radial thickness dr. The overall flow is calculated by the numerical resolution of the averaged turbulent Navier-Stokes equations. This flow provides in particular the local incident velocity at each blade of the turbine and makes it possible to evaluate the hydrodynamic forces applied to the active disk. This simplification is made to decrease the cost of computation by decreasing the number of cells of the mesh. Due to its geometrical simplicity, it suffices to mesh an active disk and its environment, the time devoted to the realization of the meshes is much shorter. We validate our model using experimental data from Mycek et al. (2014).

3.2 Hydrodynamic models

3.2.1 Actuator Disk

This model is based on the simplifications initially developed for wind turbines to represent the devices, and compute their effects in the flow hydrodynamics. It is the simplest of its range and therefore represents a necessary first step before the development of more complex models such as BEMT.

The fundamental bulk of the actuator disk methodology is to replace the physical geometry of a rotor with only its effect on the flow. This is done by inserting the rotor forces as source terms S_i into the momentum equations of the governing Navier-Stokes equations.

Its principle is to average the effects induced by the turbine on a disc which represents the surface swept by its blades during its rotation, and to distribute it over the disk volume. Figure 3.1 shows a schematic view of the average flow around a turbine considered as an uniform disc. These effects are represented by a volume force as a function on the one hand of the area S of the disc and on the other hand of the pressure jump which depends on the speed upstream of the disc U_∞, on the density fluid ρ and the thrust coefficient C_T.

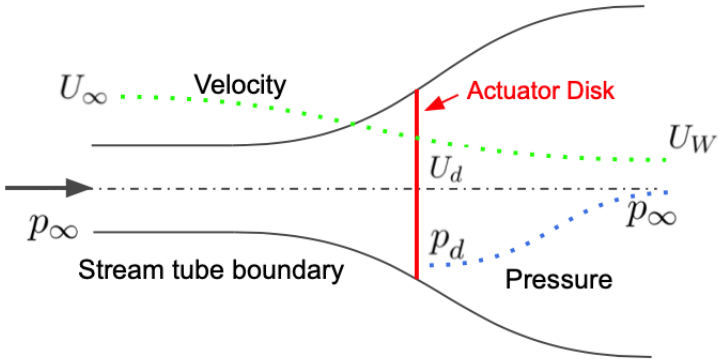

Fig. 3.1: Stream tube passing through a turbine represented by an actuator disk.

Let us therefore introduce an important parameter of this theory: the axial induction factor a (or factor influencing the translation movement). This factor directly describes the percentage of axial velocity deficit between the rotor velocity and the downstream velocity:

$$U_d = U_\infty(1 - a) \tag{3.1}$$

$$U_w = U_\infty(1 - 2a) \tag{3.2}$$

To determine the thrust effort $F = S\Delta P$ applied on the disk, the pressure jump ΔP between the pressure at disc level p_d and the upstream pressure p_∞ is deduced from the Bernoulli's law applied throughout the stream line of the stream tube in figure 3.1, note that p_d^- is the pressure on the near upstream of the disk and p_d^+ on the other side of the disk:

$$p_d^- = p_\infty + 0.5\rho(U_\infty^2 - U_d^2) \tag{3.3}$$

$$p_d^+ = p_\infty + 0.5\rho(U_w^2 - U_d^2) \tag{3.4}$$

It is now possible to obtain two expressions of the axial force F:

$$F = S\Delta P = 0.5S\rho U_\infty^2 4a(1-a) \tag{3.5}$$

$$F = 0.5S\rho U_d^2 \frac{4a}{1-a} \tag{3.6}$$

so the thrust coefficient C_t is defined as:

$$C_t = \frac{F}{0.5\rho S U_\infty^2} = 4a(1-a) \tag{3.7}$$

concerning the power coefficient C_p:

$$C_p = \frac{P}{0.5\rho S U_\infty^3} = 4a(1-a)^2 \tag{3.8}$$

since the recovered power P can be written as following:

$$P = 0.5\rho S U_\infty^3 4a(1-a)^2 \tag{3.9}$$

C_p is also called turbine efficiency. It measures the power P absorbed by the turbine converted to the kinetic power delivered by the flow through the section S in the absence of the rotor. Figure 3.2 shows the evolution of C_T and C_p in function of the induction factor a. The maximum power coefficient is obtained for $a = 1/3$ and equal approximately to $16/27 = 0.59$. It means that a rotor cannot recover more than 60% from the kinetic energy of the upstream flow. This is the limit of Betz (fig. 3.2). The corresponding drag coefficient is $8/9 = 0.89$. For $a = 1/2$, the drag coefficient reaches the maximum value of 1. Beyond $a = 1/2$, the drag decreases. In reality, the solution is not physical because the upstream velocity U_a in the wake will be negative. Practically, this theory is invalid when a is greater than 0.4.

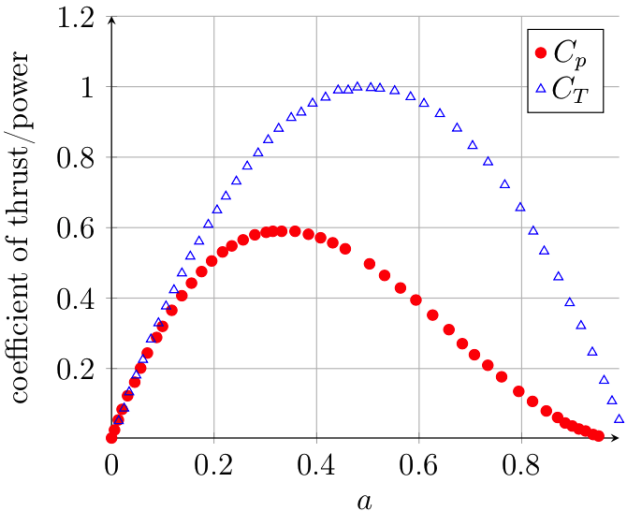

Fig. 3.2: Power and drag coefficients in function of the induction factor a.

As it is difficult to define the upstream velocity of a turbine in an array, when the upstream velocity of next devices cannot be determined easily, Nguyen et al. (2016) used the local velocity U_d at the disk location. This implies a modification of the force relation. The first step is to rewrite the pressure jump as a function of the local dynamic pressure depending on the fluid velocity at the disk U_d and a resistance coefficient K. Considering the disk as a thin porous media the upstream velocity could be link to U_d, and the thrust coefficient can be link to the resistance coefficient.

$$p_d^- - p_d^+ = \frac{1}{2}\rho K U_a^2 \tag{3.10}$$

Assuming that the disk is located in a perpendicular position to the streamwise direction, U_∞ is not equal to the average streamwise velocity, because the disk will slow down the flow in the near upstream section of it, then the velocity is defined as:

$$U_a = U_d(1 + \frac{1}{4}K) \tag{3.11}$$

and the thrust coefficient C_t is defined as:

$$C_t = \frac{K}{(1 + \frac{1}{4}K)^2} \tag{3.12}$$

The force acting on the disk could be link to K and U_d. An equal distribution of the force on the entire disk of thickness e and diameter D leads to the following source term (Nguyen et al., 2016):

$$S_i = \frac{\rho K U_d^2}{2e} \tag{3.13}$$

Given that many of these assumptions do not hold in the numerical model, or the real world, it is vital to verify the implementation and to validate the outcome from the model against laboratory and real world data. Nguyen et al. (2016) have validated the model with the experimental results of (Batten et al., 2013). The simulations are in agreement with the results especially in the far wake of the turbine.

This approach is obviously computationally cheaper than simulating an entire rotor blade geometry, but the resulting rotor wake will only capture the time-averaged effects of the entire rotor on the flow field. Additionally, this approach cannot account for flow separation in the blades or other $3D$ effects such as tip vortices, or hub horseshoe vortices.

3.2.2 Blade Element Momentum Theory

The most widely used method to calculate the load applied by the flow on the turbine and the behavior of the turbine, consists in using the balance of the amount of movement applied to a Blade Element Theory. This method is based on dividing the flow into annular control volumes of thickness d_r, to which the momentum equations are applied. Each ring is independent from others since each of the blade elements has a different rotational speed and geometric characteristics hence experiencing a slightly different flow.

The Blade element theory is combined with momentum theory to alleviate some of the difficulties in calculating the induced velocities at the rotor. It accounts for the angular momentum of the rotor and the geometry characteristics like chord and twist distributions of the blade airfoil.

The main assumptions of this method are:

1. the induced velocity in the plane of rotation is equal to half the downstream induced velocity ;

2. we can analyze the flow by dividing the blade into a number of independent elements and that the force of a blade element is solely responsible for the variation in the movement of the water which pass through the ring swept by this element ;

3.2.2.1 Blade Element Theory

In this theory, the forces acting on a blade element are calculated using the lift and drag characteristics of a two-dimensional profile. These characteristics are obtained using the angle of attack determined from the relative velocity of the flow in the plane perpendicular to the blade element (the velocity V_r fig. 3.3). We consider a turbine with n' blades, their radius is R, their chord is c, and the pitch angle is β measured between the zero lift line of the profile and the plane of rotation. The speed of rotation of the blade is ω, the

upstream velocity is V_{axial}. ωr is the tangential velocity of the blade element while the axial induction factors a and tangential a' are used to obtain the relative velocity of the flow, we can write:

$$V_r = \sqrt{V_{axial}^2(1-a)^2 + r^2\omega^2(1+a')^2} \tag{3.14}$$

We can also derive the following relations:

$$sin\phi = \frac{V_{axial}(1-a)}{V_r}, cos\phi = \frac{\omega r(1+a')}{V_r} \tag{3.15}$$

The angle of incidence:

$$\alpha = \phi - \beta \tag{3.16}$$

The lift force generated by a blade element of thickness d_r, normal to the direction of V_r is:

$$dL = 0.5\rho c d_r V_r^2 C_L F_{tip} \tag{3.17}$$

And the drag force parallel to V_r is:

$$dD = 0.5\rho c d_r V_r^2 C_D \tag{3.18}$$

where c is the chord of the blade which varies in function of radius, C_L and C_D are lift and drag coefficient respectively, their values depend on the geometry of the blade (angle of attack). F_{tip} is the Prandtl's Loss Factor correction which is introduced to correct the loading for finite number of blades (El khchine and Sriti, 2017).

The lift and drag forces generated by a blade element of thickness dr, are rotated into the rotor cylindrical coordinate system to obtain axial and tangential force components:

$$dF_x = dL\cos\phi + dD\sin\phi \tag{3.19}$$

$$dF_\theta = -dD\cos\phi + dL\sin\phi \tag{3.20}$$

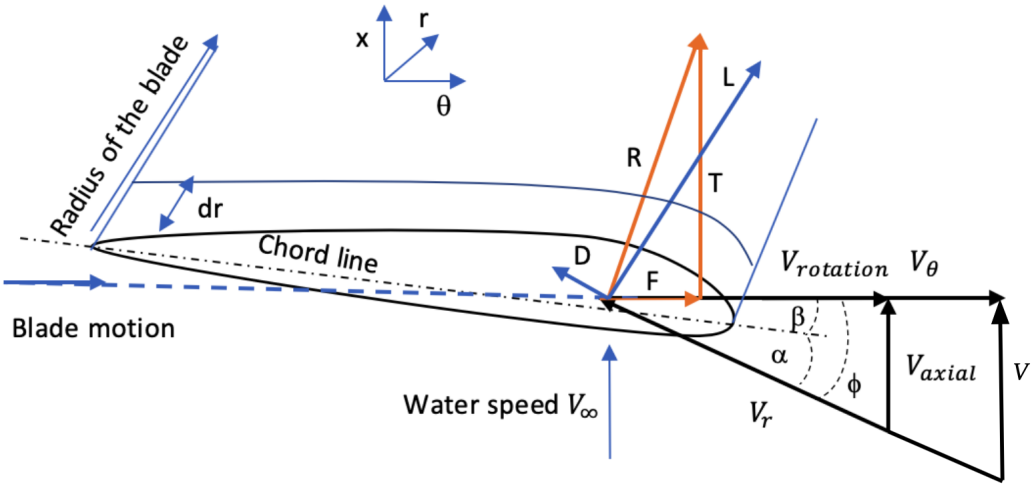

Fig. 3.3: Flow velocities and forces acting on the blade by BEMT.$V = V_{axial}(1-a)$, V_θ are the axial and tangential velocity components, β is the blade twist angle, α the angle of attack, ϕ the inflow angle.

3.2.2.2 Momentum Theory on each blade element

The study allows to evaluate the resultant hydrodynamic forces of n blade elements in the axial direction at radius r:

$$dN = \frac{1}{2}\rho V_r^2 nc(C_x sin\phi + C_z cos\phi)dr \tag{3.21}$$

On the other hand, this same result is equal to the variation in the amount of axial movement of the fluid passing through a ring of radius r, hence:

$$dN = 4\pi\rho V_{axial}^2 a(1-a)rdr + \frac{1}{2}\rho(2a'\omega r)^2 2\pi r dr \tag{3.22}$$

where we have taken into account the axial contribution of the variation in the amount of motion produced by the tangential induction factor.

We can carry out the same study on the torques and the angular momentum variation. The torque applied on the blade elements at radius r is written as:

$$dC = \frac{1}{2}\rho cn(C_z sin\phi - C_x cos\phi)V_r^2 r dr \tag{3.23}$$

and the variation of the angular momentum of the fluid passing through an element of the disc is:

$$dC = \rho V_{axial}(1-a)\omega r 2a' r 2\pi r dr = 4\pi\rho V_{axial}(\omega r)a'(1-a)r^2 dr \tag{3.24}$$

The correction of Prandtl F_P is determined according to the following equation:

$$F_P = \frac{2}{\pi} arccos(e^{(-\frac{n(R-r)}{2rsin\pi})}) \tag{3.25}$$

It is then sufficient to integrate these elementary forces and torques along the radius of the blade to obtain the overall performance of the hydrokinetic turbine.

The momentum source terms added to the momentum equations are determined from the lift and the drag forces acting on each blade. The momentum sources are computed based on the time-averaged blade forces imparted by the blade onto the fluid. The source term S_i is projected in regards to cylindrical coordinate system S_x and S_θ such as:

$$S_x = -\frac{nf_x}{2\pi re} \tag{3.26}$$

$$S_\theta = -\frac{nf_\theta}{2\pi re} \tag{3.27}$$

The total thrust T and power P are calculated by numerical integration of the sources over the disc region in cartesian coordinate system. The model is integrated numerically in OpenFOAM as a $C++$ code.

3.3 Numerical implementation in OpenFOAM

This section describes the specific implementation of BEMT in the OpenFOAM environment. The description contained in this Section will provide an overview of the code structure, as well as the integration of the method with the flow solver in OpenFOAM. As previously described above, the BEMT essentially introduces momentum sources in the cells that collectively make up the rotor disk region. Therefore, the description of the implementation of this model in OpenFOAM will begin by describing how these additional momentum sources are incorporated into the global fluid momentum equations that are solved by the RANS solvers.

In order to understand the way in which the OpenFOAM library and solvers work, some background knowledge of $C++$, the base language of OpenFOAM, is required. However, the OpenFOAM User Guide and Programming Guide provide a good overview of the general code structure, the use of object-orientation paradigm in OpenFOAM, and several base classes and operators used in OpenFOAM.

3.3.1 Overview of RANS solvers in OpenFOAM

The standard OpenFOAM distribution includes a collection of flow solvers. These flow solvers are the top-most level executable files in OpenFOAM, and are differentiated based on the flow physics that are being solved. Table 3.1 provides a set of examples of the variety of OpenFOAM standard solvers that are typically used in the IRSA group. Note that the standard OpenFOAM distribution includes a larger number of standard solvers than that shown in table 3.1. The momentum sources introduced by the models will be implemented in the flow solver through the use of the class "basicSource".

The BEMT code developed in OpenFOAM comprises multiple $C++$ classes. The file structure grouped by the class name is shown in figure 3.4. Calculation of the blade forces and momentum source terms using the methodology outlined in Section above is implemented in the main class, "rotorDiskSource".

Table 3.1: List of standard OpenFOAM flow solvers

Basic CFD Solver
laplacianFoam: Solves a simple Laplace equation, e.g. for thermal diffusion in a solid. **potentialFoam**: Simple potential flow solver which can be used to generate starting fields for full Navier-Stokes codes.
Incompressible Flow Solvers
boundaryFoam: Steady-state solver for incompressible, 1D turbulent flow, typically to generate boundary layer conditions at an inlet, for use in a simulation. **icoFoam**: Transient solver for incompressible, laminar flow of Newtonian fluids. **simpleFoam**: Steady-state solver for incompressible, turbulent flow based on SIMPLE algorithm. **SRFSimpleFoam**: Steady-state solver for incompressible, turbulent flow of non-Newtonian fluids in a single rotating frame. **pisoFoam**: Transient solver for incompressible flow based on PISO algorithm.

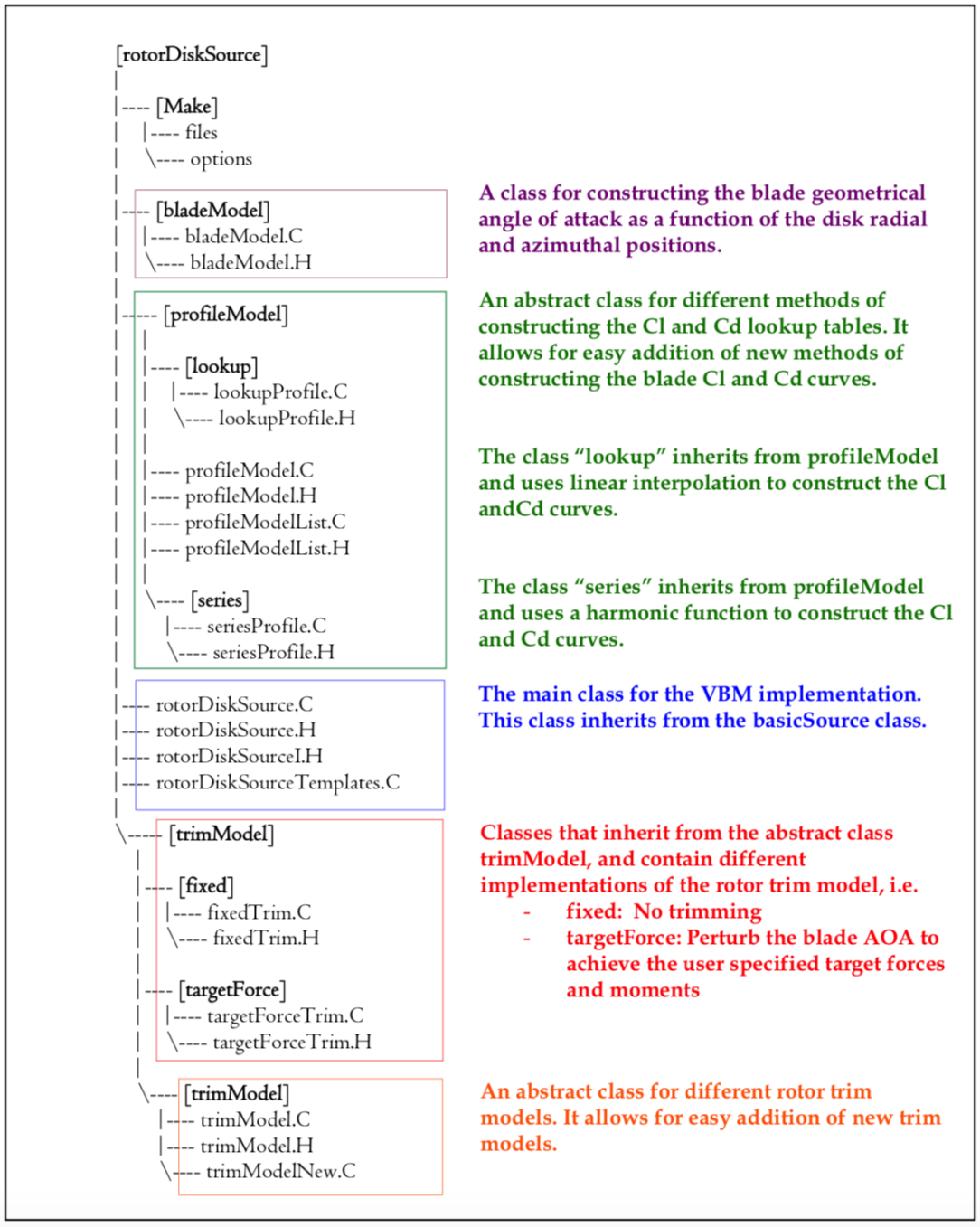

Fig. 3.4: Overview of the directory and file structure of the BEMT source code in OpenFOAM [1].

Interested users and readers are recommended to further explore the functionality provided by the basicSource class by reviewing its source code. One of the major advantages of using the basicSource class as a template abstract class for deriving the BEMT library is that multiple source term objects of different kind can be taken into consideration in the simulation. This means that the simulation can include multiple rotor disks, multiple

[1] *https://www.openfoam.com*

heat source terms, and multiple porosity terms. Some examples of such derived classes are rotorDiskSource (BEMT), actuationDiskSource (momentum sink) and porousMedia (porosity momentum sink).

3.3.2 RotorDiskSource

This section provides an overview of rotorDiskSource class. The OpenFOAM distribution does not have a Graphical User Interface that may help the user in simulating a case, contrary to other commercial CFD packages, such as ANSYS. Case preparation in OpenFOAM requires the manual preparation of all the required input and mesh files. Besides, the required files and formats vary significantly depending on the OpenFOAM solvers and Boundary Conditions to be used. Thus, to limit the wide explanation of OpenFOAM libraries that can be found in literature, only the case set up relevant to running an unsteady RANS simulation using the rotorDiskSource will be discussed.

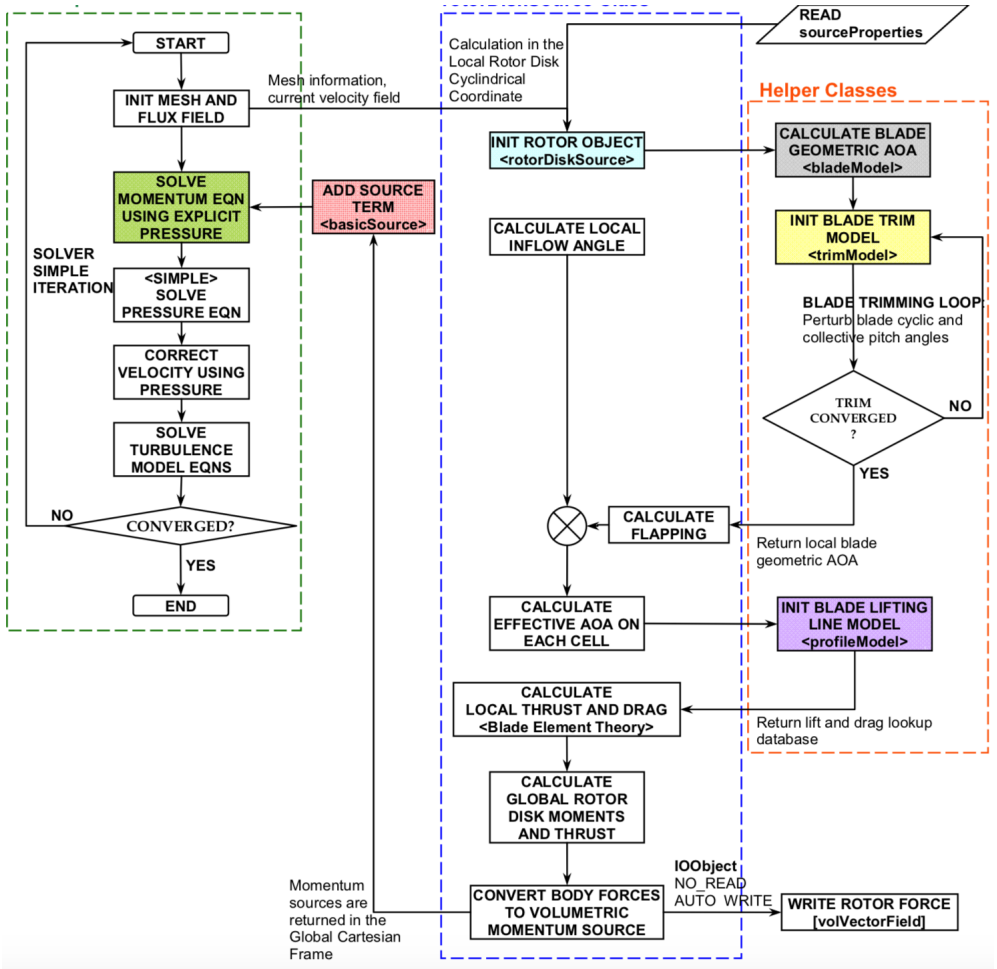

Fig. 3.5: Implementation of the BEMT using rotorDiskSource class and sedFoam solver in OpenFOAM [2].

Vertical profiles of the axial velocity dimensionless by the fluid velocity (Ux/U), downstream the turbine; blue for numerical BEMT results and red for the mea- surements of Mycek et al. (2014). The rotorDiskSource class contains both data and member functions that are needed to implement the BEMT. It contains the variables or parameters (rotor rmp, blade pitch angle, etc.) that are needed for the BEMT calculation. These data are not available for access from outside of this class. The private data have also been designed to be read as user inputs, which means that when the solver sedFoam is run, the basicSource object in the solver will look for a "dictionary" file in the case directory structure. The dictionary file for the source is called sourceProperties, and must be placed in the constant directory of the case.

The rotorDiskSource class is activated at runtime if the solver finds a fvOptions file containing a rotorDisk type entry. Since the solver sedFoam is not compatible with basic sources of fvOptions, we have made some changes and we have added the library of the sources to the code. So that the solver can compile any basic source. A flowchart showing the implementation of the rotorDiskSource class in the OpenFOAM sedFoam solver is shown in fig.3.5. The class declaration and definition for rotorDiskSource is given in the rotorDiskSource.H. The main implementation of the class is given in the rotorDiskSource.C. Some files from the rotorDiskSource class are described below, but the most important file is rotorDiskSourceTemplates.C because it contains the code of the source terms representing the rotor forces.

- rotorDiskSource.H: This is the main class declaration file, based on the abstract base class cellSetOption that is based in turn on the fvOption class. This file provides the main rotor properties such as number of blades, rotational velocity, and constructor functions.

- rotorDiskSource.C: This file is the latest one in the file series in determining the source terms. It contains the definition of functions for reading the fvOptions file entries, calculating the area of each cell face of the rotor mesh, constructing the rotor coordinate system, and adding the source terms to the momentum equation that is compiled with sedFoam solver.

- rotorDiskSourceTemplates.C: The essential role of the code in this file is to calculate the actual value of the source terms using the methodology described in the theory of BEMT section.

- bladeModel: This folder contains two files bladeModel.H and bladeModel.C, the code contains the member functions that interpolate values for twist and chord for a radial position of a cell inside the rotor volume, taking into consideration the blade data provided by the user in inputs such as radius, twist, and chord (example 3.2).

- profileModel: profileModel class contains data on the lift and drag coefficients for each blade section. The code contains the member functions that interpolate values for

lift and drag coefficients for a radial position of a cell inside the rotor volume, taking into consideration the data provided by the user in inputs such as lift and drag coefficients in function of an elementary radius (example 3.4).

- trimModel: In this class, we can simulate a blade model with variation of blade angles to reach a certain target thrust or torque. Throughout this thesis, a fixed blade with constant blade angles is used.

Table 3.2: Detailed blade profile description implemented in rotorDiskSource.

profiles	radius (m)	Pitch (deg)	chord (m)
profile 1	0.046	29.567	0.019
profile 2	0.052	29.567	0.019
profile 3	0.054	29.567	0.019
profile 4	0.069	25.627	0.053
profile 5	0.084	22.149	0.086
profile 6	0.099	19.303	0.083
profile 7	0.114	16.973	0.079
profile 8	0.130	15.053	0.074
profile 9	0.145	13.457	0.071
profile 10	0.160	12.116	0.067
profile 11	0.175	10.981	0.064
profile 12	0.175	10.011	0.061
profile 13	0.175	9.176	0.058
profile 14	0.175	8.451	0.055
profile 15	0.175	7.819	0.053
profile 16	0.176	7.263	0.051
profile 17	0.176	6.773	0.049
profile 18	0.177	6.338	0.047
profile 19	0.178	5.951	0.046
profile 20	0.176	5.605	0.044
profile 21	0.327	5.294	0.044
profile 22	0.340	5.014	0.042
profile 23	0.350	4.874	0.022

3.3.3 Modifications in rotorDiskSource

We have made some modifications in the main code of rotorDiskSourceTemplates.C because the original one does not determine the axial and tangential efforts, also the power

coefficient on each element of the blades, leading to greatly under-predicted rotor torque and downstream swirl velocities. The three main modifications that are made in the code involve:

1. Fixing an error in how the local forces are calculated ;
2. Implementing a more general blade tip correction ;
3. Implementing propeller performance parameters ;

The error is due to the fact that the original code used the blade drag as the tangential force and the blade lift as the axial force, which is only strictly true for rotors with a flow angle of zero, which is unrealistic for a generalized rotor. Instead, the lift and drag forces should be projected onto the rotor axial and tangential directions given the flow angle.

3.4 Validation

In this section, we focus on the behavior of a single hydrokinetic turbine, in terms of performance, that is to say of drag and power coefficients, as well as in terms of wake evolution. Particular attention is also made to the validation of the model with the experimental results of Mycek et al. (2014).

3.4.1 Experimental Setup

The experiments were performed in the IFREMER experimental flume tank (fig. 3.6), with a length of $L = 18m$, a width of $l = 4m$ and a depth of $h = 2m$. The rotor of diameter $d = 0.7m$ is connected to a cylindrical hub of diameter $d_h = 0.092m$ (Mycek et al., 2014). The blade collective pitch angle was preset at 0 degrees during the experiment. The rotor is connected to a motor-gearbox assembly consisting of a gearbox, a DC motor, a ballast load and a motor speed control unit, providing an active rotor speed control. The turbine blades are designed from a $NACA63418$ profile. A more detailed profile description is given in tables 3.3 and 3.4.

Fig. 3.6: Photograph of the IFREMER tunnel and honeycomb for adjusting the turbulence intensity rate (Maganga, 2011).

Table 3.3: Detailed blade profile description.

r/R	c/R	Pitch (deg)	t/c %
0.133	0.056	29.567	80.0
0.150	0.056	29.567	100.0
0.155	0.056	29.567	100.0
0.193	0.152	25.627	36.0
0.241	0.247	22.149	21.30
0.285	0.237	19.303	21.40
0.328	0.225	16.973	21.70
0.371	0.214	15.053	22.0
0.415	0.202	13.457	22.20
0.458	0.192	12.116	22.40
0.501	0.182	10.981	22.50
0.545	0.174	10.011	22.50
0.588	0.166	9.176	22.40
0.631	0.159	8.451	22.20
0.675	0.152	7.819	21.90
0.718	0.147	7.263	21.50
0.761	0.141	6.773	20.90
0.805	0.137	6.338	20.20
0.848	0.132	5.951	19.50
0.891	0.128	5.605	18.60
0.935	0.124	5.294	18.0
0.978	0.121	5.014	18.0
1.0	0.065	4.874	25.0

Table 3.4: Detailed blade profile description, $angle\ of\ attack\ (deg)$, c_d, c_l

angle of attack (deg)	cd	cl
-16.0	0.102	-0.651
-15.750	0.090	-0.698
-15.50	0.080	-0.738
-15.250	0.072	-0.775
-15.0	0.066	-0.804
-14.750	0.061	-0.828
-14.50	0.057	-0.847
-14.250	0.053	-0.862
-14.0	0.050	-0.873
-13.750	0.047	-0.883
-13.50	0.044	-0.888
-13.250	0.042	-0.895
-13.0	0.040	-0.90
-12.750	0.038	-0.879
-12.50	0.037	-0.869
-12.250	0.036	-0.862
-12.0	0.035	-0.862
-11.750	0.035	-0.890
-11.50	0.033	-0.858
-11.250	0.031	-0.820
-11.0	0.030	-0.782
-10.750	0.029	-0.748
-10.50	0.027	-0.709
-10.250	0.026	-0.674
-10.0	0.025	-0.639
-09.750	0.024	-0.608
-09.50	0.023	-0.576
-09.250	0.022	-0.558
-09.0	0.025	-0.543
-08.750	0.020	-0.535
-08.50	0.020	-0.523
-08.250	0.019	-0.513
-08.0	0.018	-0.501
-07.750	0.017	-0.488
-07.50	0.016	-0.475
-07.250	0.015	-0.463
-07.0	0.014	-0.447
-06.750	0.014	-0.426

The experimental setup is illustrated in fig. 3.7. The upstream turbulence intensity rate TI_∞ is defined in equation 1.1. The power coefficient C_P is defined as the proportion of power retrieved by the turbine as compared to the maximum available power from the incoming flow through the rotor area S:

$$C_P = \frac{M_x \omega_x}{\frac{1}{2}\rho\pi R^2 U_\infty^3} \tag{3.28}$$

where R is the radius of the rotor, πR^2 is the turbine cross-section area and M_x is the axial moment or torque. Also, the thrust coefficient C_T is defined as the axial force F_x acting on the turbine as compared to the kinetic energy of the incoming flow through the area:

$$C_T = \frac{F_x}{\frac{1}{2}\rho\pi R^2 U_\infty^2} \tag{3.29}$$

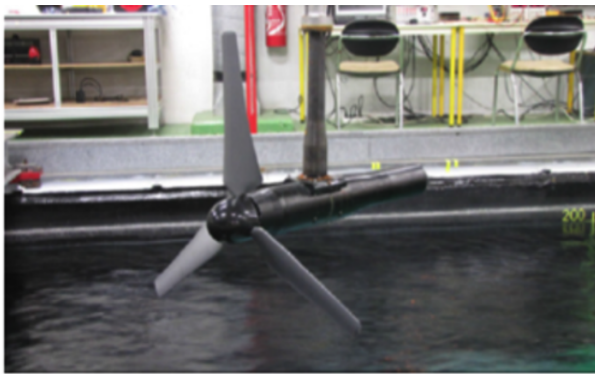

Fig. 3.7: Experimental turbine used in the IFREMER experiments (Mycek et al., 2014).

3.4.2 Numerical Setup

As mentioned above, the turbine is represented numerically by a porous disc, and a solid one is fixed on the center to represent the hub, on which the theory BEMT is applied and the momentum energy is extracted from the domain. The computational domain is a $4m * 18m * 2m$ block (fig. 3.8). The geometry and the mesh are created using ICEM CFD software, so the entire domain is meshed by $1.3million$ structured hexahedral cells (fig. 3.9). The disc of diameter d = 0.7 m is located at $11d$ downstream the inlet, this leaves $14d$ downstream the disc to observe the development of the wake. The mesh of areas of interest is refined to concentrate accuracy. The averaged value of the incident flow velocity 0.8 m/s is considered (table 3.5).

Table 3.5: Description of parameters used in Mycek et al. (2014) experiment; U_∞: flow velocity, TSR: Tip Speed Ratio (ω d/2U_∞), TI: Turbulence Intensity.

Profile	U_∞	**TSR**	**Re**	**TI**	**Pitch angle**	**Rotation**
NACA 63418	0.8 m/s	3.67	28 e4	3%	0°	counterclockwise

The blades are modeled using 23 discrete elements along their span in accordance with the detailed blade profile description in Mycek et al. (2014).

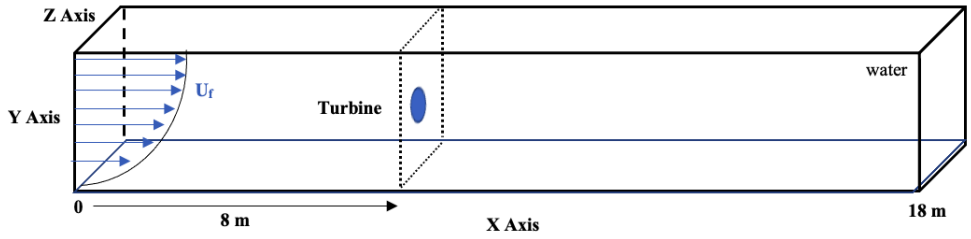

Fig. 3.8: Initial state and position of the disc in the channel.

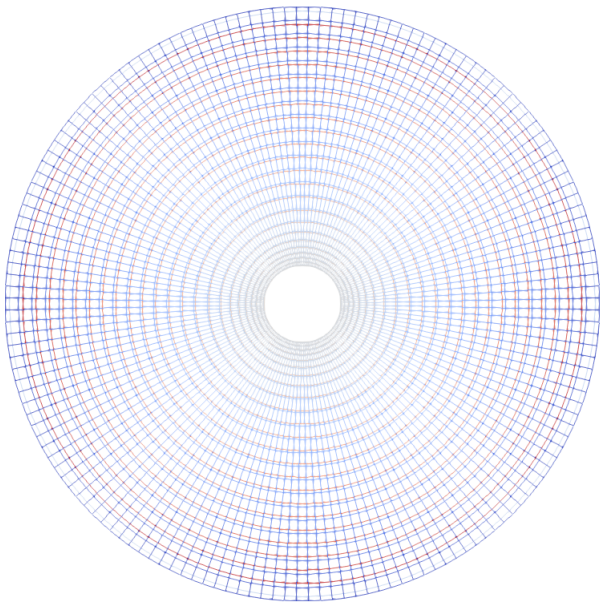

Fig. 3.9: Mesh configuration of the disc using structured hexahedral cells.

Concerning the boundary conditions themselves, at the walls, zero velocity is imposed. In inlet, the velocity is set to the logarithmic profile using the atmBoundaryLayer library in OpenFoam (eq. (5.2)) with the distance to the wall z, where u_* is the bed friction velocity function of U_{ref} = 0.77 m/s, κ = 0.41 is the von Karman constant, and z_0 =

$4.9e^{-8}$ is the Nikuradse roughness length. This profile is set also as initial condition. In outlet, the hydrostatic pressure is fixed. At the top, a slip condition is imposed.

$$\frac{u^f}{u_*} = \frac{1}{\kappa} ln(\frac{z + z_0}{z_0}) \tag{3.30}$$

3.4.3 Validation result

Coefficients of performance

Figure 3.10 shows the comparison of numerical results of the configuration above with the experimental measurements of Mycek et al. (2014). As observed, the C_p and C_T evolution is in accordance with the experiment as the TSR increases until 3.67. Otherwise, beyond this value, the difference between experimental and numerical results increased. That could be explained by the effect of the vortexes generated on the tip of blades, since it was considered from the beginning to be a simple correction on the tip, while in literature (Branlard and Gaunaa, 2014) there exist other corrections for BEMT that might be considered. In spite of this, the absolute errors between the two results are approximately 0.3% for C_p.

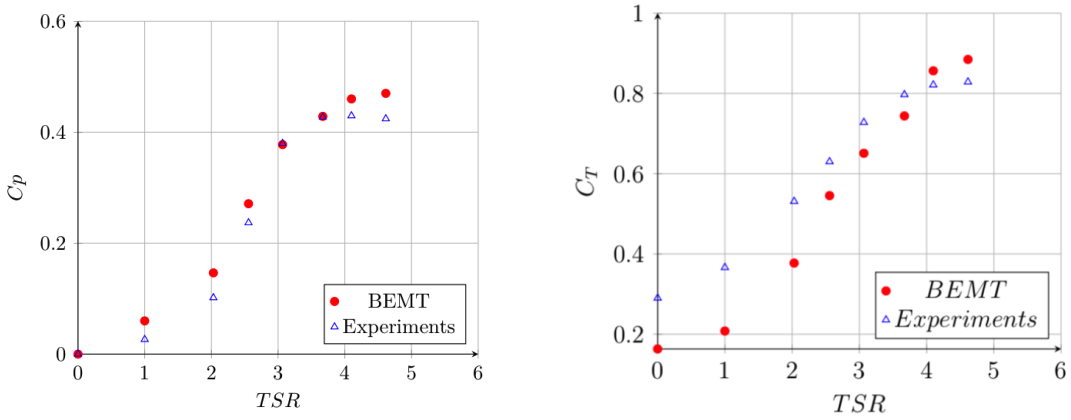

(a) **(b)**

Fig. 3.10: Variation of Power coefficient in function of TSR factor.

Wake characterization

Figures 3.11 show the variation of axial velocity u_x and the turbulence intensity I_{2d} in the wake between $1.2d$ and $10d$ behind the turbine. The considered flow velocity is U_∞ = 0.8 m/s and the hydrokinetic turbine speed corresponds to a TSR of 3.67. This value corresponds to a speed of rotation of 80 round per minute, or approximately 8.38 rad/s. As before, the ambient turbulence rate is I_∞ = 0.03.

The first to be noted, is that the degradation of the axial velocity is clear even until $10d$ downstream the turbine. It is shown how the turbine creates a zone of a velocity deficit

along the axis of the channel, by capturing the hydrodynamic energy of the water and transforming it to a kinetic energy.

Figure 3.12 and 3.13 show the vertical profiles of the axial velocity and the turbulence intensity I_{2d} downstream the turbine respectively. In general, the BEMT results curve and the measurements curve have the same trend of evolution near the turbine until $10d$ downstream its location. This is in accordance with the theory, so that the BEMT is reliable in determining the local effect of the turbine and calculating the local efforts on its blades. Whereas near the turbine, at $1.2d$ and $2d$, the form of the BEMT profile is not similar to the measurements at the level of the turbine, because this last is modelled by a porous disc without taking in consideration the hub geometry and the support of the turbine, this might have an impact on the distribution of the velocity deficit just behind the turbine.

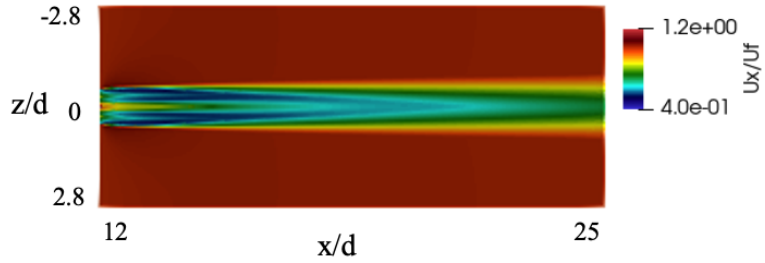

(a)

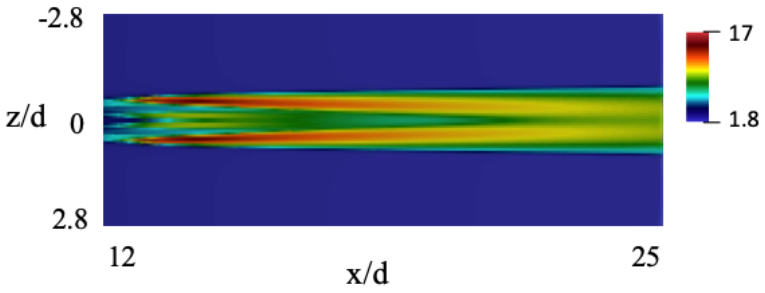

(b)

Fig. 3.11: Map of the (up): dimensionless axial velocity downstream the turbine in the wake and of the (down): axial turbulence intensity I_{2d} downstream the turbine in the wake for $TSR = 3.67$.

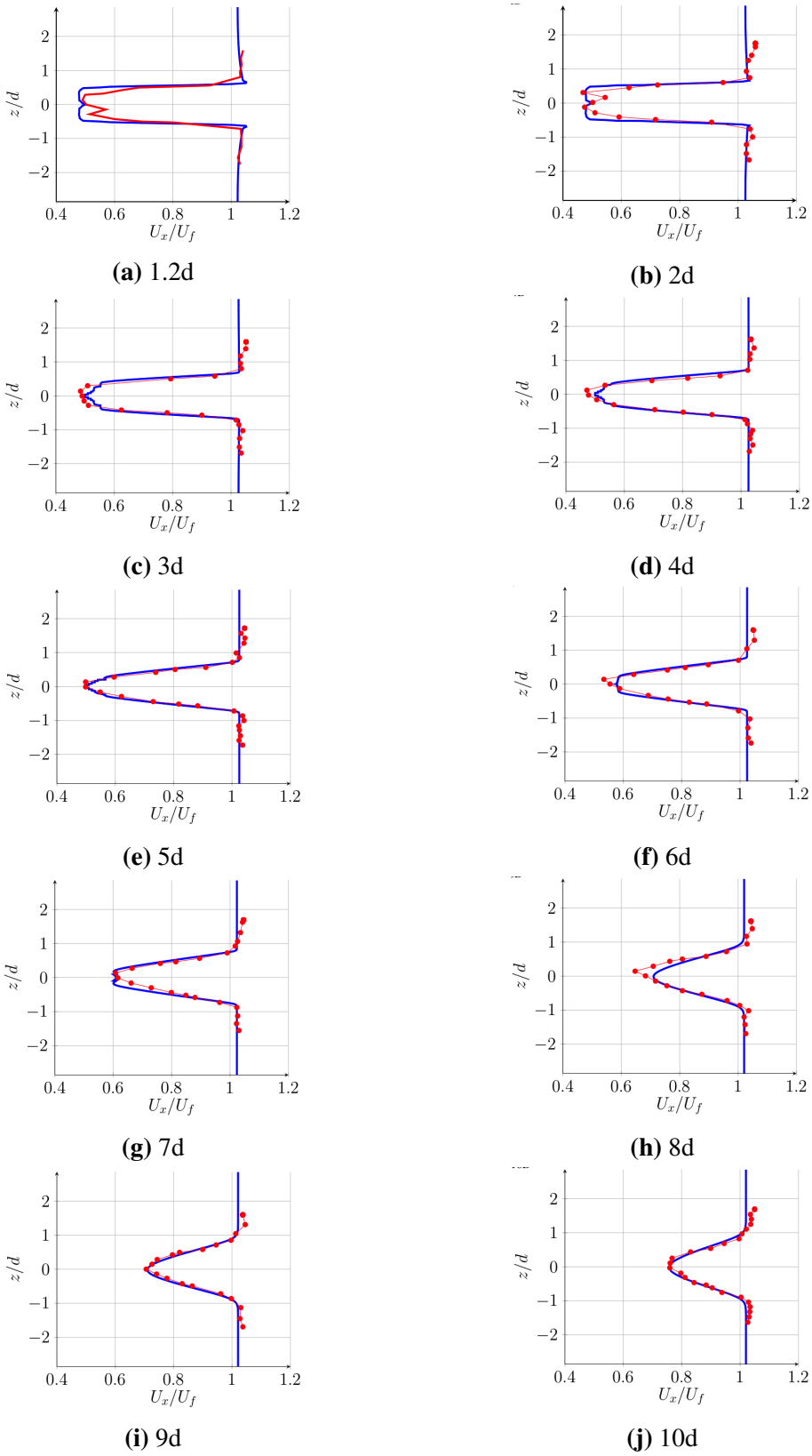

(a) 1.2d **(b)** 2d

(c) 3d **(d)** 4d

(e) 5d **(f)** 6d

(g) 7d **(h)** 8d

(i) 9d **(j)** 10d

Fig. 3.12: Vertical profiles of the axial velocity dimensionless by the fluid velocity (U_x/U_∞), downstream the turbine; blue for numerical BEMT results and red for the measurements of Mycek et al. (2014).

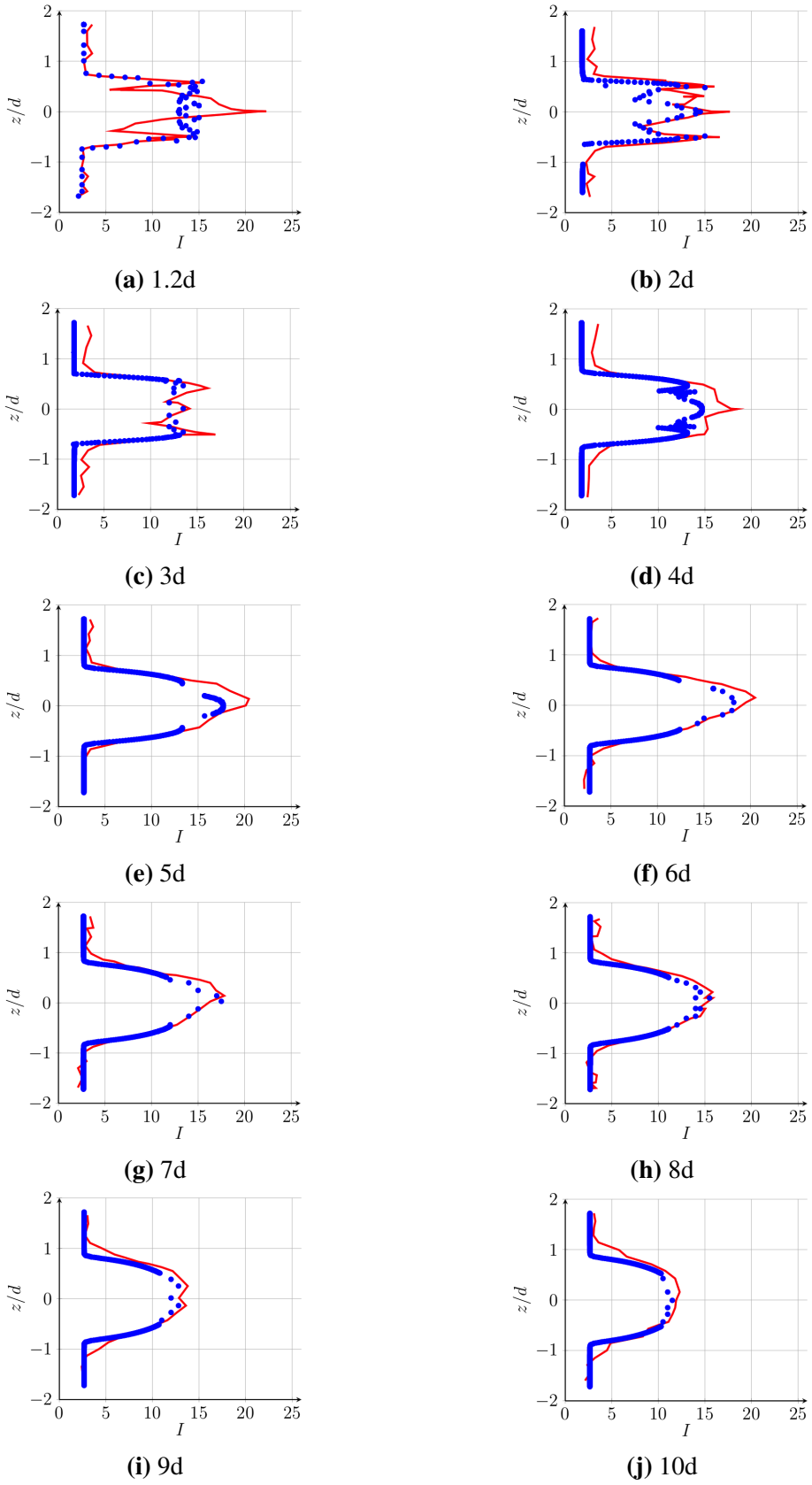

(a) 1.2d **(b)** 2d

(c) 3d **(d)** 4d

(e) 5d **(f)** 6d

(g) 7d **(h)** 8d

(i) 9d **(j)** 10d

Fig. 3.13: Vertical profiles of the mean turbulence intensity I_2d, downstream the turbine; blue for numerical BEMT results and red for the measurements of Mycek et al. (2014).

3.5 Coupling BEMT with two-phase model

Once the two phase Eulerian-Eulerian model is validated for the sediment transport, and the hydrodynamic model BEMT presented his capabilities to reproduce the near wake behind a turbine and the power coefficients of the turbine under specific conditions, it is time to couple these two models to investigate the impact of the turbine on the sediment transport all in one configuration.

The coupling lies on integrating the term source, added to the Navier-Stockes equations (eq. 2.3 and 2.4) and representing the hydrodynamic forces applied by the turbine on the flow, into SedFoam in the form of specific libraries in OpenFOAM, such as fvOptions libraries.

3.6 Summary

A numerical method, based on the Blade Element Momentum and the Actuator Disk theories, made possible the modeling of the hydrodynamic efforts induced on the flow by the hydrokinetic turbine represented by a porous disc. The different aspects of the method have been described in the first part of this chapter. In the second part, the numerical implementation of the model into the OpenFOAM built-in rotorDiskSource class is then described within the rotoDisk library that represents the source term added to the Navier-Stockes equations 2.3 and 2.4. It is also shown some of the modifications realized on this class since it has a critical bug which results in greatly under-predicted rotor torque and downstream swirl velocities. Then, the numerical simulations carried out with the calculation code resulting from this method were exposed when comparing to the measurements obtained by Mycek et al. (2014). It was shown that the performance evaluation in terms of power and drag coefficients was in good agreement with the experimental results in the ascending part of the curves. However, for higher rotational speeds, the separation of the boundary layer, which causes the reduction in torque and therefore in C_P, cannot be taken into account with the current turbine representation model. Since the blades are modeled by infinitely thin profiles, only the value of the pressure jump across the surface is likely to be evaluated and not the pressure itself. The model failed to capture the effect of vortex shedding from the blade tip. Nonetheless, this shortcoming is to be expected from the current model, as only time-averaged momentum sources are being introduced on the rotor disk. In the range of validity of TSR, a convergence study was successfully carried out and the values obtained are close to the numerical and experimental results of Mycek et al. (2014). Concerning the wake behind the turbine, it was characterized using axial velocity snapshots, profiles at different distances downstream of the turbine.

The numerical results obtained are in good agreement with the experimental results for an ambient turbulence intensity equals to 3%. Taking into account a different value of the ambient turbulence rate in the flow, such as 15% is one of the perspectives in the future work.

Chapter 4

Local scour near an axial-flow turbine

4.1 Introduction

Assessment of turbine interaction with the local sediment environment has been identified as a key environmental issue needing investigation for turbine's device design and development. In particular for erodible channel environments, the interaction between a turbine and the evolution of the bed topography must be monitored in order to avoid both the structural failure of the device support structure and the propagation of scour or deposition features within the channel. Hydrokinetic turbines interact with the dynamics of the sedimentary bottom at small and large scale. Despite the interest that the study of these interactions deserves, little research has been published in the field.

In this chapter, we are interested on the large scale experiments under clear water conditions carried out by Hill et al. (2015) at the Saint Anthony Falls Laboratory, University of Minnesota. We study the effect of the modeled turbine on the near bed evolution by using the Euler-Euler two-phase flow model presented in Khaled et al. (2021). Two kind of turbine modelings are considered: the actuator disk theories (AD) (Nguyen et al., 2016), and the Blade Element Momentum Theory (BEMT) to parameterize the turbine blades. The experimental and numerical implementations are first described. Then, we apply the two methods (EE with AD and EE with BEMT) to simulate the interaction between an axial-flow hydrokinetic turbine with two different tip-speed ratios and an erodible bed under clear-water conditions and compare the computed results in terms of bed morphology with measurements by Hill et al. (2015). We also investigate how the different models of turbine (AD or BEMT) and different tip speed ratios, can affect the computed results in terms of wake characteristics and velocity profiles. Finally, conclusions are presented.

4.2 Experimental setup

The experiments were conducted in a channel of 2.75 m wide, 1.8 m deep and 85 m long. A bed of uniform sediment material (sands, d_s = 1.8 mm) is distributed and flattened over all the channel bottom. A three bladed axial flow turbine is installed $4d$ downstream from the beginning of the channel, the rotor diameter is d = 0.5 m. The base of the turbine is conical and covered by the sediment layer about 0.15 m from the bottom of the channel. Figure 4.1 shows a photo of the test section, turbine and instrumentation used during experiments.

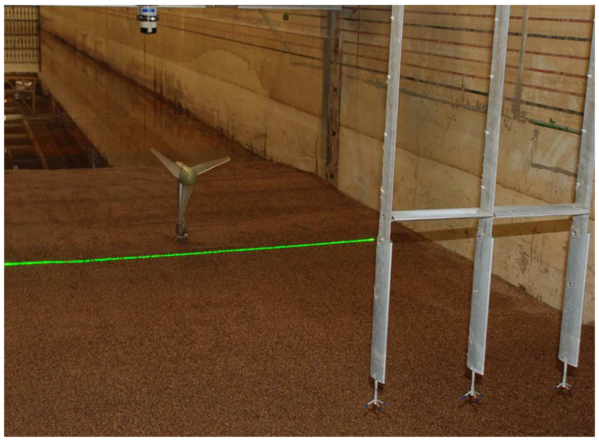

Fig. 4.1: Photo of the model and the instrumentation used in the experiments of Hill et al. (2015).

Net erosion and deposition was mapped by differencing before and after topographic scans. Test section mean inflow velocities were characterized using a Sontek PC-ADP located approximately $2d$ upstream of the turbine location. Test section outlet flow velocities were monitored using three synchronized Nortek Vectrino velocimeters located 6dT downstream of the turbine at hub height. Average flow rate during all large-scale test cases was kept constant at $Q_w = 1.765\ m^3/s$.

Further information about the experimental setup is found in Hill et al. (2015).

4.3 Numerical setup

The simulated channel (fig. 4.2) is 10 m long (streamwise direction x), 2.75 m wide (crosswise direction z) and 1.15 m deep (vertical direction y).

Concerning the turbine's modeling, as explained in chapter 3, the turbine extract kinetic energy from the flow as it produces electricity through generators. The basic principle of AD and BEMT is to recreate the effects that a real turbine would have on the surrounding current by adding a sink term corresponding to the average hydrodynamic

force. These force fields are applied in the form of source terms. The balance between the force field and the modified flow is then governed by the conservation equations of mass and momentum (2.3) and (2.4). So the rotor is represented by a porous disk of diameter d = 0.5 m. The center of the rotor is located at 3 m from the inlet with a height of 0.425 m from the bed surface. The bulk velocity of the fluid is 0.56 m/s. Two configurations are considered: A* and B*. The tip speed ratio is 7.1 for A* and 5.8 for B*. We investigate the dependence of bed patterns first on the model that represents the turbine (AD and BEMT) with TSR = 7.1 (configuration A*), then on two different tip speed ratios of the rotor (TSR = 5.8 (B*) and TSR = 7.1 (A*)), in which TSR = 7.1 is the one employed in the experiment. Tables 4.1, 4.2, 4.3 and 4.4 show other hydrodynamic and sediment properties used in this section.

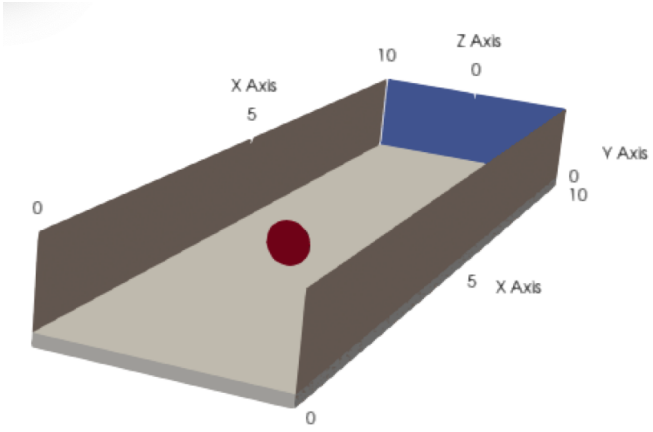

Fig. 4.2: Initial state of the domain, position of the disc at $3m$ from the inlet and the sheet layer of sands on the bottom (grey color).

Table 4.1: Numerical hydrodynamic properties for the configurations $A*$ and $B*$ where a, b, c are the dimensions of the channel, a is the domain length in the x-direction, b is the water depth and c is the length in y-direction. x' is the position of the turbine, TI is the turbulent intensity.

a*b*c	d	x'	TI	U_∞
$10 * 1.15 * 2.75$ m	0.5 m	3 m	3%	0.56 m/s

Table 4.2: Numerical properties for the configurations $A*$ and $B*$ where s is the initial thickness of sand sheet and d_s is the mean sand diameter. Note that u_* is the bed friction velocity lower than the critical value to avoid the flow effect on the sediment transport.

ϕ	s	d_s	u_*	u_{*cr}
55%	0.15 m	1.8 mm	0.027 m/s	0.034 m/s

Table 4.3: Tip-Speed-Ratio values of the configurations $A*$ and $B*$.

	A*	**B***
$turbine's\ model$	$AD-BEMT$	AD
TSR	7.1	5.8

Table 4.4: Different models of sediment transport used in the simulations for configurations $A*$ and $B*$.

particle shear stress	friction model	viscosity model	drag model	particle pressure model
granular flow	$\mu(I)$ (Chauchat and Médale, 2014)	Boyer et al. (Hsu et al., 2003)	Gidaspow (Hsu et al., 2003)	Lun (Lun, 1991)

The bottom is considered as a wall where a zero velocity, and a Neumann boundary condition for TKE are imposed. The inlet velocity is set to the logarithmic profile with the distance to the wall y, where u_* = 0.027 m/s is the bed friction velocity. This value is chosen so that it is lower than the critical velocity (u_* = 0.034 m/s) to avoid the sediment transport due by the flow. In outlet, the hydrostatic pressure is fixed. At the top, a slip condition is imposed.

Concerning the sediments properties, a bed of 55% of sands of diameter of 1.8 mm and density of $1922\ kg/m^3$ is layed down under the turbine all along the canal. The turbine is modelled using the Blade Element Momentum Theory or the Actuator Disk model, the effect of the tower is not considered here. The time step is 0.001 s. The critical stress τ_c calculations used for comparison are based on the work of Shields (1936). Considering the chosen sediment, the critical Shields parameter is θ_{cr} = 0.0696. This corresponds to a critical shear stress value of 1.156 Pa.

4.4 Effects of different turbine's modeling on bed pattern

In this section, we examine how the scour evolution and scour pattern depend on the model that represents the turbine blades.

The initial flat topographic surface has been subtracted from the final bed topography and normalized by the turbine rotor diameter, enabling visualization of regions where erosion (negative values) and deposition (positive values) have occurred.

4.4.1 Temporal Evolution of the local scour

Figures 4.3 and 4.4 show the computed contours of bed elevation at t = 0 min, t = 2 min and t = 3 min, the turbine is located at x = 3 m. As seen, the scour is occurred below the turbine and a deposition area is appearing in the downstream. During baseline condition, no sediment transport occurred, confirming that the local shear stress, τ_b, is below the critical (Shields) value for the given grain size, τ_{cr} = 1.15 Pa.

It is noticed that the form of the scour is almost circular under the turbine in the case of BEM theory (fig. 4.3), which is not obviously the case when using the AD turbine model (fig. 4.4). One notices that the deposition pattern downstream the turbine is more important in the BEMT case than in AD one. This is indicative of the differences in sediment dynamics between the two approaches. The turbine modelled by BEMT induces more local impacts due to the tip vortices and the 3D effects of the turbine rotation on the bed. The computed temporal scour evolution is compared with the measurements of (Hill et al., 2015) and the numerical results of (Yang et al., 2017) in fig. 4.5 at four spanwise locations (z = 0, z = $0.2d$, z = $0.4d$ and z = $0.6d$) $0.1d$ downstream of the turbine. The computed bed evolutions are close and show good agreement with the measurements and the LES results in the near wake (fig. 4.5a and fig. 4.5c). It appears some differences in the depth of the scour at z = $0.4d$ and z = $0.6d$ that can be attributed to the comparison on the first minutes of the phenomenon. Indeed, the results of Yang et al. (2017) are a bit far from the measurements in the first instants but they are nearly the same as the simulation takes place (Yang et al., 2017). Anyway, the BEMT results are closer to measurements than those of AD.

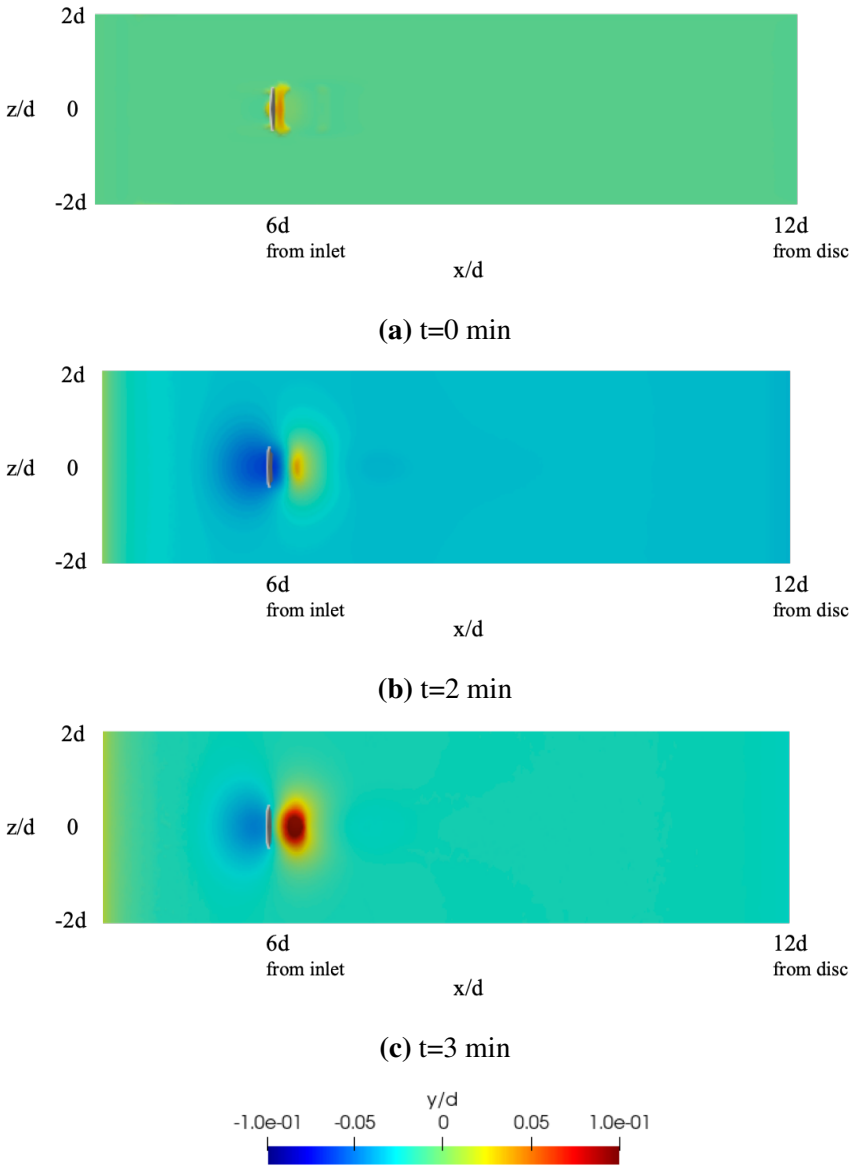

(a) t=0 min

(b) t=2 min

(c) t=3 min

Fig. 4.3: Computed contours of bed elevations relative to the initial flat bed at different time instants for Blade Element Momentum Theory.

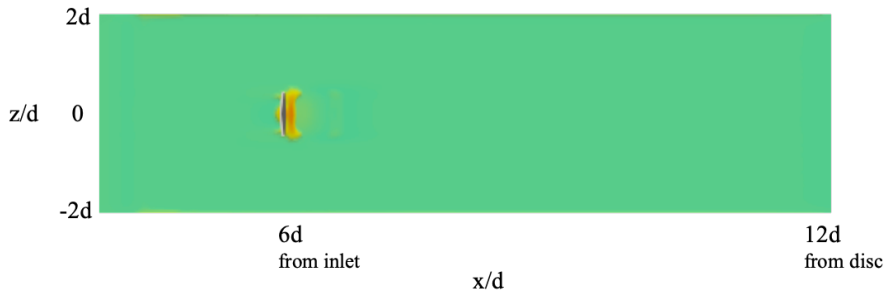

(a) t=0 min

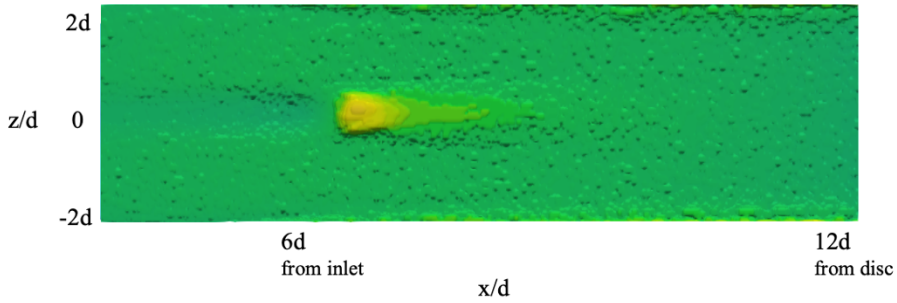

(b) t=2 min

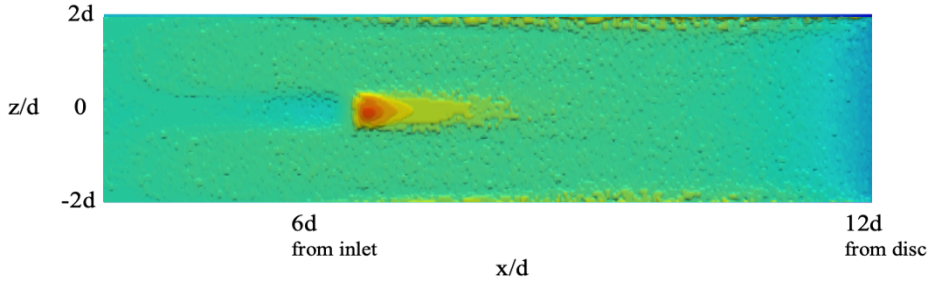

(c) t=3 min

Fig. 4.4: Computed contours of bed elevations relative to the initial flat bed at different time instants for Actuator disk theory.

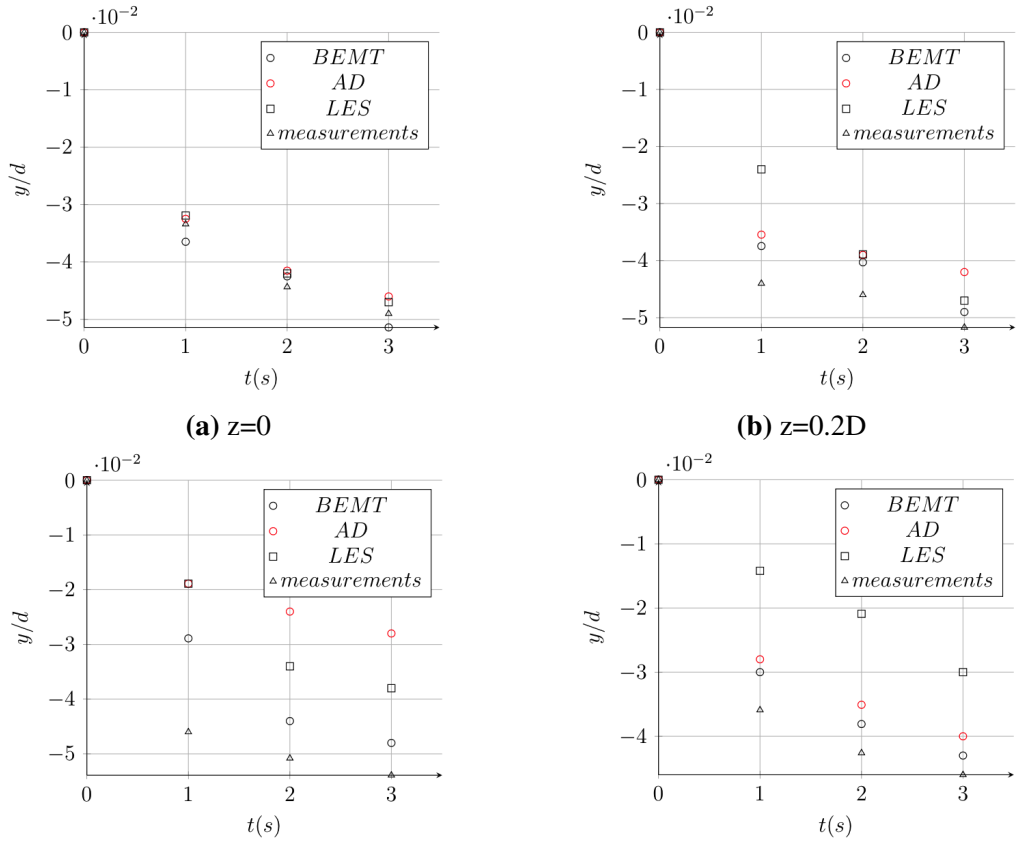

(a) z=0 **(b)** z=0.2D

(c) z=0.4D **(d)** z=0.6D

Fig. 4.5: Comparison of computed time series of bed elevation relative to the initial flat bed at $0.1d$ downstream from the rotor and at (a) $z = 0$, (b) $z = 0.2d$, (c) $z = 0.4d$ and (d) $z = 0.6d$ (turbine is located at $z = 0$ in the spanwise direction): measurements by Hill et al. (2015) (triangle); multiphase Euler-Euler with BEMT (black circle); multiphase Euler-Euler with AD (red circle); LES by Yang et al. (2017) (square).

4.4.2 Morphodynamic impact of the turbine

Figure 4.6 shows the spatial evolution of the bed elevation and the lateral shear stress τ_{yz} in the cross-sections (under the turbine and $1d$ from the turbine location). Figure 4.6a shows that the maximum scour occurred below the turbine is $0.052d$ for $BEMT$ but $0.046d$ for AD, this is already shown in fig. 4.3. The V-shape of the scour is wider in BEMT than in AD simulation. This illustrates also the local effects of the swirl induced by the tangential force.

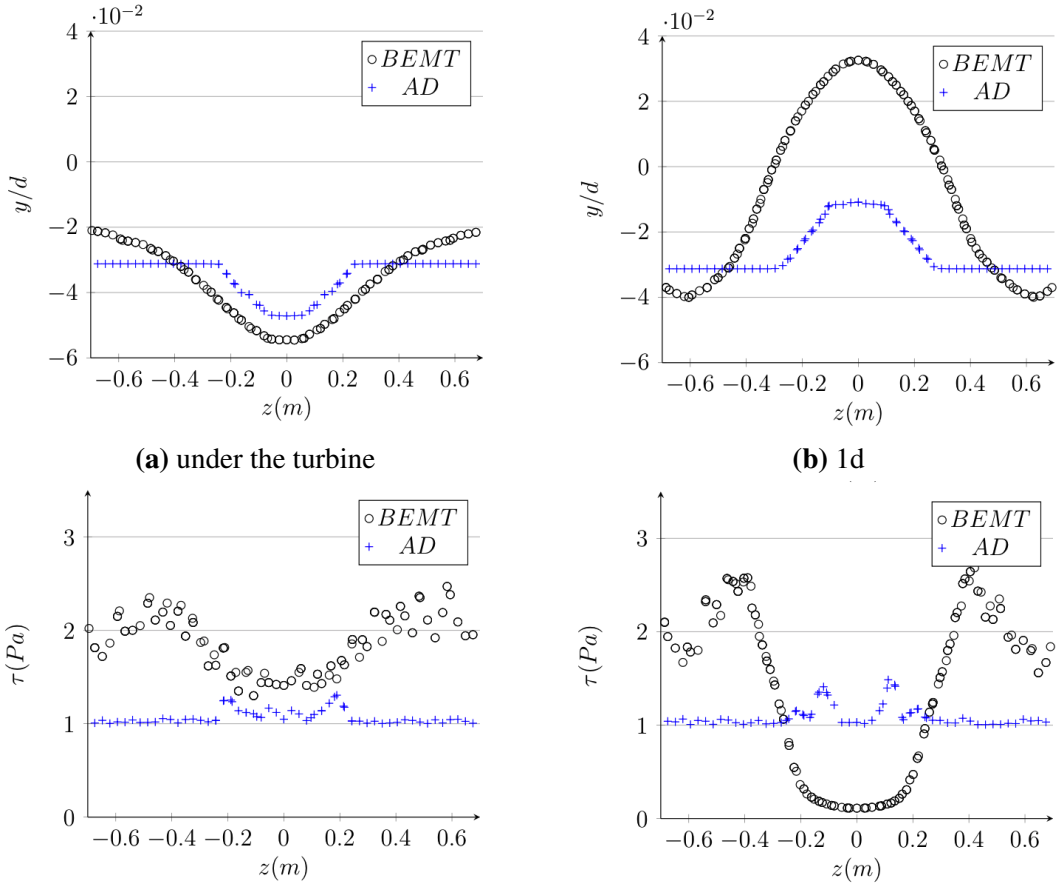

(a) under the turbine

(b) 1d

(c) under the turbine

(d) 1d

Fig. 4.6: Comparison of computed cross-sections contours of bed elevations y/d (a,b) and shear stress τ_{yz}, between $BEMT$ and AD theories at t = 3 min.

Figure 4.6b, shows that a phenomenon of deposition is occurred downstream of the turbine in BEMT since the bed elevation is greater than the initial flat bed $y/d = 0$. This is a result of an important erosion process occurring under and close to the turbine that leads to deposit the sediments at $1D$ and reach such bed elevation. This erosion may be produced by the longitudinal shear stress but also by the fluctuating variation of the lateral local shear stress (fig. 4.6c). The values of this last are much greater than the critical bed shear stress as mentioned previously. So that the eroded sediments hit the edges of the channel and they are transported by the current and trapped in the wake to be deposit at $1d$. Thus, the erosion is more important in BEMT than in AD and seems to be more realistic too.

4.4.2.1 Effects of different turbine models on turbine's wake

Differences are appearing on the flow between the two simulations with BEMT and AD. The streamwise velocity is affected much close to the location of the turbine (fig.

4.7) for which the AD affects more the axial velocity than the BEMT. In both models, the wake is recovered progressively downstream the turbine. At $1d$ downstream the turbine, the vertical profiles of the streamwise velocity of BEMT and AD (fig. 4.8) are not as much near as in the far wake. Close to the turbine and until $3d$ after it, the z-component of the velocity differs indicating the presence of the tangential velocity in the BEMT simulation. This is the manifestation of the turbine rotation modeled by the tangential force. After $3d$, the tangential velocities are close for both simulation indicating a dissipation of swirl induced by the disc rotation.

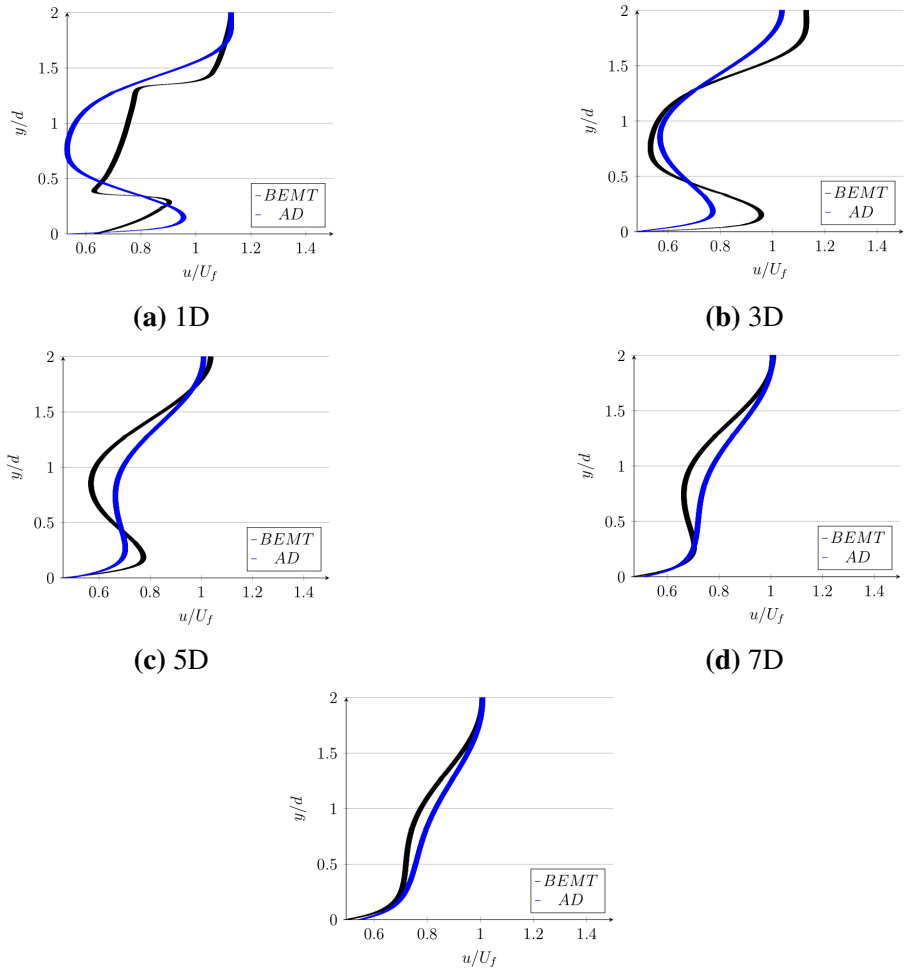

(a) 1D **(b)** 3D

(c) 5D **(d)** 7D

(e) 9D

Fig. 4.7: Comparison of computed vertical profiles of axial velocity between AD and BEMT at $1d, 3d, 5d, 7d$ and $9d$ turbine downstream locations.

The turbine represented by an actuator BEM model induces a thrust force and a tangential force, these produce a reduction of the axial velocity in the turbine's wake and an increase of the tangential velocity which produces a swirl close to the turbine (fig. 4.7a). This effect is more visible in fig. 4.8, where the vertical profiles of the rotational

velocity shows the impact of the turbine in the vertical axis across the turbine and in the wake.

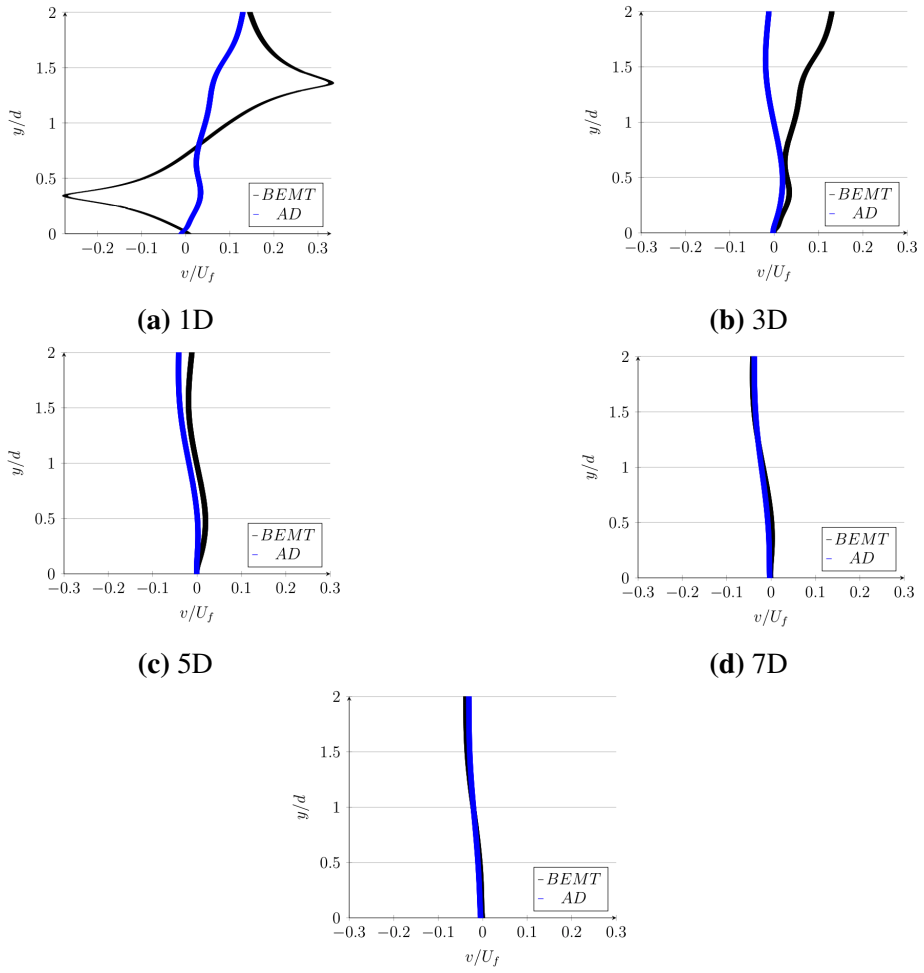

(a) 1D **(b)** 3D

(c) 5D **(d)** 7D

(e) 9D

Fig. 4.8: Comparison of computed vertical profiles of transverse velocity between AD and BEMT at $1d, 3d, 5d, 7d$ and $9D$ turbine downstream locations.

Figure 4.9 shows that the wake for BEMT is recovered closer to the turbine than in the case of AD. But it is evident that it is not well established since the results are at the first instants of the simulations. This difference could be considered with care, as the complexity of the model needs maybe more time to converge where as the results are at the first instants of the simulations.

Though the impact of the tangential velocity on bed under the turbine is more important for BEMT compared to AD, the swirl produced by the turbine would have a very local impact.

It reveals also the presence of a high vorticity close to the bottom in the turbine's plane (fig. 4.10) that should produce an erosion beneath the turbine. This vorticity decreases

with the distance to the canal axis.

This explains the localisation of the erosion close to the turbine. This could explain the scour occurred below the turbine of BEMT about $0.052d$ which is deeper than that of AD around $0.042d$ (fig. 4.6a).

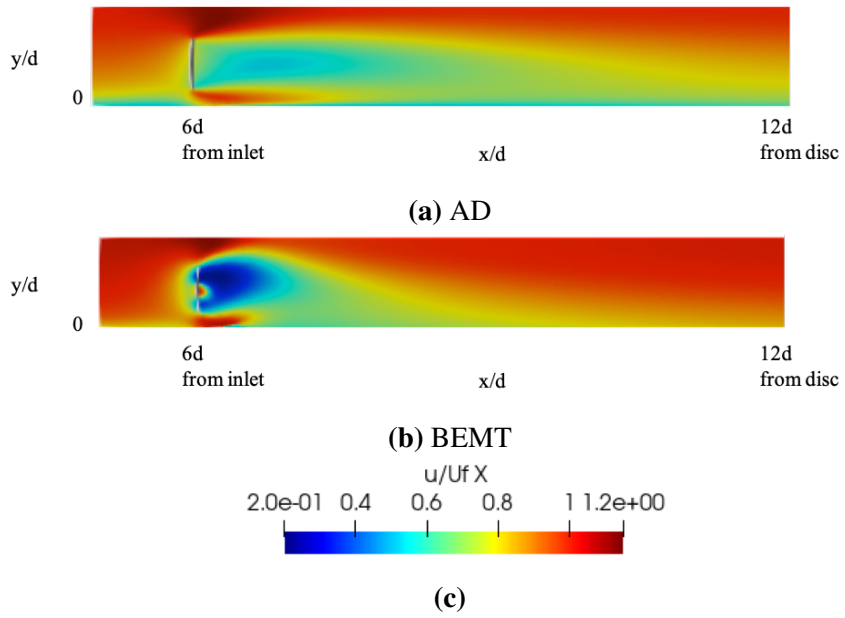

(a) AD

(b) BEMT

(c)

Fig. 4.9: Axial profiles of streamwise velocity for (a) Actuator Disk Theory and (b) Blade Element Momentum Theory at t = 3 min.

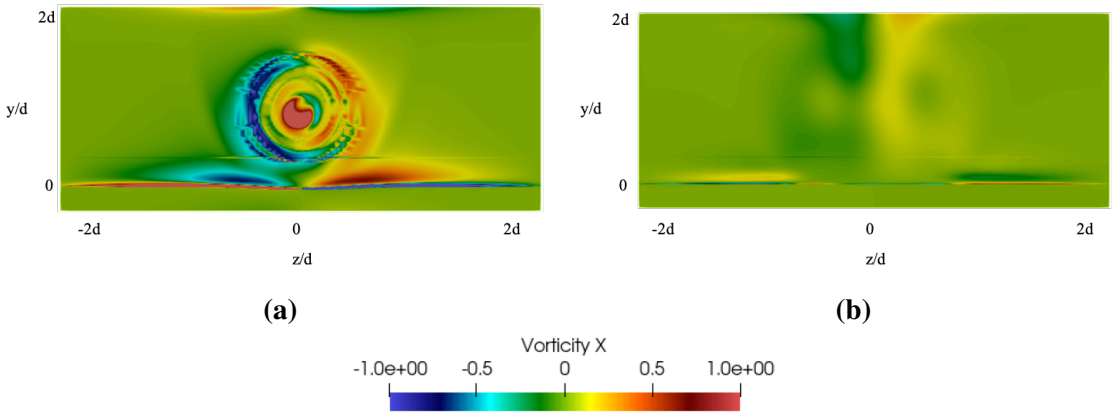

(a) **(b)**

Fig. 4.10: Velocity field in the (y,z) plans colored by the fluid vorticity at t = 3 min for BEMT (a) under the turbine and (b) $1d$ from the turbine location.

4.5 Summary

The investigation carried out in this chapter aims to couple the 3D Euler multi-phase model CFD approach to two actuator models (BEMT and AD) of an axial-flow three-bladed hydrokinetic turbine to study the interactions between the turbine and sediment transport of sandy bed under clear-water scour conditions. The energy extracted by the turbine alters the hydrodynamics of the stream by increasing or reducing the friction in areas around the turbine. Close to the turbine, scour phenomena and deposit zones are appearing. The results are compared with measurements and LES results in literature. Good agreement was obtained in the near wake. A deeper scour and deposition regions are observed for BEMT. On the other hand, the wake is more established for AD downstream the turbine in the first instants of the simulations.

The upcoming works concern the simulation for longer time to examine the evolution of the bottom with the different configurations, and will be conducted with the AD-BEMT model only.

Chapter 5

Blockage Effects on turbine-sediments interactions

Introduction

Once the coupled model validation was carried out, it is crucial to study the interaction between hydrokinetic turbine and sediment transport. This chapter presents the results obtained for the simulation of the blockage effects on the turbine's impact on the sediment transport. It consists in considering one sediment class, sand of one diameter, and an horizontal axis turbine with an axial flow direction corresponding to the riverine case. The approach is configured first with two different dimensions of the computational domain: configurations A and B. Then, a general conclusion is occured after studying the blockage effects of other four different configurations C, D, E and F.

The numerical integration of the configurations into OpenFOAM is shown first with an overview on the hydrodynamic and sediment properties used in simulations. Thus, a comparison of the turbine's impact on the bed topography is then investigated between the configurations, presenting the temporal evolution of the scouring under the turbine for all configurations. A particular interest is also given to the constraints on the bottom and the turbine's impact on the wake, which are crucial for the setting in motion of the sediments.

It has been shown for all configurations that the scouring capabilities are well enhanced below the turbine due to the acceleration of the flow and increasing of local shear stress of sediments.

Due to the very costly calculation times, the simulations focused on the first hundred seconds of the scour phenomenon, and these results provide proof of concept that the two-phase approach is able to deal with configurations where the interactions between the two phases and the structures are three-dimensional and complex.

The following chapter has been published in the Journal of International Sediment Research (Khaled et al., 2021).

5.1 Scour-Sensitivity to channel width configurations

Two different configurations are carried out in this section, for which the tip-speed-ratio $TSR = U/U_\infty = 2.1$ and the turbulence intensity $TI = 3\%$ are held constant. The flow Reynolds number is sufficiently high ($Re = 240000$) so as to maintain fully turbulent conditions. All the sediments and hydro properties are the same for configurations except the channel's widths thus the blockage ratios differ. The blockage ratio is defined as the ratio of the total turbine area to the channel cross-sectional area:

$$B_r = \frac{n_t A_T}{b * c} \tag{5.1}$$

where A_T is the turbine area, n_t is the number of turbines ($n_t = 1$ in this chapter), b and c are the dimensions of the channel.

Tables 5.1, 5.2 and 5.3 show the numerical properties and the different blockage ratios of the configurations. The sediment particles are made of medium sand, density $\rho_s = 2650$ kg/m^3 and diameter $d_s = 0.25$ mm. The fluid is water with density $\rho_f = 1000$ kg/m^3 and kinematic viscosity $\nu = 10^{-6} m^2/s$.

Table 5.1: Numerical properties for configurations A and B where $c/2$ is the distance between the center of the turbine and the lateral edge of the channel.

	A	**B**
$c/2$	$6d$	$2.5d$
blockage-ratio	1.67%	4.2%

Table 5.2: Numerical hydrodynamic properties for configurations A and B where x' is the position of the turbine from the inlet, d is the turbine's diameter, TI is the turbulent intensity, U_∞ is the mean upstream velocity of the fluid. Note that the Froude number is $Fr = 0.466$.

d (m)	x' (m)	TSR	TI	U_∞ (m/s)	turbulence model
0.08	1.51	2.1	3%	0.8	$k-\epsilon$

Table 5.3: Numerical sediment properties for configurations A and B where ϕ is the initial volume fraction of the sediments, s is the initial thickness of sand sheet and d_s is the mean sand diameter. Note that the Froude number is $Fr = 0.466$.

ϕ	s (m)	d_s (mm)	particle shear stress	friction model	viscosity model	drag model	particle pressure model
61%	0.05	0.25	granular flow	MuI (Hsu et al., 2003)	Boyer (Hsu et al., 2003)	Gidaspow (Hsu et al., 2003)	Lun (Lun, 1991)

5.1.1 Computational mesh

The computational domain of each configuration is a block of $a = 4$ m length along the x-axis and $b = 0.3$ m deep on y-axis (fig.5.1), the width c of the channel differs among the configurations (table 5.1). The disc of diameter $d = 0.08$ m that represents the energy extracted by the turbine, is placed at 1.51 m downstream the inlet (fig. 5.1). The mesh is created using the OpenFOAM library package, block Mesh, it is configured as 60 million hexahedral mesh for the wider channel (A), such as the size of the wider mesh is approximatively equal to $0.04d$. A layer of 0.05 m thickness and composed of 61% of sand is spread on the bottom. Since the mesh is heavy, the mean time of the calculus is about 72 hours to compile 100 s of the simulation.

5.1.2 Boundary conditions

Concerning the boundary conditions themselves, at the walls, zero velocity is imposed. The bottom boundary used a smooth wall no slip condition and employed wall functions for the near wall flow. This allowed boundary layers to develop naturally along the tunnel test section. Within the OpenFOAM framework, for the TKE, a small fixed value can be used so as the kqRWallFunction that acts similarly as a Neumann boundary condition. At the outlet, zero-gradient conditions (Neumann conditions), are specified for all quantities, except for the reduce pressure p for which a uniform Dirichlet condition is imposed. At the top surface of the computational domain, Neumann conditions are applied for k and ϵ and for the three components of the velocity. Consequently, it cannot handle situations where the free surface is deformed near the structure. At the side, symmetry planes conditions are used. In inlet, the velocity is set to the logarithmic profile (eq. (5.2)) with the distance to the wall y, where u_* is the bed friction velocity, $\kappa = 0.41$

is the von Karman constant, and k_s = $2.5d_s$ is the Nikuradse roughness length in order to account for the bed roughness. This profile is set also as initial condition. Concerning the value of u_*, it is chosen to be 0.0369 m/s greater than the critical value, u_*cr = 0.0342 m/s. This latter is determined regarding the critical Shields parameter of the chosen sediment θ_{cr} = 0.043 (Shields, 1936), this corresponds therefore to a critical shear stress value of 0.1738 Pa. In outlet, the hydrostatic pressure is fixed. At the top, a slip condition is imposed. The real bottom is considered as impermeable.

$$\frac{u^f}{u_*} = \frac{1}{\kappa} ln(\frac{30y}{k_s}) \tag{5.2}$$

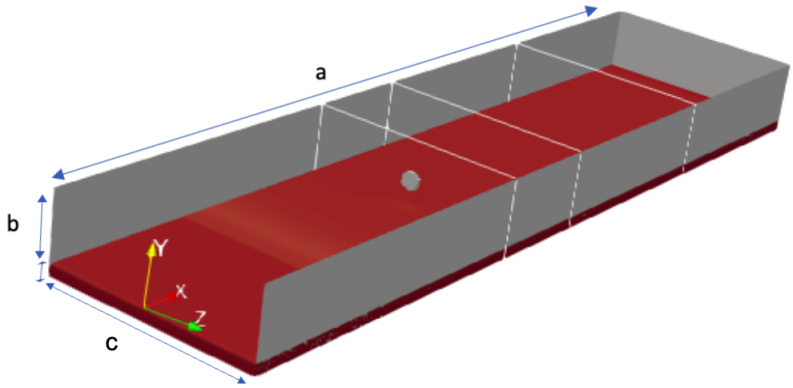

Fig. 5.1: Initial state of domain, position of the disc and the sheet layer of sands on the bottom (red color) and the three cross-sections (dashed-white lines) used for the configurations, a, b and c are the length, depth and width of the hydrodynamic channel respectively.

Concerning the turbine, the blades are modelled using 23 discrete NACA 63418 elements among their span in accordance with the blade profile given in Mycek et al. (2014).

The fluid turbulence model $k - \epsilon$ has been used for both configurations. A time step of 10^{-3} s is imposed to approach the convergence.

5.2 Results

To illustrate the turbine's impact on the sediment transport, the results of the two configurations A and B are considered and compared to the baseline results. Then an attempt is made to study the effect of the blockage ratios on the interaction turbine-sediment by comparing the results of the two configurations A and B.

5.2.1 Impact of the turbine on the bottom topography with comparison to baseline conditions

The configurations A and B are carried out in this section. A particular study of the impact of the turbine on the sediment transport and the generated wake, is investigated with comparison to baseline conditions.

Figure 5.2 and 5.3 show the modifications of the sediment bed due to the presence of the turbine for configurations A and B. Several changes in bed morphology have been found in the presence of the turbine. The clearest feature is the scour in the near wake area below the turbine, and the formation of sedimentary body downstream the turbine. In addition, changes on the bed are carried out in the far wake in configuration A comparing to baseline morphology. The impact of the turbine on the transport of sediments is clear either in axial or transverse directions.

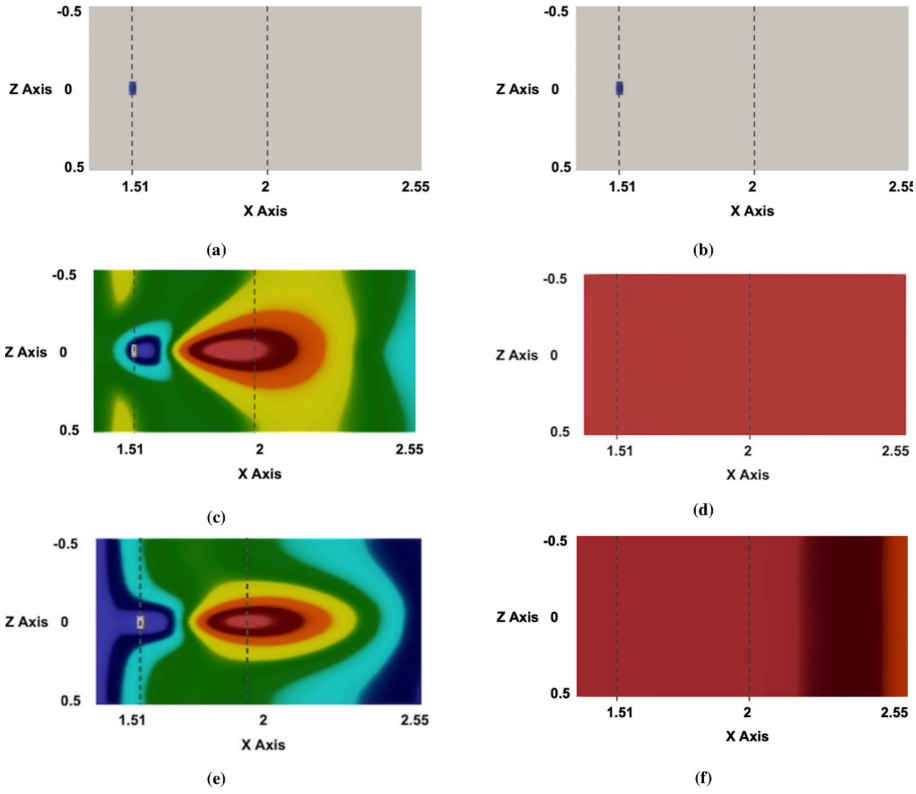

Fig. 5.2: Normalized elevations of the bottom (y/d) for baseline case (right) and in the presence of the turbine (left) for configuration A. (a,b) t = 0 s, (c,d) t = 40 s (e,f) t = 60 s.

The bed morphology evolution near the turbine and downstream its location, is widely different in both configurations. The effect of the wake generated behind the turbine on the bottom, is clearer in configuration A (fig. 5.2) than in the case B (fig. 5.3). To more investigate the difference of the impact of the turbine between the two configurations, two transverse sections are taken into consideration. Such as S_1 at x_0 below the turbine, and

$S2$ at $x - x_0 = 6d$ downstream the turbine for both configurations. The temporal and spatial evolution of each section will be examined in the next sections.

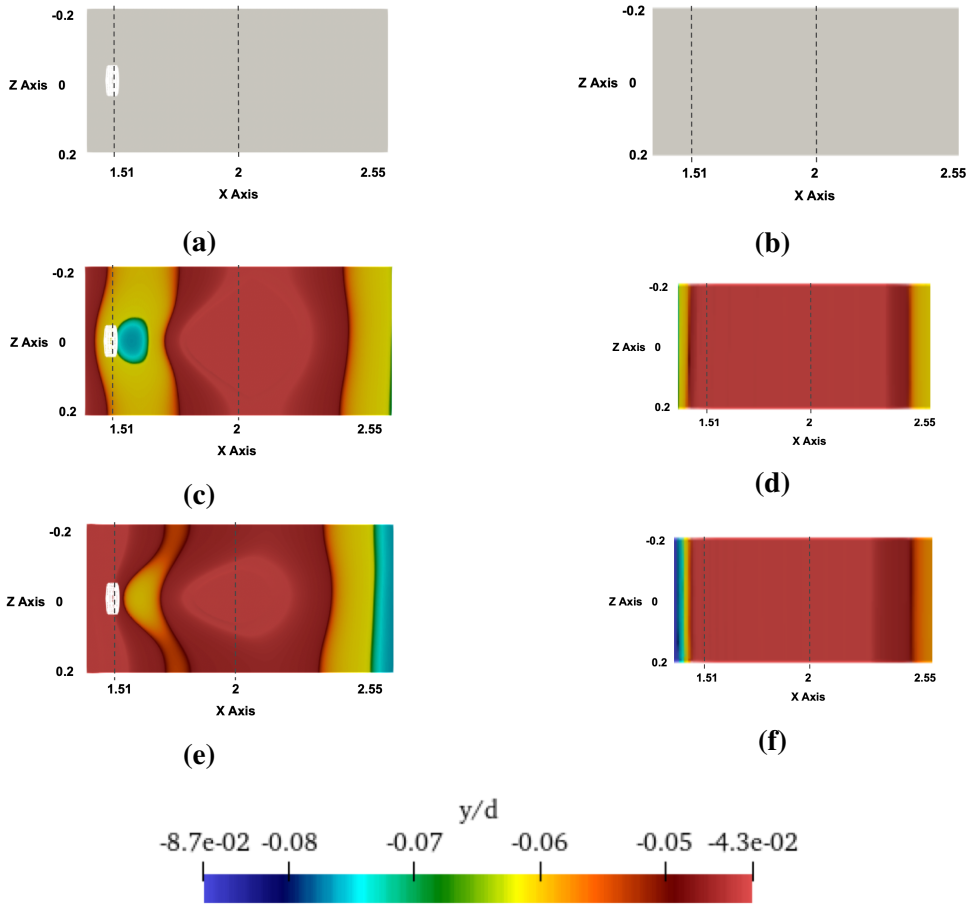

Fig. 5.3: Normalized elevations of the bottom (y/d) for baseline case (right) and in the presence of the turbine (left) for configuration B. (a,b) t = 0 s, (c,d) t = 40 s (e,f) t = 60 s.

5.2.2 Temporal evolution

Figure 5.4 shows the temporal evolution of the bed elevation for configurations A and B. In configuration A, the scour below the turbine at S_1 (fig. 5.4a), occurs in the first 30 s, the bed elevation decreases progressively to reach a scour of $0.09d$. Without the turbine the bed elevation does not variate as much as in the case with the turbine, the maximum depth occurred is $0.04d$ which is much lower than the scour depth when the turbine is installed. While the scour below the turbine for configuration B (fig. 5.4c) is not deeper compared to configuration A, it reaches a maximum depth of $0.07d$. Concerning the temporal variations of the bed downstream the turbine, figures 5.4b and 5.4d show that the erosion process is less important in section S_2 for both configurations during the $60s$ of simulation regarding the scour below the turbine, whereas without the turbine the

curve evolves differently. Moreover, at section $S2$, a continuously slow erosion process is acting in the case A whereas a steady state seems to be reached with the turbine occurring a maximum elevation of $-0.04d$ under the initial interface of the sand layer.

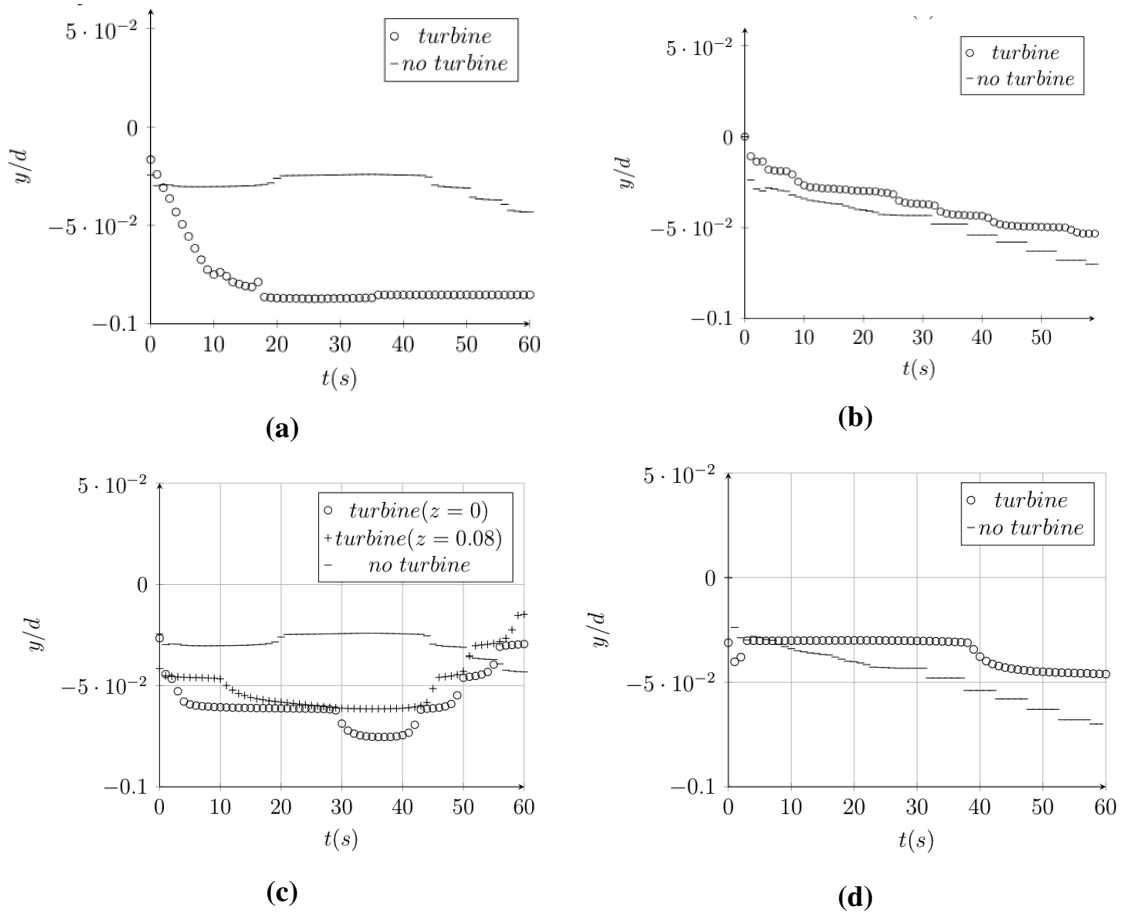

Fig. 5.4: Temporal evolution of normalized bed elevation (y/d) with and without the turbine at (a,c) S_1 and (b,d) S_2 respectively for A (upper) and for B (lower).

Traditionally, the sediment transport and the erosion process are characterised by the bed shear stress and the critical bed shear stress. Particularly, fig. 5.5a shows that the shear stress below the turbine in configuration A is maximum in the first instants of the simulation then it continues to decrease until reaching 0.08 Pa. Note that this is lower than the critical erosion shear stress value of 0.1738 Pa. This could explain the stability of the scour below the turbine from $t = 30$ s, the shear stress carried on the bed below the turbine can not anymore erode the sediments. At section S_2 ($x - x_0 = 6d$) (fig. 5.5b), after $t = 20$ s, the shear stress decreases slowly around a value close to the critical shear stress for both situation (with and without the turbine). This is coherent with a slight bottom evolution. Note that, with the two-phase flow approach, the erosion is not triggered by the bottom shear stress exceeding the critical stress. Here, there is agreement between the model and the erosion theory.

In case B, in figures 5.5c and fig. 5.4a, the bed elevation and the bottom shear stress do not vary as much as in case A at S_1, the erosion process evolves slowly comparing to case A. Even if the bottom elevation does not evolve a lot, the deposition and erosion processes could persist simultaneously. Moreover, the entrained matter could come from the lateral sides due to the turbine's rotation effect. It means that the presence of the turbine increases the local shear stress directly below the turbine and reduce it in the near wake (fig. 5.5). It greatly enhances scour below the turbine (fig. 5.4a and 5.4c).

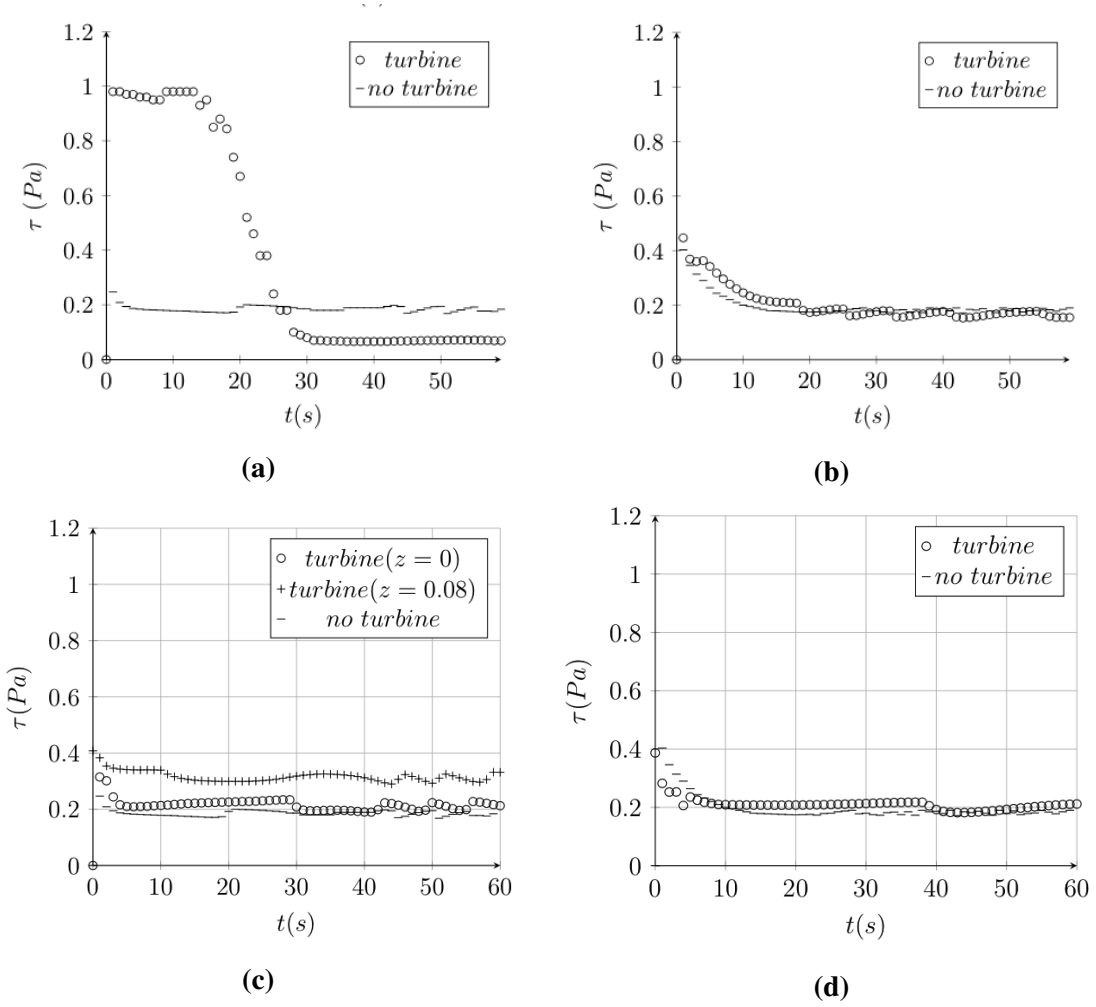

Fig. 5.5: Temporal evolution of bed shear stress with and without the turbine at section (a,c) S_1, (b,d) S_2 respectively for A (upper) and B (lower).

The stability of the scour below the turbine in A can be explained also by the local flow acceleration resulting from flow shrinking between the rotor bottom tip and the top of the sand layer (example fig. 5.6 at t = 40 s). This acceleration decreases the sand layer below the turbine, forms a scour and leads subsequently to a varied morphology downstream the turbine. Figure 5.6 shows the swirl induced on the wake by the rotation of the turbine at $t = 40$ s in configuration A. A simple temporal analysis on two locations

is not enough to state on the process. A spatial analysis should be done, but at particular instants. The equilibrium state occurred below the turbine at t = 40 s in configuration A (fig. 5.5a) and the last instant are chosen to do this afterwards.

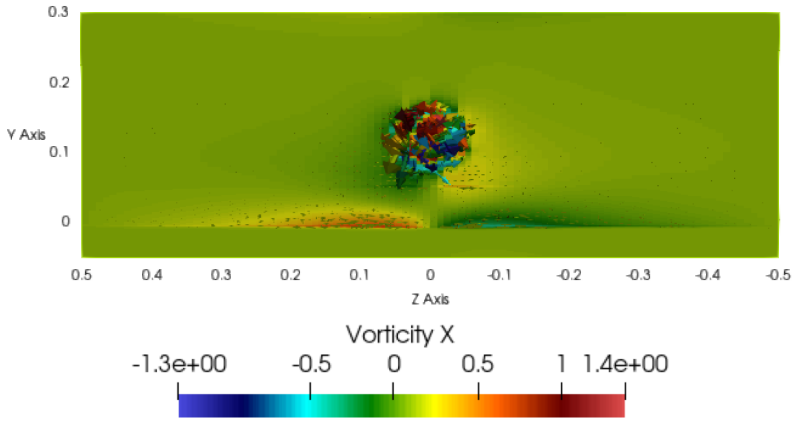

Fig. 5.6: Velocity field in the (y,z) plans colored by the fluid vorticity.

5.2.3 Spatial evolution

The baseline bed morphology evolution (fig. 5.7) is similar between A and B either in cross sections S_1 or S_2 on t = 40 s. Although, in the presence of the turbine, fig. 5.7a shows that the maximum scour occurred below the turbine is $0.084d$ for A and $0.07d$ for B on t = 40 s, otherwise on t = 100 s (fig. 5.7c), the scour in B is not as deep as in the previous moment, and the bed in A is more eroded under the edges of the turbine but remains the scour under the center of the turbine as discussed above. it is noted also that the surface of the scour under the turbine in the case of A is composed of several plates while in the case of B the surface is smooth and continuous. This is due to a phenomenon to be interpreted since there is no variation in mesh sizes of the bottom under the turbine.

Figures 5.7b and 5.7d, show that a phenomenon of deposition is occurred downstream of the turbine in B since the bed elevation is greater than the baseline bed. It explains that there is an important erosion process occurring in the wake of the turbine that leads to deposit the sediments at $6d$ and reach such bed elevation. This erosion may be produced by the sudden variation of the lateral local shear stress (fig. 5.8), so that the eroded sediments hits the edges of the channel and they are transported by the wake to be deposit at $6d$.

Thus, the erosion is more important in case A than in case B. It should be taken into account in the analysis of the turbine's effects.

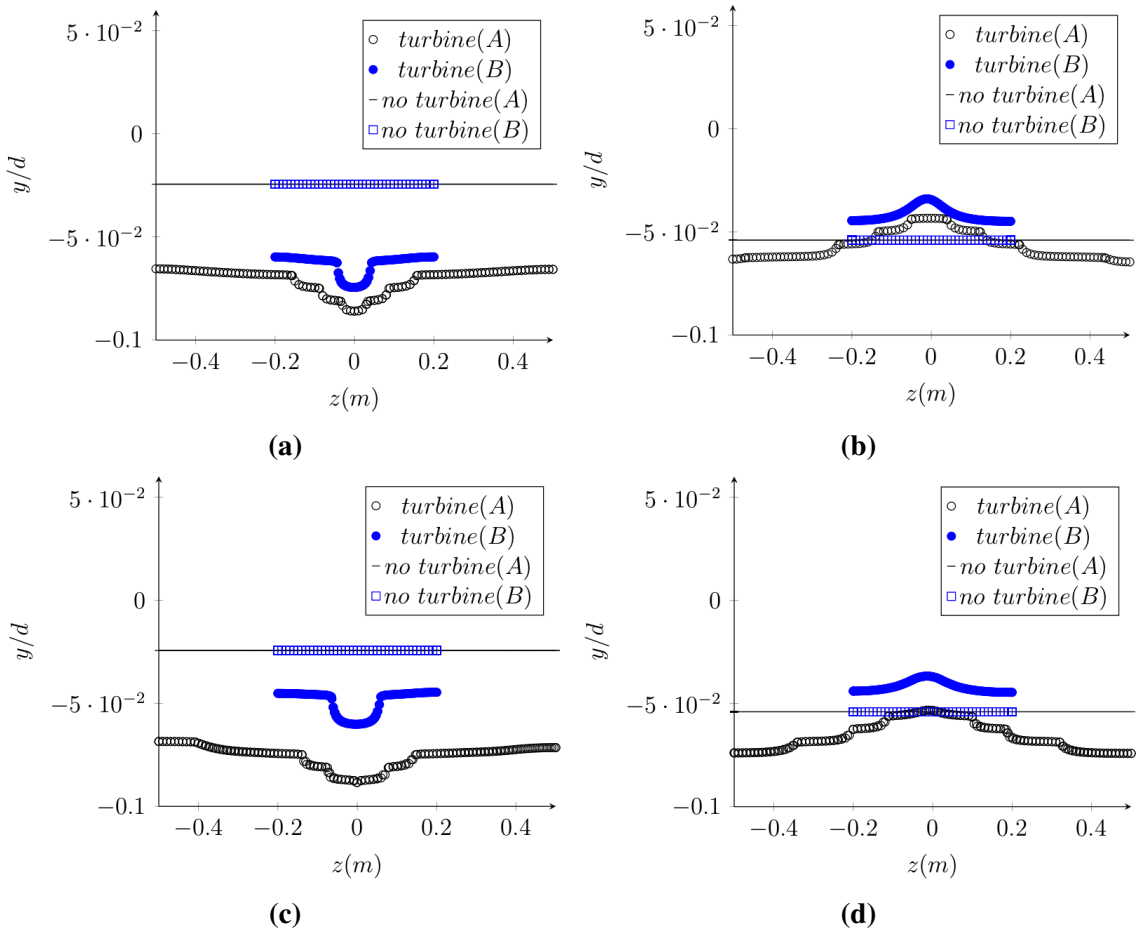

Fig. 5.7: Spatial evolution of bed elevation with and without the turbine at (a,b) sections S_1 and S_2 on $t = 40$ s and (c,d) sections S_1 and S_2 on $t = 100$ s for configurations A (black) and B (blue).

The turbine represented by an actuator BEM model induces a thrust force and a tangential force, these produce a reduction of the axial velocity in the turbine's wake and an increase of the tangential velocity which produces a swirl close to the turbine. This effect has been illustrated in fig. 5.6. It is more visible in fig. 5.9, where the vertical profiles of z-component of the fluid velocity shows the impact of the turbine in the vertical axis across the turbine and in the wake. In the turbine's plane the TIP speed could be observed whereas it vanishes at $6d$ behind the turbine. Figure 5.10 illustrates the high vorticity in turbine's plane in the turbine's location then the reduction of the vorticity $6d$ downstream the turbine.

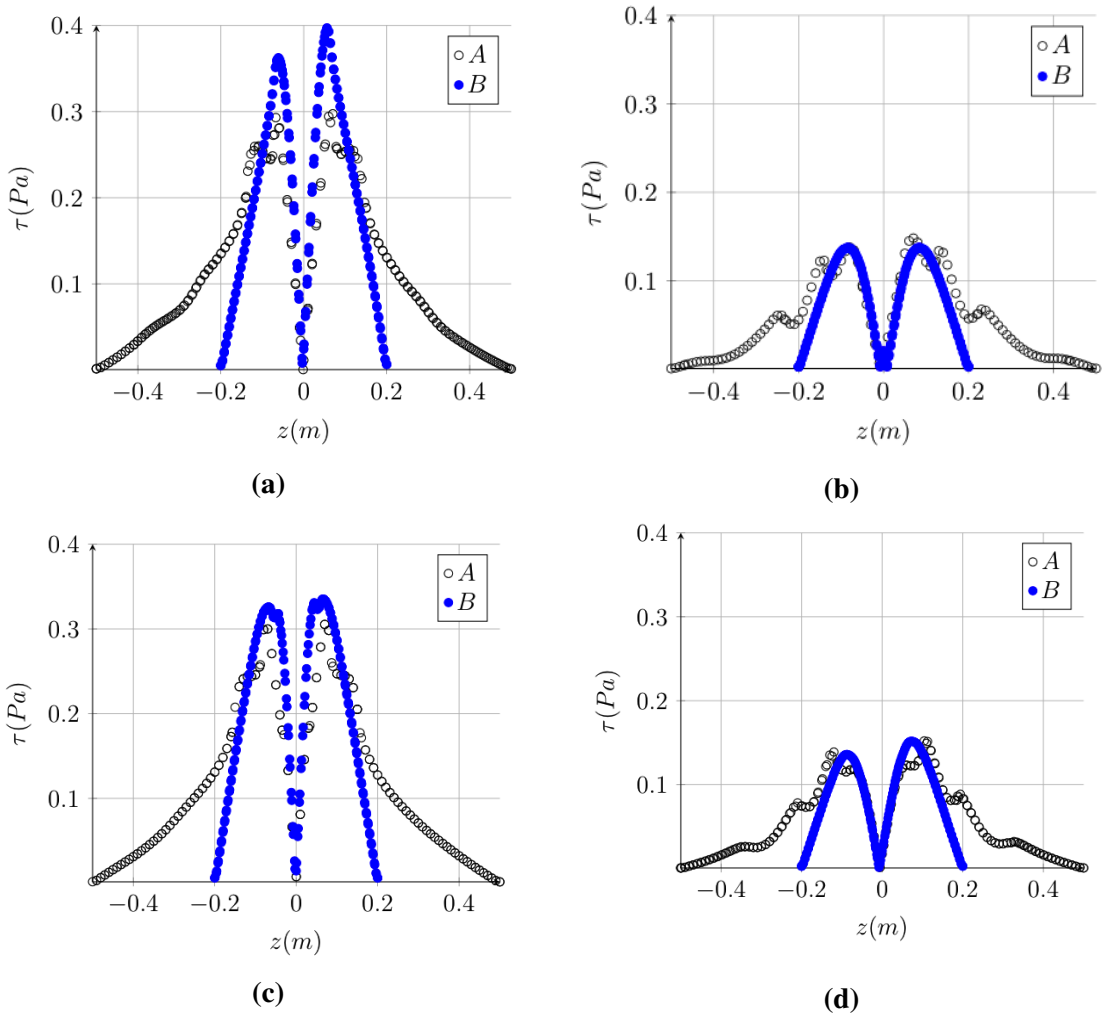

Fig. 5.8: Spatial evolution of shear stress (τ_{yz}) at (a,c) section S_1 and (b,d) section S_2 on t = 40 s (upper) and t = 100 s (lower) for configurations A (black) and B (blue).

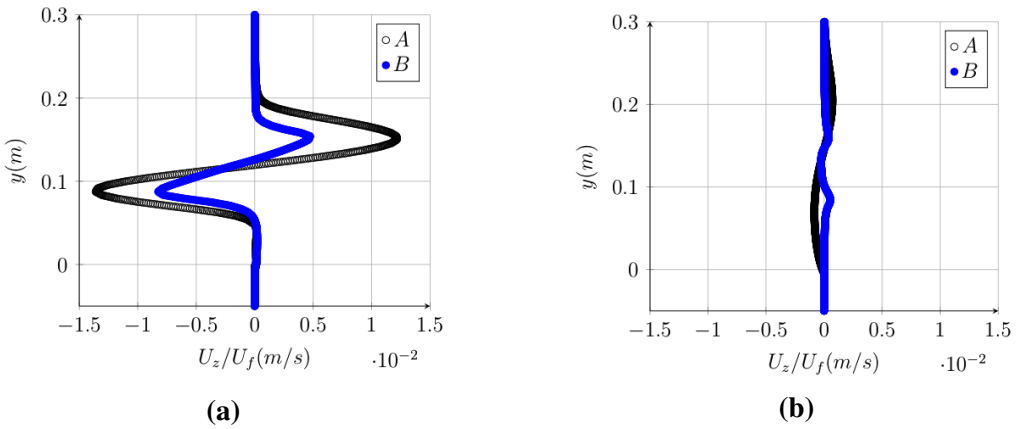

Fig. 5.9: Vertical profiles of velocity , normalized by the mean velocity of the fluid upstream the turbine, U_f at sections S_1 (a) and S_2 (b) for configurations A and B on t = 40 s.

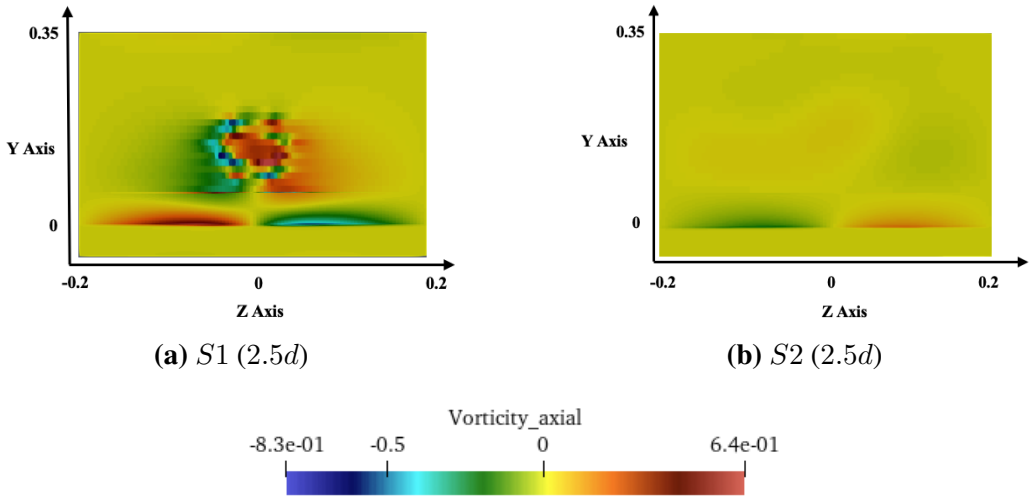

(a) $S1$ $(2.5d)$ **(b)** $S2$ $(2.5d)$

Fig. 5.10: ISO-contouring of the axial vorticity in cross sections areas S_1 (a) and S_2 (b) for configuration B on t = 40 s.

So, the swirl produced by the turbine would have a very local impact. It reveals also the presence of a high vorticity close to the bottom in the turbine's plane (a) that should produce an erosion beneath the turbine. This vorticity decreases with the distance to the canal axis. This explains the localisation of the erosion close to the turbine. Similar results have been obtained with the configuration A. Some differences are appearing on the vorticity intensities close to the bottom that could indicate the greater erosion encountered in the configuration A beneath the turbine regarding the configuration B. This could explain the scour occurred below the turbine of A about $0.09d$ which is deeper than that of configuration B around $0.07d$ (fig. 5.7a).

The drawing of the (yz)-shear stress on the bottom (fig. 5.8) confirms that the rotation of the turbine has a direct impact on the bed below the turbine (fig. 5.8a). The maximum of shear stress is encountered on both side of the turbine and is clearly greater than the critical one. This value is reduced for both cases downstream the turbine (fig. 5.8b) confirming a small implication of the swirl due to the rotation on the bed erosion far away downstream the turbine. Thus, figures 5.9 and 5.8 assure that the flow in the wake does not have the enough capacity to erode the bottom like below the turbine, due to the reducing of the effect of the swirl on the bottom while moving away from the turbine. The differences encountered between the cases A and B on the τ_{yz} (fig. 5.8) shear stress appears as a result of the blockage effect.

Once the flow has stopped eroding under the turbine in A at t = 40 s, then normally there should not be a lot of sediment which is transported in the wake behind the turbine. Fig. 5.11a reveals that the volume fraction of sediment at an altitude y = 0 is not null but remains at ϕ = 0.1 under the turbine at t = 40 s and t = 100 s. This is just above the bed

and is the witness of the low concentrated layer. This sediment could be carried away by the flow easily. It could come from both side of the turbine as the shear stress due to the rotation still be high (around 0.33 Pa) (fig. 5.11b) and erosion process should still take place. Downstream the turbine, the sediment layer is more condensed (fig. 5.11c) and the (yz)-shear stress at this layer (fig. 5.11d) remains close to the critical value.

Then it is important to see what is going on downstream the turbine in A, and compare the results with those of B, considering that there is a significant difference between the results of the two configurations as given in figure 5.11. Figure 5.12 compares the evolution of the bed morphology in axial direction between A and B. The scour generated below the turbine is very clear in A with a minimal value of depth of $0.09d$, contrary to the scour occurred below the turbine in B which reaches a maximum value of depth of $0.07d$. These values are also showed below the turbine in fig. 5.7. The turbine greatly enhances a dune downstream of its location in A and B.

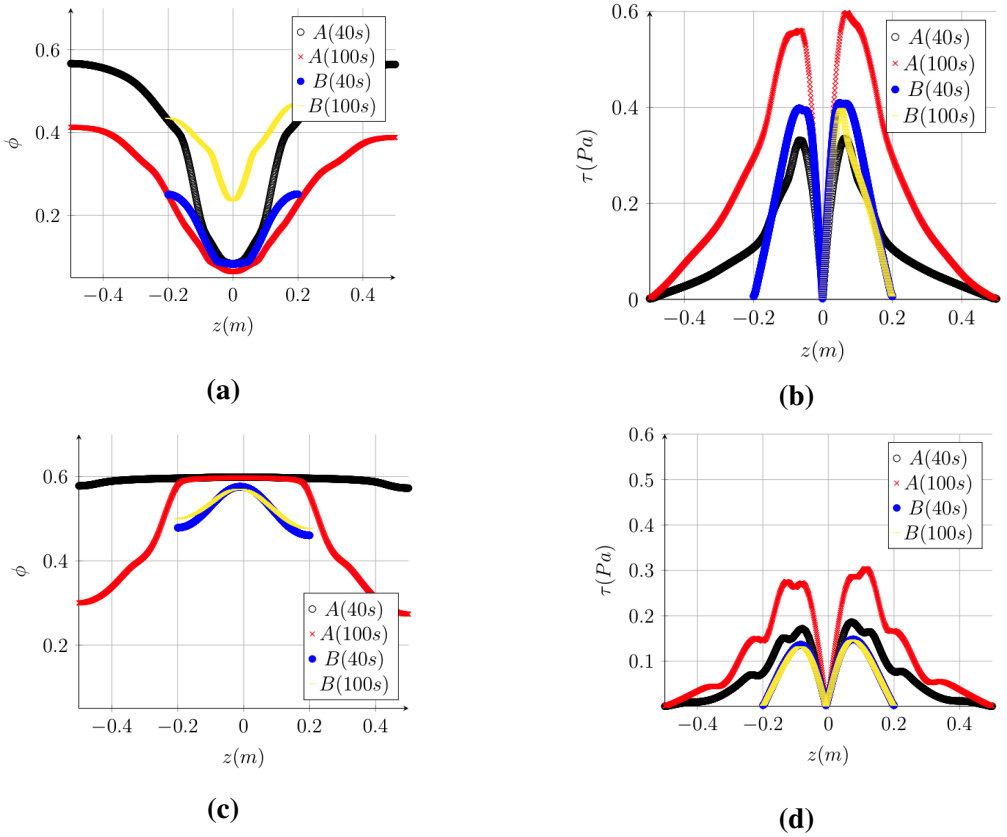

Fig. 5.11: Cross sectional profiles at y = 0 m of (a,c) sediment concentration ϕ and (b,d) shear stress τ_{yz} at sections (a,b) S_1 and (c,d) S_2, on t = 40 s and 100 s.

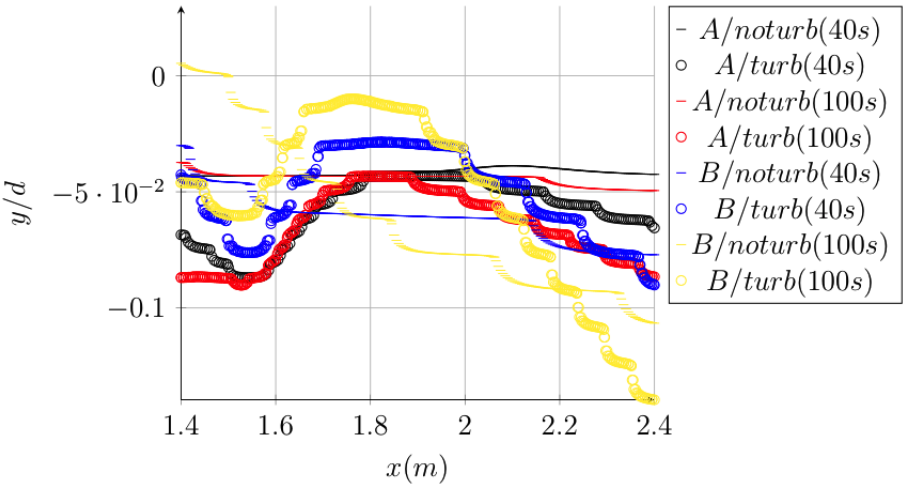

Fig. 5.12: Axial evolution of bed morphology y/d on the bottom of the channel with and without the turbine for configurations A and B on t = 40 s and t = 100 s.

Figure 5.13 shows the difference in dimensionless bed elevation between the baseline and turbine results on S_1 and S_2 for both configurations. The impact of the turbine in A on the erosion process under its location is the most significant during the time (fig. 5.13a) and in the transverse section at t = 40 s (fig. 5.13b). Otherwise, the deposition process of sediments is more obvious in B at section S_2 during the time (fig. 5.13a) and in the transverse section at t = 40 s (fig. 5.13b). Although, the impact of the turbine at S_2 does not differs between both configurations as much as at S_1.

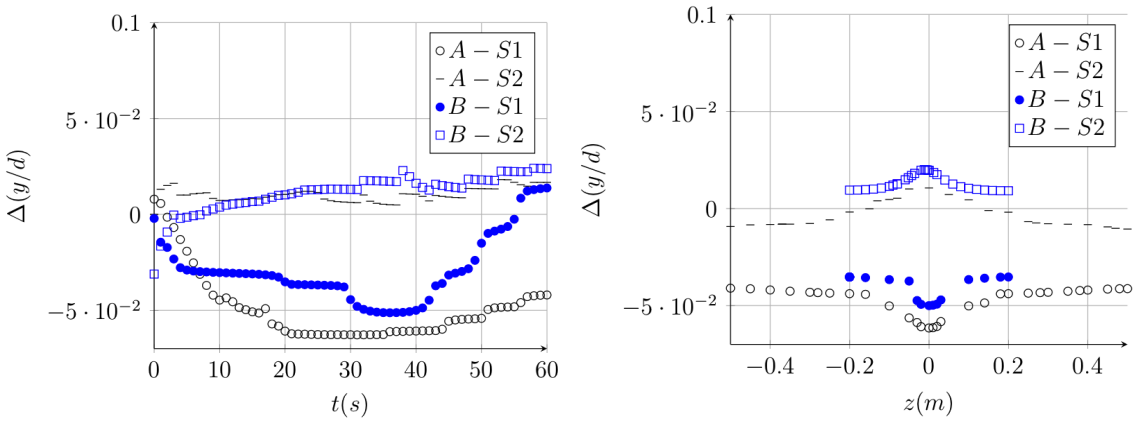

(a) **(b)**

Fig. 5.13: Difference in dimensionless bed elevation between the baseline and turbine results on S_1 and S_2, the erosion is represented in negative values. (a): temporal evolution of $(\Delta y/d)$, (b): spatial evolution of $(\Delta y/d)$.

Furthermore, we can distinguish the blockage effect, when comparing the impact of the turbine between both configurations. The erosion process under the turbine is more

obvious surprisingly for the lower blockage ratio case (configuration A) (fig. 5.12): Concerning the transport of sediments, the impact of the turbine in A is very localized under its location (fig. 5.2), but in B it is more distributed throughout the entire width of the channel at the level of the turbine (fig. 5.3c). This can be explained by an interaction in B between the presence of the walls of the channel and the presence of the turbine. The effect of closed walls leads to bi-dimensioning the flow (little variation in z). From an hydrodynamic point of view, fig. 5.14 shows that the vorticity is important in A under the turbine but it is decreasing while moving away from its location, so that it is almost null at the lateral sides of the channel. On the other hand, the vorticity in B is still remarkable throughout almost the entire width of the channel at turbine level (fig. 5.14). To explain that, we formulate to the hypothesis that the high confinement induces a strong interaction between the channel side effects and the turbine's effect. This leads to a distribution of the vorticity over the entire width and thus reduces its intensity and its capability to erode. Consequently, the erosion under the turbine in case B is lower that in case A and is not yet establish at t = 40 s. Moreover, the transport of sediments is more stable in case A than in case B. In addition, the 3D effect of the turbine in cross sectional areas (fig. 5.14) is clearer in case A than in case B, such as the vorticity fields are widespread below the turbine on both sides occurring an increasing of the bottom shear stress (fig. 5.8) and more eroding the bottom near the edges of the channel (fig. 5.7a). The results of this section are obtained for two channel widths and must be extended to several other widths to be consolidated, this is the investigation of the next section.

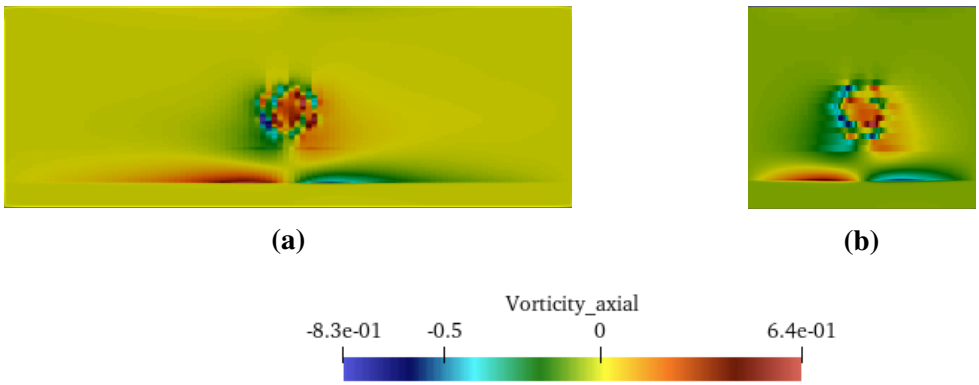

Fig. 5.14: ISO-contouring of the axial vorticity in cross section area S_1 for cases A (a) and B (b) at t = 40 s.

5.3 On the existence of a limit in this behavior

After investigating the blockage ratios effects on the turbine's impact on sediment transport between two configurations, it is crucial to study the effects of different other

blockage ratios to provide a more generalized conclusion. Therefore to strengthen the synthesis provided, a comparison is made between the results of six configurations A, B, C, D, E and F (fig. 5.15). The results of the six configurations are carried out in this section. The numerical properties of the six simulations are similar to the one used for A and B (tables 5.2 and 5.3).

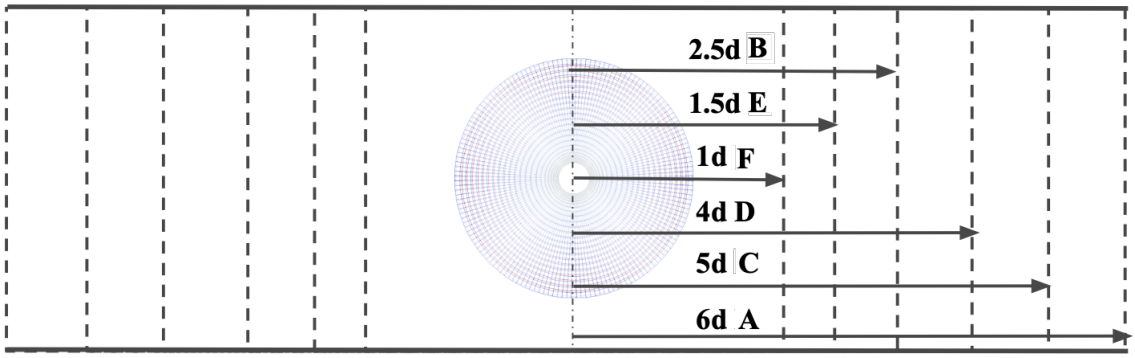

Fig. 5.15: Position of the disk due to the different channel's widths of all configurations in cross-sections (see table 5.4).

Table 5.4 shows the different blockage ratios of the configurations, they are classified decreasingly from the more confined (F) to less confined (A), 10.5% to 1.67% respectively. The mesh is created using the OpenFOAM library package, block Mesh, it is configured as 60 million hexahedral mesh for the wider channel (A) and 20 million cells for the more confined case (F).

Table 5.4: Numerical properties for configurations A, B, C, D, E and F where $c/2$ is the distance between the center of the turbine and the lateral edge of the channel.

	A	**B**	**C**	**D**	**E**	**F**
$c/2$	$6d$	$2.5d$	$5d$	$4d$	$1.5d$	$1d$
blockage-ratio	1.67%	4.2%	2%	2.6%	6.9%	10.5%

5.3.1 Temporal evolution

Figure 5.16 shows the temporal evolution beyond the 120 s of the bed elevation for the six configurations, distinguished by the distance $c/2$ between the center of the turbine and the boundary of the channel, such as $c/2 = 6d, 2.5d, 5d, 4d, 1.5d$ and $1d$ for A, B, C, D, E and F respectively. As noticed, the evolution of the bed elevation is not similar between the configurations during the time. However, they all reached a quasi-equilibrium state of elevation from t = 120 s. The simulations tend to converge beyond this instant. Same

for configuration D, the maximum depth occurred is $0.07d$. Since the blockage ratios of configurations D and C are very close, the bed elevations evolve similarly, nevertheless the scour depth of configuration C is $0.08d$ and deeper than the one of configuration D. In configuration A, the scour below the turbine at S_1, occurs in the first 30 s, the bed elevation decreases progressively to reach a scour of $0.084d$ as noticed in the previous section. While the scour below the turbine for configuration B is not deeper compared to configuration A at t = 40 s as seen in the previous section, although beyond this instant, it varies differently to reach a maximum depth of $0.06d$. On the other hand, the results of configurations E and F are remarkable comparing to other configurations results. The scour occurred is not mush deeper as in the case of other configurations, there is a significant gap between the scour of E ($c/2 = 1.5d$) and the one of B ($c/2 = 2.5d$), even though they differ by just one diameter of confinement. For example, between A and B, the gap is not much important as between B and E, despite the fact that they differ by $(c/2)_B - (c/2)_E = 3.5d$ of confinement, much greater than $1d$. In the next section, the spatial evolution of the scour under the turbine for the configurations A, B, D, E and F are considered, since the temporal variation of the scours between configurations C and D is the same. Figure 5.17 shows the bed morphology near the turbine for all configurations at t = 130 s, the scour below the turbine and the deposition pattern downstream its location is commun for all configurations. However, each one has a different morphology and different scouring depth.

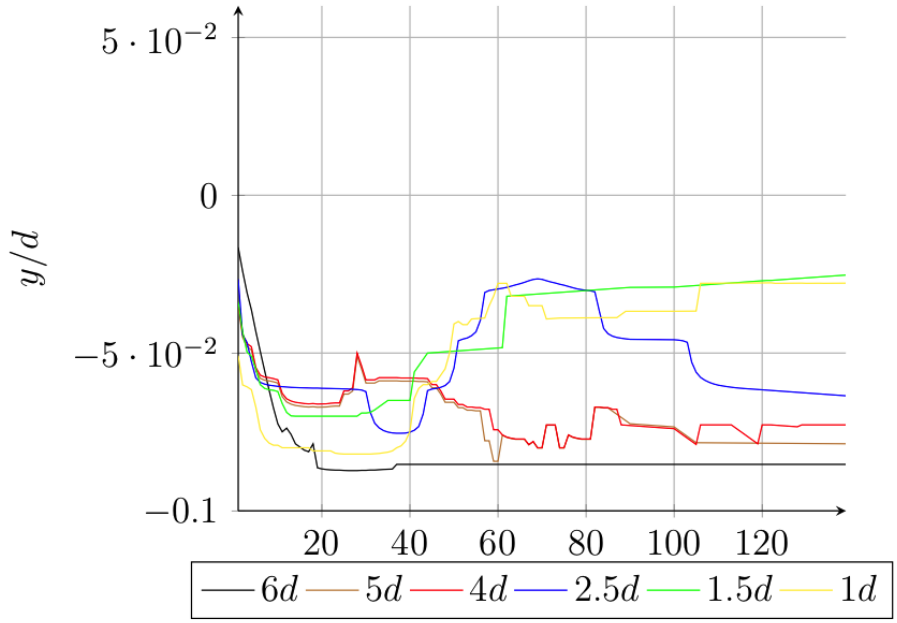

Fig. 5.16: Temporal evolution of normalized bed elevation (y/d) for all configurations under the turbine on S_1.

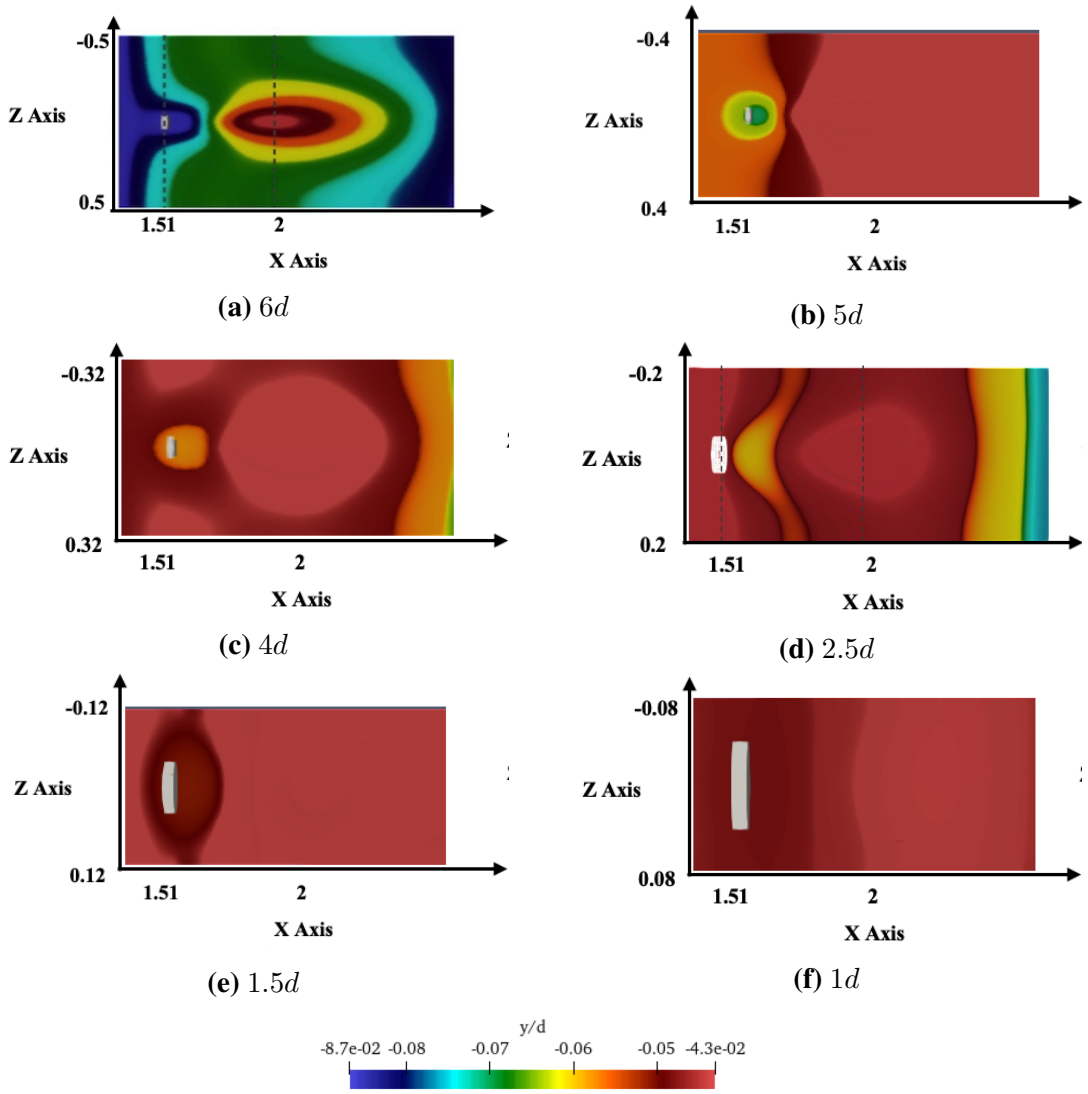

Fig. 5.17: Maps of normalized bed elevation (y/d) for different six blockage ratios configurations; (a) 6d, (b) 5d, (c) 4d, (d) 2.5d, (e) 1.5d, (f) 1d. at t = 130 s.

5.3.2 Spatial evolution

Concerning the spatial evolution, figure 5.18 shows the scouring pattern of the bed below the turbine, at section S_1 (fig. 5.18a), since the shear stress at this section is high enough to erode the sediments (fig. 5.19a) and downstream the turbine at section S_2 (fig. 5.18b) when the shear stress (fig. 5.19b) is not as important as at S_1. The impact of the turbine is remarkable by the scouring occurred below its position and the deposition term generated at S_2. The erosion is more important below the turbine when the center of the turbine is far enough from the lateral borders of the channel (for $c/2 = 6d$), the depth of the scour is about $0.084d$, then it decreases degradably when the turbine is more confined. The depth of the scour occurred when $c/2 = 4d$ is about $0.07d$, and $0.062d$ for $c/2 = 2.5d$.

The ones for $c/2 = 1.5d$ and $c/2 = 1d$ are very close but so far from the depth of $c/2 = 2.5d$. This could explain that the impact of the turbine on the bottom is not localized below its location when it is so confined ($c/2 = 1.5d$ and $c/2 = 1d$), this is clear in figures 5.20g and 5.20i when the vorticity evolution around the disc is not confined locally below its location as in the case of other configurations but it is spread out until the lateral edges of the channel, that is why the shear stress is the less important between the configurations, therefore the erosion is less obvious.

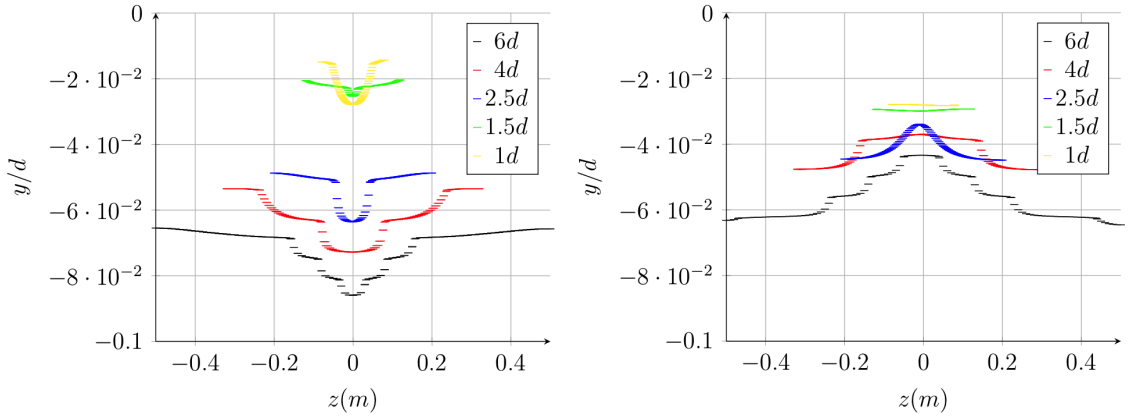

(a) S_1 **(b)** S_2

Fig. 5.18: Spatial evolution of bed elevation for the five configurations on a) S_1 and b) S_2 at $t = 40$ s.

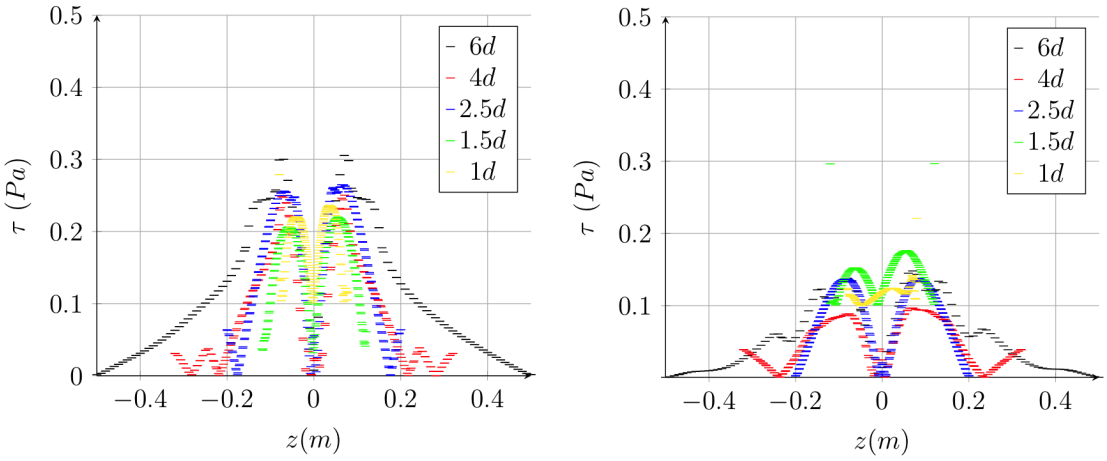

(a) S_1 **(b)** S_2

Fig. 5.19: Spatial evolution of shear stress (τ_{yz}) on a) S_1 and b) S_2 at $t = 40$ s.

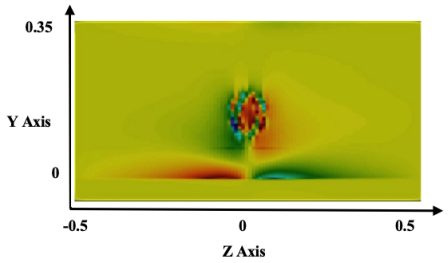

(a) $6d$ $(S1)$

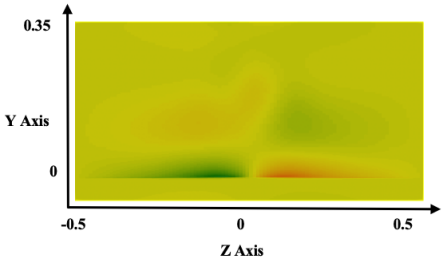

(b) $6d$ $(S2)$

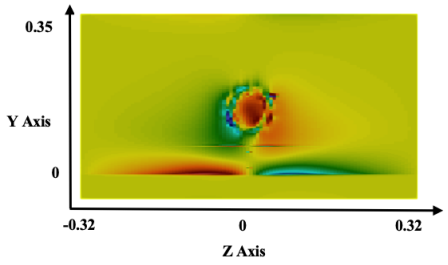

(c) $4d$ $(S1)$

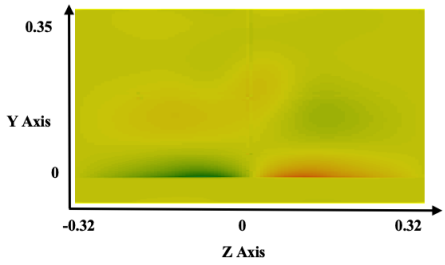

(d) $4d$ $(S2)$

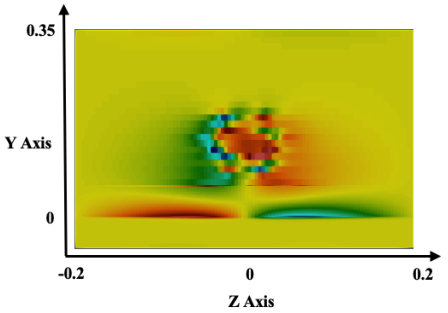

(e) $2.5d$ $(S1)$

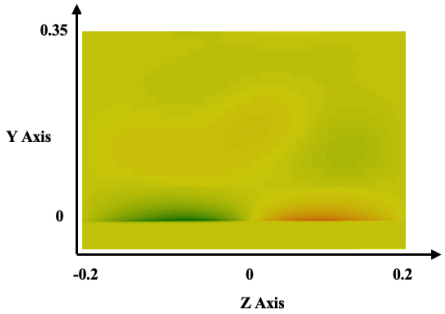

(f) $2.5d$ $(S2)$

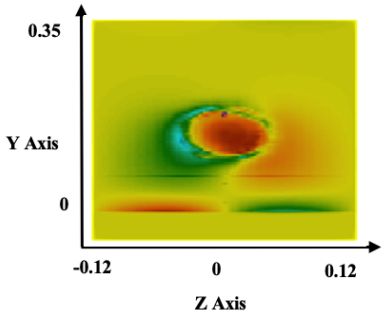

(g) $1.5d$ $(S1)$

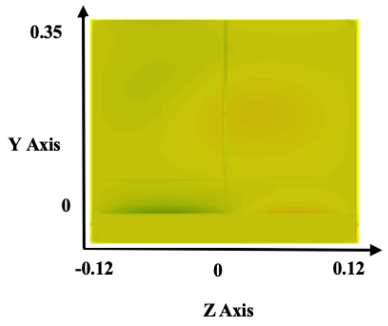

(h) $1.5d$ $(S2)$

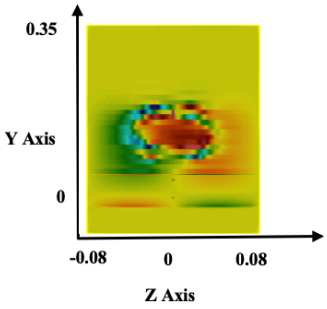

(i) $1d$ $(S1)$

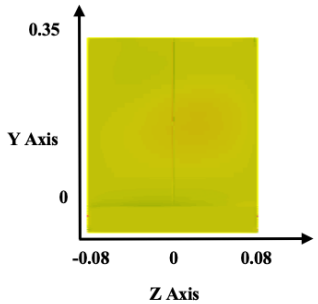

(j) $1d$ $(S2)$

Fig. 5.20: ISO-contouring of the axial vorticity in cross sections areas S_1 (a) and S_2 (b) for all configurations.

5.4 Summary

The study in this chapter aims to investigate the effect of different blockage ratios on the turbine-sediment interaction. The results show a significant impact of the blockage ratio on the evolution of the morphology of the bottom downstream the turbine; the lower the ratio is, the more the impact of the turbine in the near wake is more obvious.

These results are in accordance with the experimental results of Williams and R. Bolisetti (2019) who investigated the scouring mechanism around a cylinder. They studied the effect of the ratio of cylinder diameter and the channel width on the erosion produced at the cylinder's location. The authors thus showed that there is an important effect of the proximity of the lateral walls on the erosion of the sedimentary bottom and that the stronger the blockage, the more the side walls have an impact on erosion. However, this must be mitigated, because according to their experiences this is only true if the ratio D/ds (pier diameter to sediment diameter) exceeds 100. Our results are not obtained for a vertical cylinder but for a 80 mm diameter turbine, the sediment diameter being 0.25 mm. Configuration A is realized for a blocking rate of 0.0166, configuration B of 0.0416, configuration C of 0.02, configuration D of 0.026, configuration E of 0.069, and configuration F of 0.1. These values are closed to those used in the experiment of Williams and R. Bolisetti (2019). In addition, the ratio of the turbine diameter to the sediment diameter is 320. The erosion is more important below the turbine when the center of the turbine is far enough from the lateral borders of the channel (configuration A) therefore the impact of the turbine is restricted below its position, the depth of the scour is about $0.084d$. However, the erosion decreases degradably when the turbine is more confined, the depth of the scour occurred for configuration F is about $0.024d$, due to the interaction between the turbine's impact and the walls effects.

Moreover, it is crucial to study the impact of the confinement of two axial-flow turbines on the interaction turbine-sediment, this is the subject of the next chapter.

Chapter 6

Interaction between hydrokinetic turbines and large scale bedforms

6.1 Introduction

After investigating the impact of blockage ratios on the turbine-sediment interaction, it is crucial to study the impact of two interacted turbines on the sediment transport. This chapter presents the results obtained for the simulation of the interaction between two axial turbines and their impact on the bedform morphology. It consists in considering one sediment class, sand of one diameter, and two horizontal axis turbines with an axial flow direction corresponding to the riverine case. The approach is configured with four different axial inter-turbines distances: configurations A_1, A_2, A_3 and A_4. The numerical properties are explained below for all the configurations.

6.2 Numerical Setup

Four different configurations are carried out in this section, for which the interaction of two axial hydrokinetic turbines, T_1 and T_2, are simulated in each configuration. The turbines are placed one behind the other axially in the computational channel. A layer of sand is spread out uniformly on the bottom of the channel below the turbines. Same hydrodynamic and sediment properties of the last chapter are configured here for both configurations. The axial distance inter-turbine is the only parameter that differs between the four configurations, it is defined as $x_1 = 4d$ for configuration A_1, $x_2 = 7d$ for configuration A_2, $x_3 = 10d$ for configuration A_3 and $x_4 = 13d$ for configuration A_4 (see fig. 6.1), where d is the diameter of each turbine. We use the same hydrodynamic conditions as in Chapter 5. Thus $TSR = 2.1$, and $TI = 3\%$. Table 6.1 recalls the numerical properties and the different inter-turbine distances of the configurations. The physical parameters

used in the code are the same as in previous chapter and are provided in table 5.3. As in the previous cases, the blades are modelled using 23 discrete NACA 63418 elements among their span in accordance with the blade profile provided in Chapter 3. Also, the fluid turbulence model $k-\epsilon$ has been used for both configurations and a time step of 10^{-3} s is imposed to approach the convergence.

The critical Shields parameter is θ_{cr} = 0.043 which corresponds to a critical shear stress value of 0.1738 Pa.

Table 6.1: Numerical hydrodynamic properties for configurations A_1, A_2, A_3 and A_4 where a, b, c are the dimensions of the channel, x' is the position of the first turbine, TI is the turbulent intensity.

a*b*c	d	x'	TSR	TI	U_∞
$4 * 0.35 * 1$ m	0.08 m	1.51 m	2.1	3%	0.8 m/s

Table 6.2: Numerical hydrodynamic properties for configurations A_1, A_2, A_3 and A_4 where x' and x'' are the position of the first and second turbine respectively from the inlet, d_i is the distance inter-turbines.

	A_1	A_2	A_3	A_4
x' (T_1)	1.51 m	1.51 m	1.51 m	1.51 m
x'' (T_2)	1.82 m	2.06 m	2.3 m	2.54 m
d_i	$4d$	$7d$	$10d$	$13d$

6.2.1 Computational mesh

The computational domain is a block of $a = 4m$ length along the x-axis, b = 0.3 m deep on y-axis and c = 1 m width on z-axis (see fig.6.1). The disc of the first turbine T_1, is placed at 1.51 m downstream the inlet, thus the one that represents the second turbine T_2 is located at a distance d_i far from the first disc (fig. 6.1) and listed in table 6.2. The mesh is created using blockMesh, it is configured as 60 million hexahedral mesh.

6.2.2 Boundary Conditions

The conditions are the same as used in Chapter 5. They are synthetised in table 6.3.

Table 6.3: Summary of the boundary conditions implemented in the simulation of all configurations: zG = zeroGradient, iO = inletOutlet, fV = fixedValue, FP = fluxPressure, hP = hydrostatic pressure and logP = logarithmic profile.

Boundary	*type*	u_f	u_s	p	k	ε	ϕ
inlet (flow)	patch	logP	logP	zG	fV	zG	fV
inlet (sed)	wall	fV(null)	fV(null)	zG	fV	zG	zG
top	patch	zG	zG	zG	zG	zG	zG
bottom	wall	fV(null)	fV(null)	FP	zG	zG	zG
outlet	patch	iO	iO	hP	zG	zG	zG

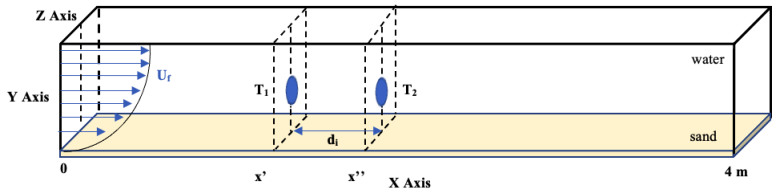

Fig. 6.1: Initial state of domain, position of the turbines (T_1 and T_2), logarithmic profile of the fluid velocity at inlet, the sheet layer of sands on the bottom (yellow color); d_i is the inter-turbines distance (see table 6.1).

6.3 Results

6.3.1 Wake characterization

Figure 6.2 presents axial velocity maps between the two interacted turbines. The wake behind the downstream turbine is altered by the influence of the upstream turbine. The downstream velocity deficit still remains contained in an axial strip, which is slightly larger than the one behind a single turbine. The wake also seems to recover slightly faster in terms of velocity deficit. The degradation of the axial velocity profiles is significant until $2d$ downstream the turbines. The velocity profiles under the first turbine (T_1) are similar for all the inter-distances configurations, since the upstream velocities of (T_1) are equal, however those under the second turbine (T_2) are different between the configurations (fig. 6.3).

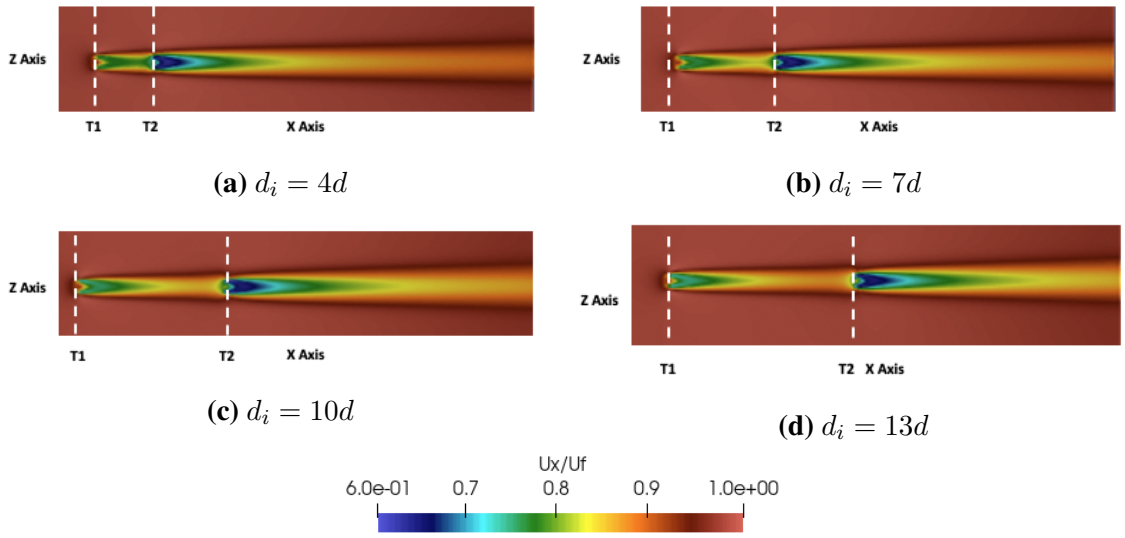

(a) $d_i = 4d$ **(b)** $d_i = 7d$

(c) $d_i = 10d$ **(d)** $d_i = 13d$

Fig. 6.2: Spatial evolution of bed elevation with the presence of two turbines apart with different d_i for configurations A_1 (a), A_2 (b), A_3 (c) and A_4 (d).

Indeed, depending on the inter-device distance, the flow at the location of the downstream turbine may not be homogeneous and may suffer as well from a velocity deficit as compared to the upstream velocity of the first turbine. As the inter-distance increases, as the upstream velocity value of the downstream turbine increases, then the tangential velocities behind the upstream turbine are more important (fig. 6.3). Figure 6.4 illustrates the high vorticity in the plane of the both turbines for all configurations. The local impact of the swirl produced by the turbine on the bottom is very significant, but differs between the turbines; it is almost similar for all the configurations below the first turbine T_1 otherwise it varies slightly below the second turbine T_2. That should produce an erosion beneath the turbine. Some differences are appearing on the vorticity intensities close to the bottom that could indicate the greater erosion encountered beneath the first turbine regarding the second one. Thus it is crucial to study the interaction between the turbine and the sediment on the bottom.

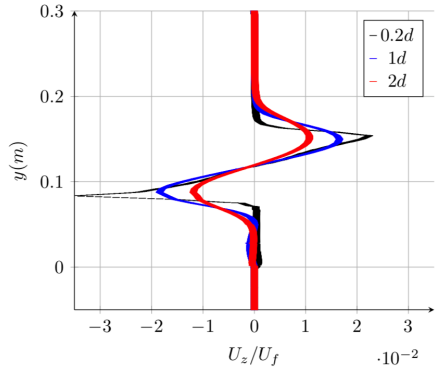

(a) $d_i = 4d, T1$

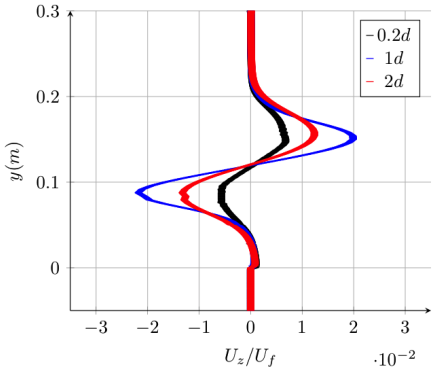

(b) $d_i = 4d, T2$

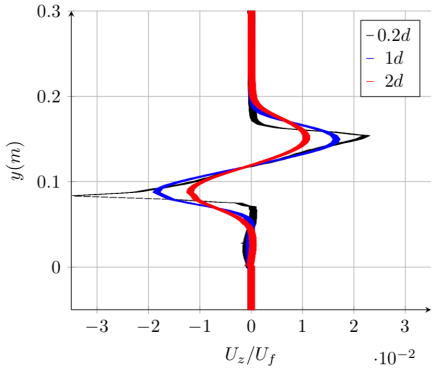

(c) $d_i = 7d, T1$

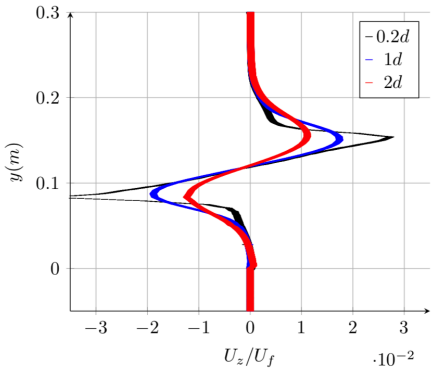

(d) $d_i = 7d, T2$

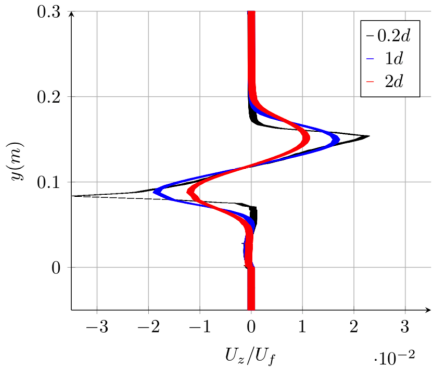

(e) $d_i = 10d, T1$

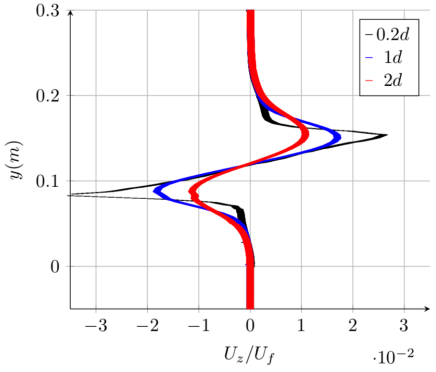

(f) $d_i = 10d, T2$

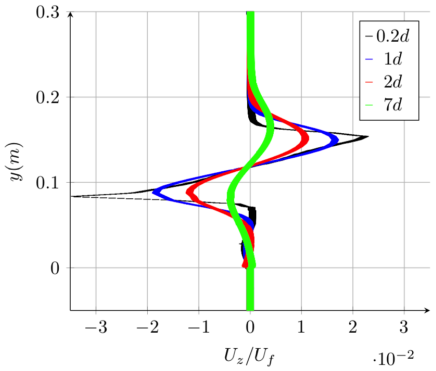

(g) $d_i = 13d, T1$

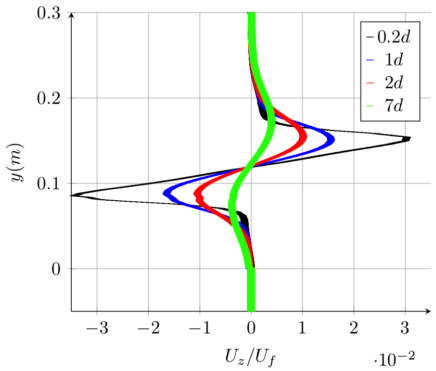

(h) $d_i = 13d, T2$

Fig. 6.3: Vertical profiles of velocity, normalized by the mean velocity of the fluid U_f upstream the turbines T_1 and T_2 for all configurations, at $0.2d$ (black), $1d$ (blue) and $2d$ (red), $7d$ (green).

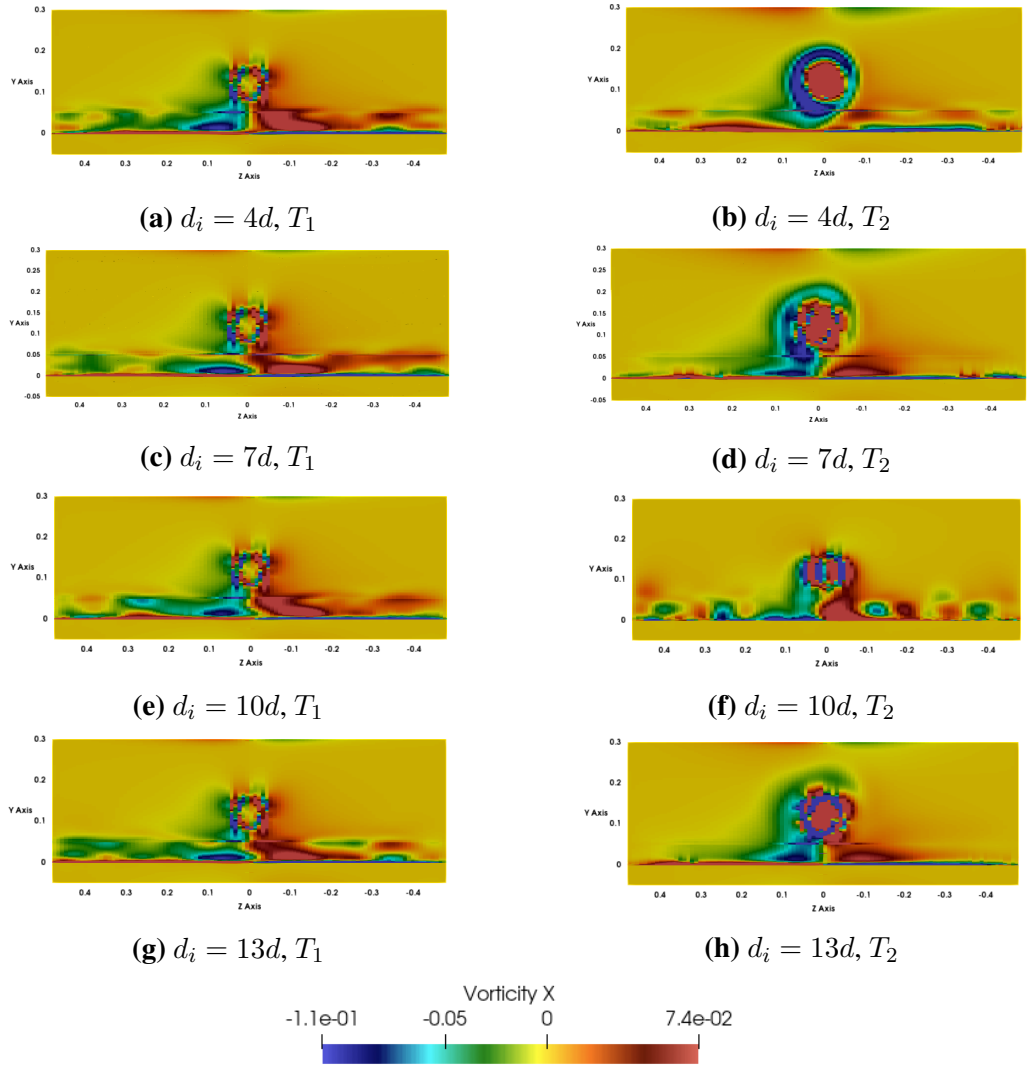

(a) $d_i = 4d$, T_1 **(b)** $d_i = 4d$, T_2

(c) $d_i = 7d$, T_1 **(d)** $d_i = 7d$, T_2

(e) $d_i = 10d$, T_1 **(f)** $d_i = 10d$, T_2

(g) $d_i = 13d$, T_1 **(h)** $d_i = 13d$, T_2

Fig. 6.4: ISO-contouring of the axial vorticity near the turbines T_1 and T_2 for all configurations, at $0.2d$, $1d$ and $2d$.

6.3.2 Turbines-sediments interaction

Figure 6.5 shows the modifications of the sediment bed due to the presence of the two turbines T_1 and T_2 for configurations A_1, A_2, A_3 and A_4 (fig. 6.5b, 6.5c, 6.5d and 6.5e respectively). Figure 6.6 presents the distribution of the bed shear stress with and without the turbines. The impact of the turbines on the bed morphology is clear when comparing the results with the baseline case either in bed elevation in fig. 6.5a or the bed shear stress in fig. 6.6a. The clearest feature is the scour under each turbine so that the shear stress is high enough at their position, also the formation of two significant sedimentary bodies downstream the turbines, one behind T_1, and other behind T_2 of each configuration extending all along its axis in the far wake, so that the shear stress at this position is not as high as near the turbines. However, the bed form without the turbines is dominated by

the sand ripples which are not homogeneous due to the canal walls effect.

The scour depth near the first turbine is almost the same for the four configurations, but we distinguish the difference of the scouring near the second turbine, since the position of the second turbine is widely different among the configurations (mainly in configuration A_2 6.5c). Thus, several changes in bed morphology have been found in the zone limited by the two turbines T_1 and T_2 between the configurations. The more the distance between turbines d_i increases, the more the bed is evolved. When $d_i = 4d$, T_2 is close enough to T_1 (fig. 6.2a), so that the upstream velocity of T_2 is the lowest compared to the ones of other configurations, this makes the flow less accelerated around the disk compared to other configurations, therefore providing a less scouring under the second turbine.

To more investigate the difference of the impact of the turbines on the bed between the configurations, three transverse sections are taken into consideration near each turbine. The first one is at the turbine's position $0d$ ($x = 1.5$ for T_1), and the others at $1d$ and $2d$ downstream the turbine. The spatial evolution of the bed at each section at $t = 60$ s will be examined in the next parts.

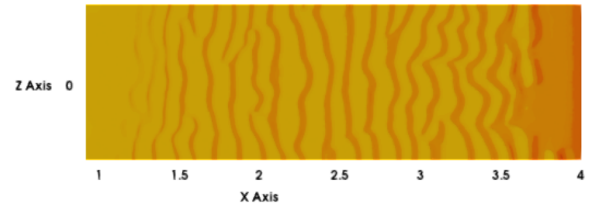

(a) *no turbine*

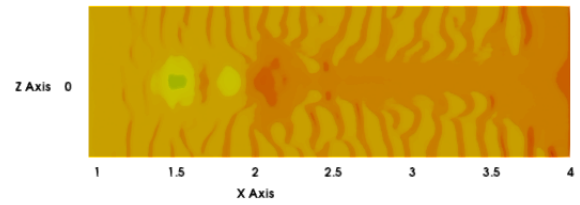

(b) $d_i = 4d$

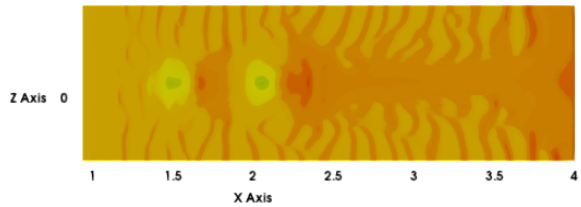

(c) $d_i = 7d$

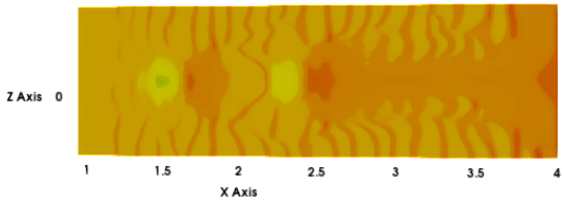

(d) $d_i = 10d$

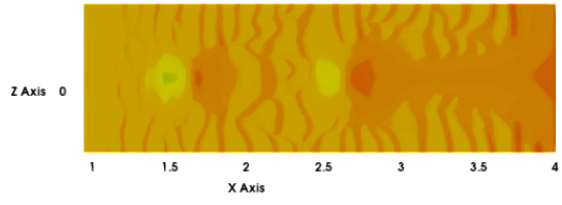

(e) $d_i = 13d$

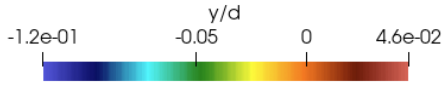

Fig. 6.5: Normalized elevations of the bottom (y/d) with and without the turbines; (a) baseline case, (b) d_i = $4d$, (c) d_i = $7d$, (d) d_i = $10d$ and (e) d_i = $13d$ at 60 s.

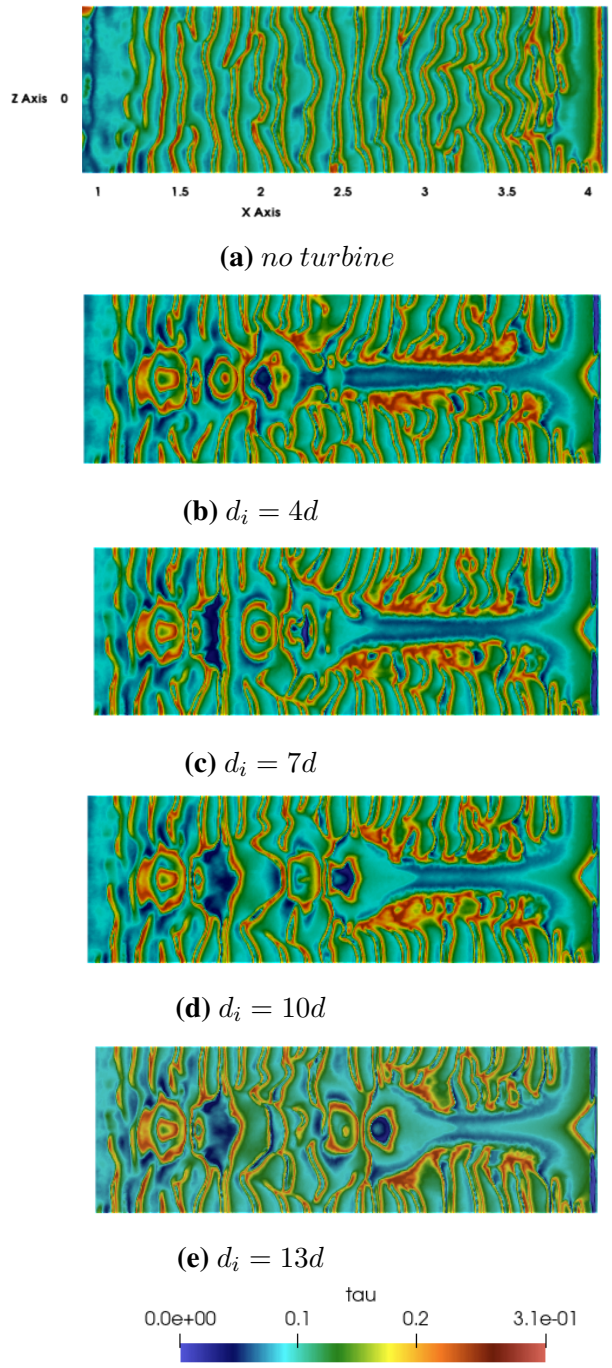

(a) *no turbine*

(b) $d_i = 4d$

(c) $d_i = 7d$

(d) $d_i = 10d$

(e) $d_i = 13d$

Fig. 6.6: Spatial evolution of bed shear stress with and without the turbines; (a) baseline case, (b) $d_i = 4d$, (c) $d_i = 7d$, (d) $d_i = 10d$ and (e) $d_i = 13d$ at 60 s.

Figure 6.7 shows the evolution of the bed shear stress below the turbines in the (y,z) plane throughout the sandy bed. It highlights on the impact of the turbine into a significant depth of the sedimentary bottom. This impact is almost similar under T_1 for all configurations since the position and the numerical conditions of T_1 are the same. However, the bed shear stress under T_2 evolves differently between the configurations (fig. 6.7b, 6.7d, 6.7f and 6.7h). The farther the second turbine is from the first, the more the shear stress

increases and therefore the impact on the bottom is greater.

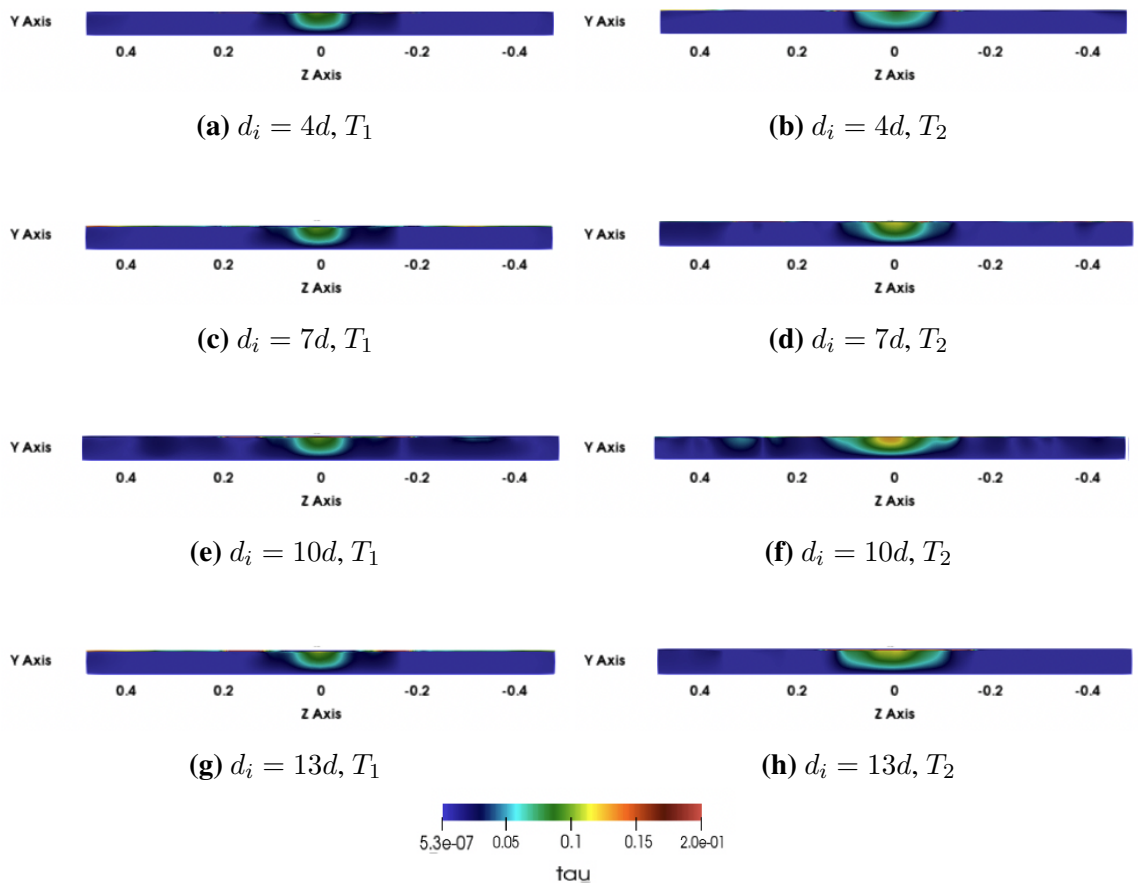

(a) $d_i = 4d, T_1$ **(b)** $d_i = 4d, T_2$

(c) $d_i = 7d, T_1$ **(d)** $d_i = 7d, T_2$

(e) $d_i = 10d, T_1$ **(f)** $d_i = 10d, T_2$

(g) $d_i = 13d, T_1$ **(h)** $d_i = 13d, T_2$

Fig. 6.7: Spatial evolution of bed shear stress in (y,z) plane below the two turbines for configurations A_1 (a,b), A_2 (c,d), A_3 (e,f) and A_4 (g,h).

Figures 6.8 and 6.9 present the spatial evolution of the normalized elevation of the bottom and the bed shear stress in the plane (y,z) with and without the turbines. First we notice in figures 6.8a, 6.8c and 6.8e, that without the turbine the bed does not variate as much as in the case with turbine, the maximum depth occurred is 0.018d, whereas under T_1 and T_2 the erosion is significant comparing to the depth of non-turbine case, the scour reaches a depth of $0.03d$ at $0d$ (fig. 6.8a and 6.8b) and $0.024d$ at $1d$ downstream the turbines T_1 and T_2 (fig. 6.8c and 6.8d). Table 6.4 shows the position of the cross sections of each configuration. The presence of the turbine accelerates the flow around the disc, thus increases the shear stress and enhances the capability of the flow to erode the sediments, thus forms a scour and leads subsequently to a varied morphology downstream the turbine.

Table 6.4: Position of the cross sections near T_1 and T_2 for each configuration.

	0d	**1d**	**2d**
T_1	$x = 1.5$ cm	$x = 1.58$ cm	$x = 1.66$ cm
T_2 $d_i =$ **4d**	$x = 1.82$ cm	$x = 1.9$ cm	$x = 1.98$ cm
T_2 $d_i =$ **7d**	$x = 2.06$ cm	$x = 2.14$ cm	$x = 2.22$ cm
T_2 $d_i =$ **10d**	$x = 2.3$ cm	$x = 2.38$ cm	$x = 2.46$ cm
T_2 $d_i =$ **13d**	$x = 2.54$ cm	$x = 2.62$ cm	$x = 2.7$ cm

The turbine represented by an actuator BEM model induces a thrust force and a tangential force, these produce a reduction of the axial velocity in the turbine's wake and an increase of the tangential velocity which produces a swirl close to the turbine. This effect has been illustrated in fig. 6.4. It is more visible in fig. 6.3, where the vertical profiles of z-component of the fluid velocity shows the impact of the turbine in the vertical axis across the turbine and in the wake. In the turbine's plane the TIP speed could be observed whereas it vanishes lightly at $2d$ behind the turbine. Figure 6.4 illustrates the high vorticity in turbine's plane in the turbine's location then the reduction of the vorticity $2d$ downstream the both turbines. So, the swirl produced by the turbine would have a very local impact. It reveals also the presence of a high vorticity close to the bottom in the turbine's plane that should produce an erosion beneath the turbine. This vorticity decreases with the distance to the canal axis. This explains the localisation of the erosion close to the turbine. Some differences are appearing on the vorticity intensities close to the bottom under T_1 that could indicate the greater erosion encountered beneath the first turbine regarding T_2. This could explain the scour occurred below T_1 (about $0.03d$) which is deeper than that below T_2 (around $0.024d$) (fig. 6.8).

However, at $2d$, a phenomenon of deposition is occurred downstream of the turbines T_1 (fig. 6.8e) and T_2 (fig. 6.8f) since the bed elevation is greater than the baseline bed. It explains that there is an important erosion process occurring close to the turbine that leads to deposit the sediments at $2d$ and reach such bed elevation. This erosion may be produced by the sudden variation of the lateral local shear stress (6.9), so that the eroded sediments hits the edges of the channel and they are snared by the wake to be deposit at $2d$. The maximum value of bed shear stress, for all configurations and at the three cross sections for both turbines, is almost 0.25 Pa, which is greater than the critical value of bed

shear stress (0.1738 Pa) calculated in the last chapter. Note that the erosion process still occurred from $0d$ until $2d$ downstream the turbines, even though a sedimentary bodies are formed at $2d$.

As mentioned above, the evolution of the bed under T_1 is the same for all configurations, except at $2d$ (fig. 6.8e) the elevation for A_1 is little different from the others, this could be explained by the interaction of T_1 and T_2 on the bottom since the second turbine is placed at $4d$. Otherwise, figure 6.8c shows that the scours under T_1 and T_2 which is located at $7d$ downstream the first turbine, are the same. This may be the reason of an accumulated impact of the interaction of both turbines at $7d$. On the other hand, the erosion under T_2 procures the same scour for $4d$, $10d$ and $13d$, which is about $0.024d$.

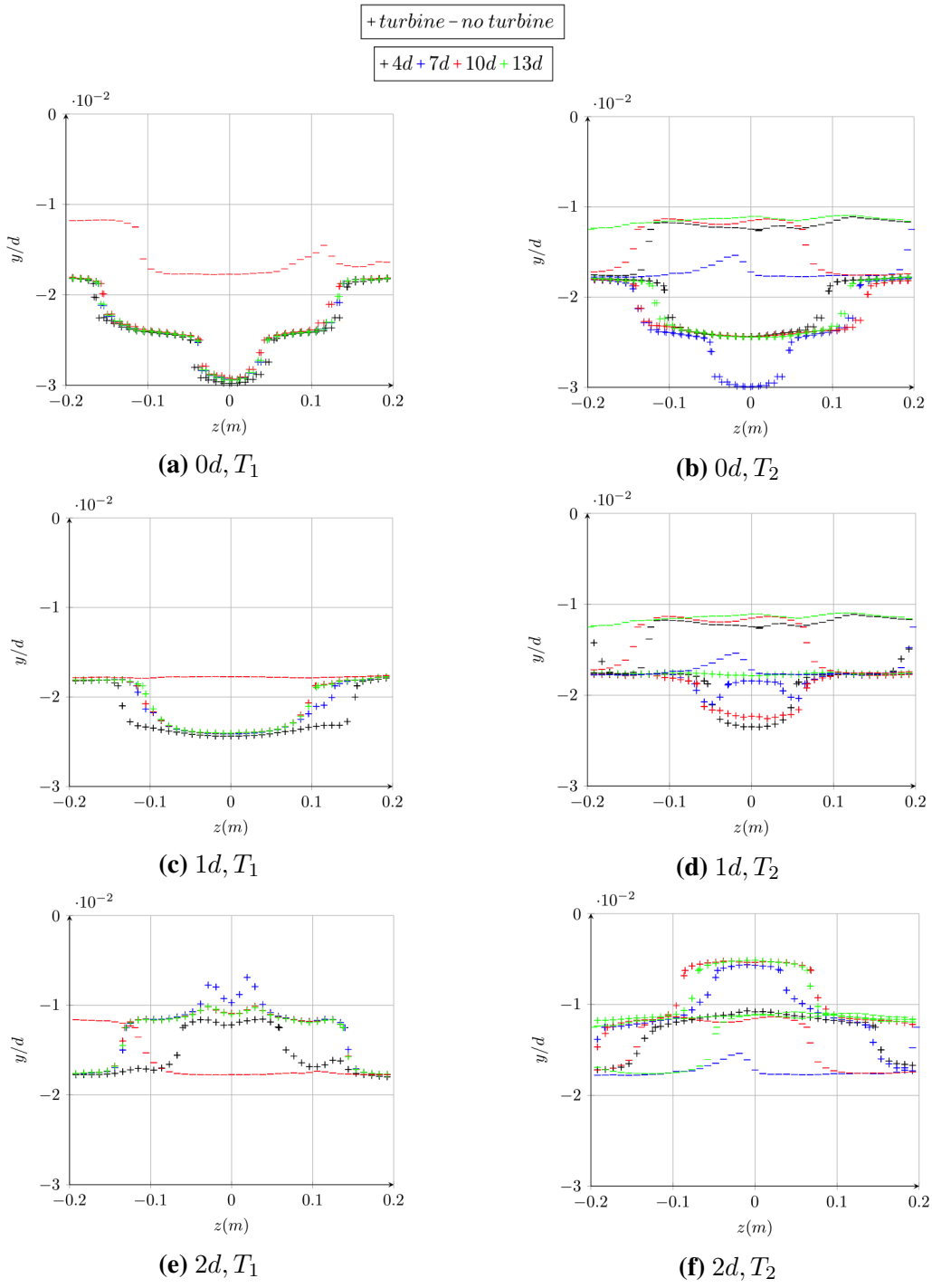

(a) $0d, T_1$ **(b)** $0d, T_2$

(c) $1d, T_1$ **(d)** $1d, T_2$

(e) $2d, T_1$ **(f)** $2d, T_2$

Fig. 6.8: Spatial evolution of the bed elevation at t = 60 s with the turbine (+) and without the turbine (-) at the cross sections of the turbine's position x' (a), x'' (b); (c) and (d): at $1d$ downstream T_1 and T_2 respectively; (e) and (f): at $2d$ downstream T_1 and T_2 respectively; black, blue, red and green colors correspond to the 4d, 7d, 10d and 13d configurations respectively.

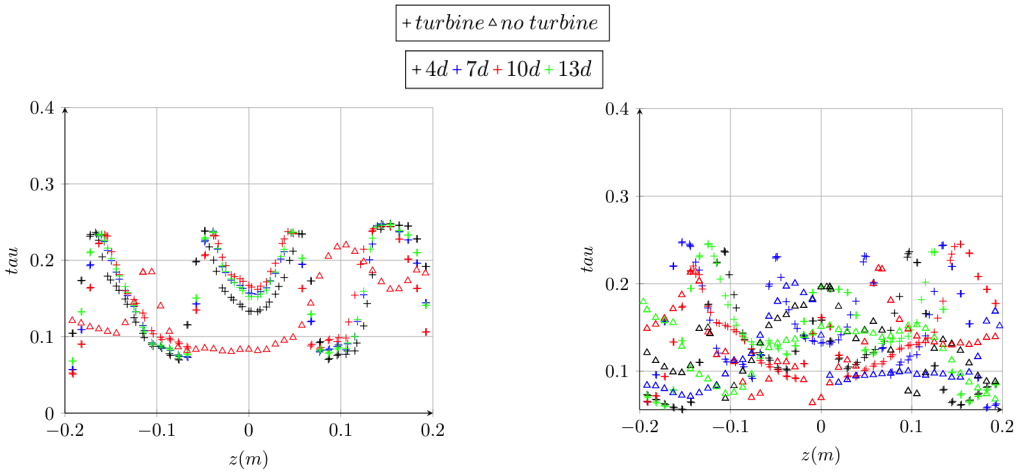

(a) $0d, T_1$ **(b)** $0d, T_2$

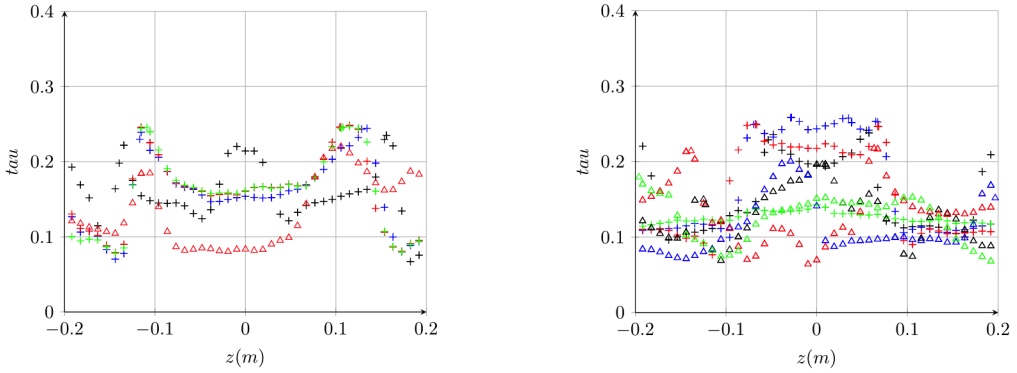

(c) $1d, T_1$ **(d)** $1d, T_2$

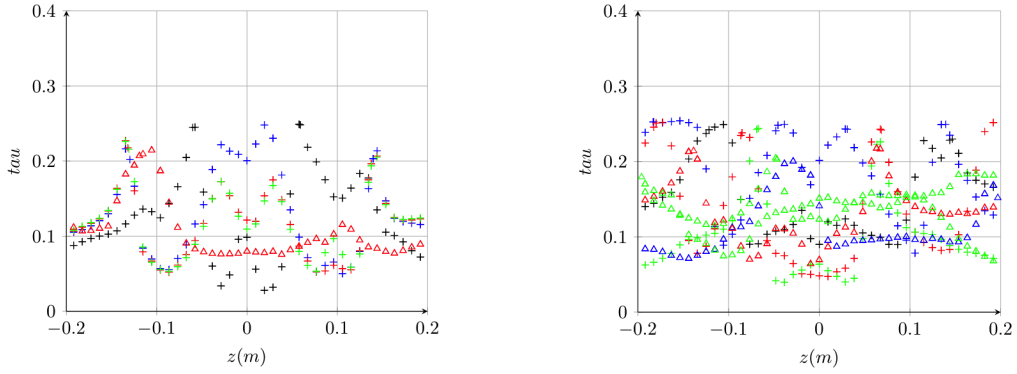

(e) $2d, T_1$ **(f)** $2d, T_2$

Fig. 6.9: Spatial evolution of the shear stress (τ_{yz}) on t = 60 s with the turbine (+) and without the turbine (triangles) at the cross sections of the turbine's position x' (a), x'' (b); (c) and (d): at $1d$ downstream T_1 and T_2 respectively; (e) and (f): at $2d$ downstream T_1 and T_2 respectively; black, blue, red and green colors correspond to the 4d, 7d, 10d and 13d configurations respectively.

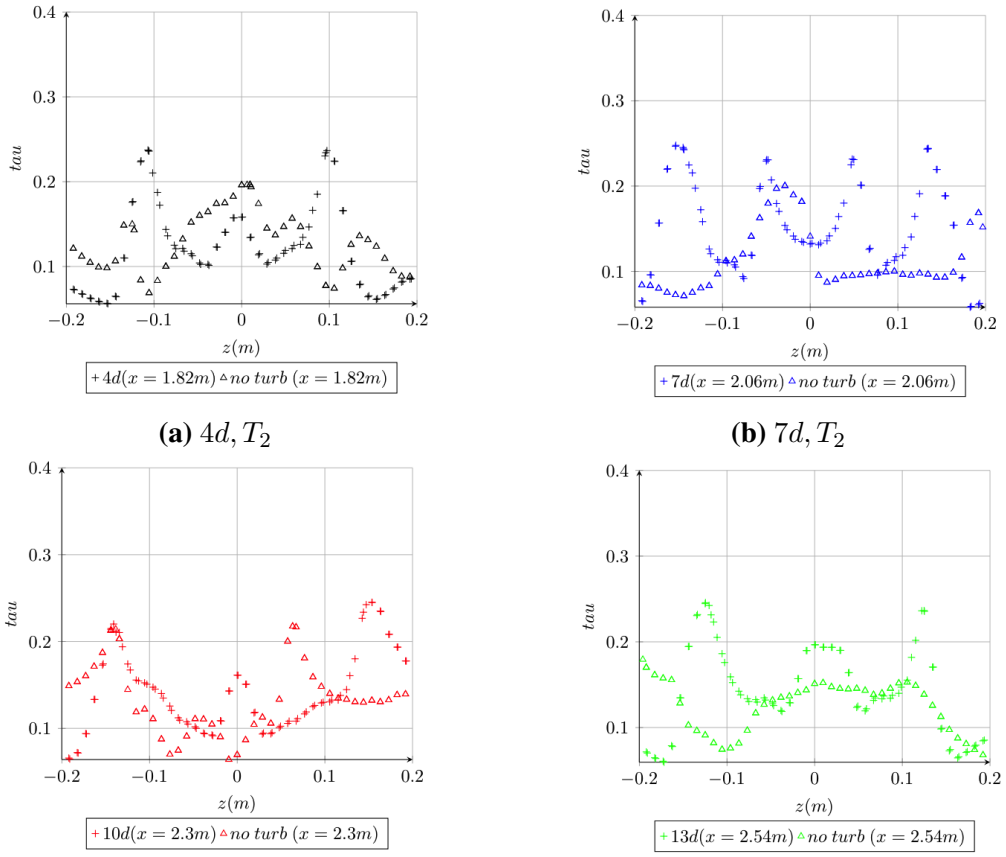

(a) $4d, T_2$ **(b)** $7d, T_2$

(c) $10d, T_1$ **(d)** $13d, T_2$

Fig. 6.10: Spatial evolution of the shear stress (τ_{yz}) on t = 60 s near the second turbine T_2 (+) at the turbine's position $x' = 0d$ for all configurations.

Figure 6.12 compares the evolution of the bed morphology in axial direction with and without the turbines for all configurations. The scour generated below the first turbine is the same for all configurations but after $X = 2d$ the evolution of the bed is widely different between the configurations. This is also shown in fig. 6.11 where different aspects of the bed shear stress are occurred between the turbines throughout the thickness of the sediment bed. However, the bed morphology maintains a cyclic ripples form in the baseline case all along the axis. We notice that the bed in configuration A_2 evolves in a different way downstream the first turbine comparing to other configurations. Its curve presents an important scour at $7d$ and a significant pic between $10d$ and $12d$ downstream the first turbine. However, the curves of other configurations, provide a hollow (scour) under T_2 and a ridge (deposition) downstream its location with the same magnitudes. The farther the second turbine is from the first, the more some ripples are lightly generated between the two turbines, similar to the baseline case. Such as the case of $13d$, there is an attempt to produce a ripple especially at $8d$ downstream the first turbine. This means that the flow at $8d$ begins to recover (fig. 6.3g) and the impact of the first turbine is no

more effective at this position (fig 6.11), otherwise this ripple starts to disappear gradually from $X = 9d$ due to the intervention of the impact of the second turbine. The common point between all the configurations is that the bed is established beyond a distance $4d$ downstream the second turbine, and maintains a constant elevation of $-0.11d$ equal to the pic of the ripples in baseline case. Figure 6.13 shows the difference in dimensionless axial bed elevation between the baseline and turbine results for all configurations. The impact of the turbine in A_2 on the erosion process under its location is the most significant at $7d$.

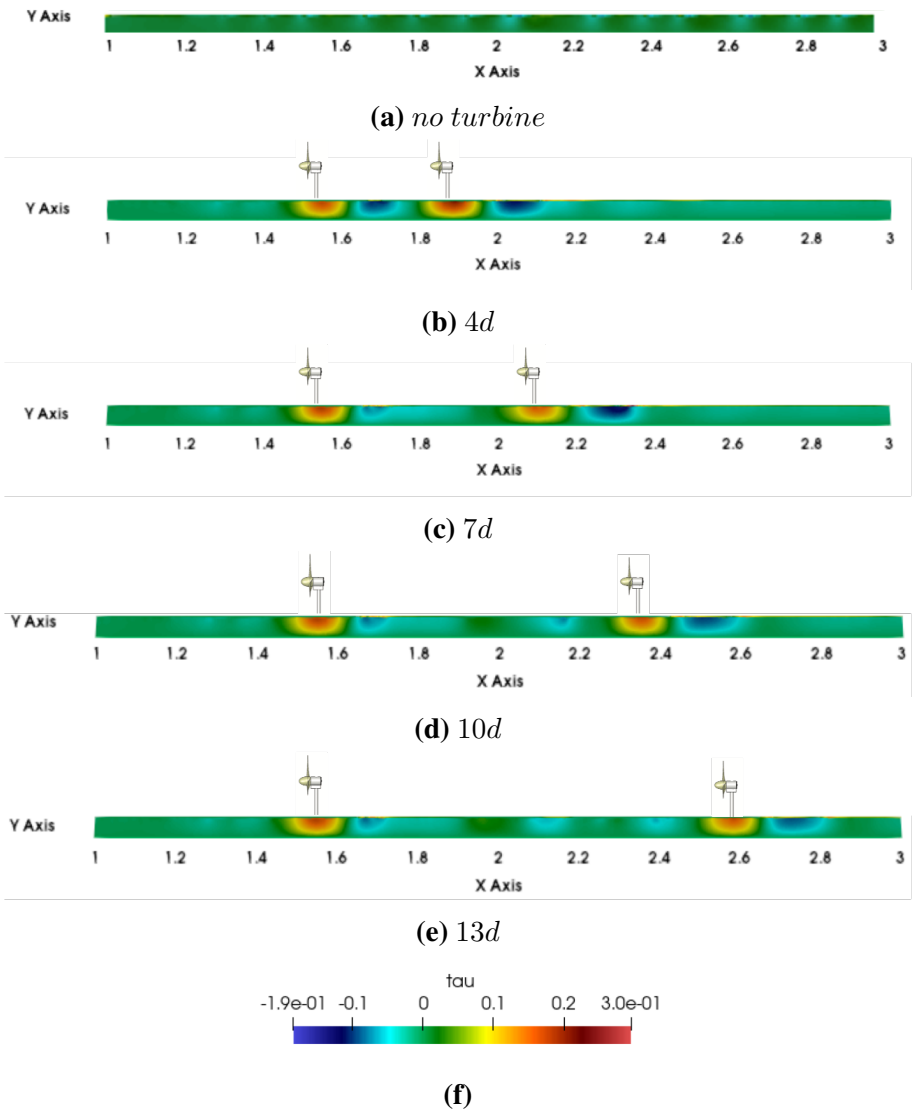

(a) *no turbine*

(b) $4d$

(c) $7d$

(d) $10d$

(e) $13d$

(f)

Fig. 6.11: Spatial evolution of bed elevation with the presence of two turbines apart with different d_i for configurations A_1 (a), A_2 (b), A_3 (c) and A_4 (d).

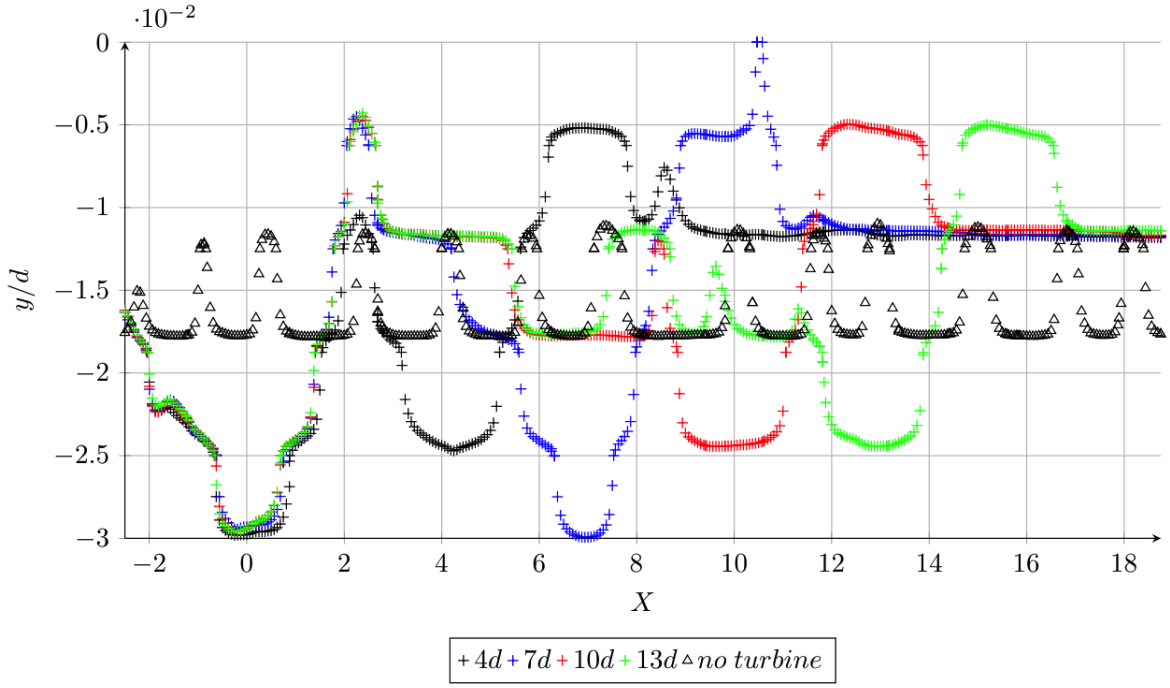

Fig. 6.12: Dimensionless bed elevation along the axis of the channel for the four configurations; d_i = $4d$ (black plus), $7d$ (blue circle), $10d$ (red triangle) and $13d$ (green square) such as $X = (x - x_1)/d$ and x_1 = 1.5 cm.

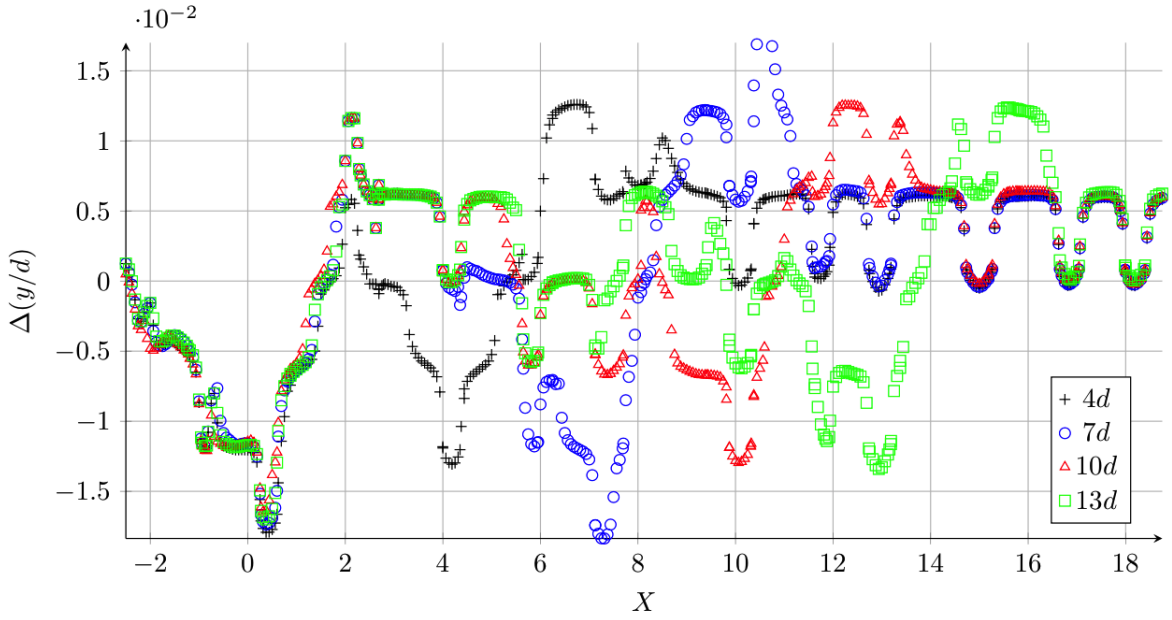

Fig. 6.13: Difference of the dimensionless axial bed elevation between the baseline conditions and the results of presence of the turbine for the four configurations; $d_i = 4d$ (black plus), $7d$ (blue circle), $10d$ (red triangle) and $13d$ (green square) such as $X = (x - x_1)/d$ and $x_1 = 1.5$ cm.

6.4 Summary

In this chapter, we investigated the impact of two interacted turbines on the sediment transport by varying the inter-device distances. The wake interaction between the two turbines is studied first. The wake distribution behind the second turbine is altered by the wake of the upstream turbine, and it is characterized depending on how far it is from the first turbine. Concerning their impact on the sediment transport, a scour is occurred below each turbine for all configurations, and a deposition term is generated behind the turbines regarding the baseline results. The scour is more important under the first turbine since the upstream hydrodynamic conditions are greater than the downstream turbine. Hence, the bed under the second turbine evolves differently between the configurations, the erosion is more pronounced when the inter-distance equals to $7d$ and it is almost similar to the one under the upstream turbine. Results highlight how the interactions between turbines and channel morphology are coupled, and how the presence of single or multiple turbines can influence the local and far-field sediment transport characteristics.

The further the second turbine is located away from the upstream turbine, the more the impact of this latter decreases on the wake distribution of the second, hence the impact of the turbines interaction on the sediment transport is less significant between their locations. Except for the case of d_i = $7d$, the erosion is still important below the second turbine. Thus, it is crucial as perspectives to extend the study and investigate the sensitivity of other inter-distance values in the sediment transport, and reformulate a general conclusion on the relation between the inter-devices distance and the impact of the turbines on sediment transport.

Chapter 7

Conclusions and perspectives

The research program carried out in this thesis aim to couple the 3D Euler multi-phase model CFD approach to a BEMT model of an axial-flow three-bladed hydrokinetic turbine to study the interactions between the turbine and sediment transport of sandy bed. A validation of the different part of the model has been done.

First, the multi-phase theories, based on the Euler-Euler approach, that model the transport of sediments are presented in chapter 2. The SedFOAM code is used in OpenFOAM based on the validation of the litterature. Then, the hydrodynamic models that represent the hydrokinetic turbine, such as the Actuator Disk (AD) and the Blade Element Momentum theories (BEMT) are described, in chapter 3. All developpement have been validated regading the experimental results of Mycek et al. (2014) in terms of performance coefficients and axial velocity distribution in the wake.

These models have been integrated in SedFOAM code. In chapter 4, we verified the capability of the coupled model to study the interaction turbine-sediment by comparing the numerical results with the measurements of Hill et al. (2014) in clear water conditions.

Then, a first study of the erosion of a bottom substrate has been conducted to estimate the impact of the studied turbine on a sandy river bottom as a first application of the coupled model in chapter 5. It allows us to highlight the blockage effect on the mobile sediment bed. The investigation is made by comparing the impact of different blockage ratios on the sediment transport with the presence of the turbine. The energy extracted by the turbine alters the hydrodynamics of the stream by increasing or reducing the friction in areas around the turbines. Close to the turbine, scour phenomena and deposit zones are appearing. The more the turbine is confined, the more its impact on the bottom is less pronounced so the erosion process is less important. This is due to the interaction between the turbine and the walls of the channel that becomes more important when the turbine is more confined, so the vorticity induced by the turbine stills remarkable till the edges of the channel, thus the impact of the turbine on the bottom is not localized under

its position.

Then, a first study of the impact of the distance between two turbines in tandem on the local river has been conducted. The scour is occurred below each turbine for all configurations, however it is more important under the first turbine since the upstream hydrodynamic conditions are greater than the downstream turbine. Hence, the bed under the second turbine evolves differently between the configurations, the erosion is more pronounced when the inter-distance equals to $7d$ and it is almost similar to the one under the upstream turbine. Results show that the local impact of the interacted turbines on the bottom is not as important as the one of the single turbine with the same numerical properties (discussed in the last chapter). Such as the depth of the scour under the single turbine of the configuration A is about $0.084d$, on the other side, the one under the upstream turbine of the configurations A_i[1] is about $0.03d$.

Those morphology changes should have an impact on ecological processes. In the near field, the high levels of transported sediment could affect the surrounding water quality and increase turbidity level by reducing the light penetration in water, the temperature and the aquatic habitat. Moreover, metallic contaminants, in the case of different type of sediments, could be trapped in the sediment bed (Coynel et al., 2016) and be reintroduced in the water column by the erosion of the bed. Large scales morphological evolution has been also considered such as the dunes' migration. It could modify the turbulent boundary layer and cause time-varying turbulent structures. It could then affect human daily activities such as farming (Awang et al., 2017) and can lead to economic losses and damages in long term due to land collapse... To continue development progress, hydrokinetic devices need to operate efficiently in a variety of channel conditions, both with and without mobile substrates, and minimize their impact on the surrounding ecological and morphological environment. Potential implications extend to the design of scour-protection foundation structures, to potential control strategies based on incoming bedforms and on optimal siting for the mitigation of bedform induced unsteady loads. There remains a need for a systematic investigation on turbine-sediment interactions based on the turbine hub height above the sediment layer, and tip-speed ratio, and proximity to the nearest upstream bedform crest location (fig.7.1). Research should investigate these parameters in-depth to gain a better understand on how it effects the mean and variability in turbine performance coefficients, and the turbine near and far-wake velocity deficit. Additionally, these parameters should be further investigated to assess their control on local scour depths and lateral areas of influence. While these studies focused primarily on axial-flow hydrokinetic devices, research should expand to incorporate additional device designs.

The work presented here expands on the limited literature available today on interac-

[1] A_i (i = 1, 2, 3 and 4) designate the four configurations of chapter 6.

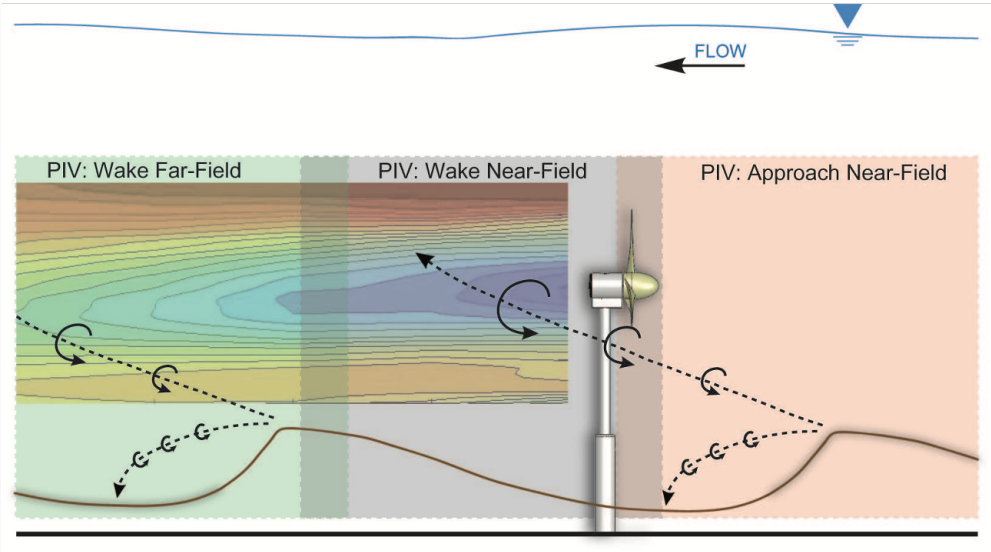

Fig. 7.1: Schematic showing the interactions between dune generated turbulence and axial-flow hydrokinetic turbines (Hill et al., 2014).

tions between hydrokinetic turbines and erodible channels. In particular, the turbine is simulated by two different hydrodynamic models but we did not vary the sediment size for both cases, though it is crucial as a perspetive to study the impact of varying also the sediment diameters. Although results presented within this thesis are from unidirectional flow simulations with relatively large-scale roughness features, they provide an indication of the interactions of hydrokinetic turbines will have in bi-directional (for example tidal) flows with either stationary or mobile substrates containing arbitrarily complex topographic features. The river morphology changes need thorough investigation as any excessive development may also contribute to several impacts. There remains a need for a systematic investigation on turbine-sediment interactions in real scale river application, testing also the impact of displacement of an array of turbines on the transport of sediments like in fig. 7.2.

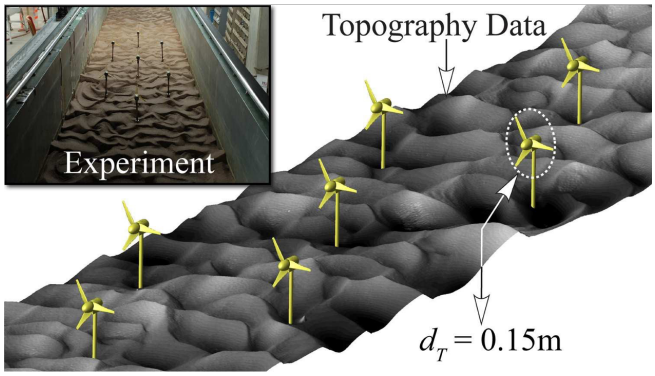

Fig. 7.2: Topography of seven turbine staggered array installed in migrating sand ripple topography ($d50$ = 0.42 mm) (Hill et al., 2014).

Bibliography

U. Ahmed, D. D. Apsley, I. Afgan, T. Stallard, and P. K. Stansby. Fluctuating loads on a tidal turbine due to velocity shear and turbulence: Comparison of cfd with field data. *Renewable Energy*, 112:235–246, 2017. doi: https://doi.org/10.1016/j.renene.2017.05.048.

L. Amoudry, T.-J. Hsu Hsu, and P.-F. Liu. Two-phase model for sand transport in sheet flow regime. *Journal of Geophysical Research*, 113, 2008.

L. O. Amoudry. Extension of $k - \omega$ turbulence closure to two-phase sediment transport modelling : Application to oscillatory sheet flows. *Advances in Water Resources*, 72: 110–121, 2014. doi: https://doi.org/10.1016/j.advwatres.2014.07.006.

D. Apsley, T. Stallard, and K. Stansby. Actuator-line cfd modelling of tidal-stream turbines in arrays. *Journal of Ocean Engineering and Marine Energy*, 4:259–271, 2018. doi: https://doi.org/10.1007/s40722-018-0120-3.

A. Awang, N. Awang, J. Ariffin, M. Razi, and J. Abdullah. Environmental degradation: A review on the potential impact of river morphology. *MATEC Web of Conferences*, 103 (04001), 2017. doi: https://doi.org/10.1051/matecconf/201710304001.

R. A. Bagnold. Experiments on a gravity-free dispersion of large solid spheres in a newtonian fluid under shear. *Phil. Trans. R. Soc. Lond.*, 225:49–63, 1954.

R. Bakhtyar, A. Yeganeh-Bakhtiary, D. A. Barry, and A. Ghaheri. Two-phase hydrodynamic and sediment transport modeling of wave-generated sheet flow. *Advances in Water Resources*, 32(8):1267–1283, 2009. doi: https://doi.org/10.1016/j.advwatres.2009.05.002.

WMJ. Batten, ME Harrison, and AS. Bahaj. Accuracy of the actuator disc-rans approach for predicting the performance and wake of tidal turbines. *Royal Society A*, 371, 2013. doi: https://doi.org/10.1098/rsta.2012.0293.

T. Blackmore, L. E. Myers, , and A. S. Bahaj. Effects of turbulence on tidal turbines : Implications to performance, blade loads, and condition monitoring. *International Journal of Marine Energy*, 14:1–26, 2016.

C. Bonamy, J. Chauchat, Z. Cheng, T. Nagel, and T.J. Hsu. Sedfoam, a openfoam solver for sediment transport. *12th OpenFoam Workshop, Exeter, United Kingdom*, 2017.

F. Boyer, E. Guazzelli, and O. Pouliquen. Unifying suspension and granular rheology. *Physical Review Letter*, 107:188–301, 2011. doi: https://doi.org/10.1103/PhysRevLett.107.188301.

E. Branlard and M. Gaunaa. Development of new tip-loss corrections based on vortex theory and vortex methods. *Journal of Physics Conference Series*, 555, 2014.

J. Capecelatro and O. Desjardins. An euler–lagrange strategy for simulating particle-laden flows. *Journal of Computational Physics*, 238:1–31, 2013.

L.P. Chamorro, D.R. Troolin, and L. Seung-Jae. Three-dimensional flow visualization in the wake of a miniature axial-flow hydrokinetic turbine. *Experiments in Fluids*, 54, 2015.

J. Chauchat and S. Guillou. On turbulence closures for two-phase sediment-laden flows models. *Journal of Geophysical Research*, 113, 2008. doi: https://doi.org/10.1029/2007JC004708.

J. Chauchat and M. Médale. A three-dimensional numerical model for dense granular flows based on the μ (I) rheology. *Journal of Computational Physics*, 256:696–712, 2014. doi: https://doi.org/10.1016/j.jcp.2013.09.004.

J. Chauchat, Z. Cheng, T. Nagel, C. Bonamy, and Hsu T.J. Sedfoam-2.0: a 3-d two-phase flow numerical model for sediment transport, journal of geosci. *Model Dev*, 10:4367–4392, 2017. doi: https://doi.org/10.5194/gmd-10-4367-2017.

S. Chawdhary, C. Hill, X. Yang, M. Guala, D. Corren, J. Colby, , and F. Sotiropoulos. Wake characteristics of a triframe of axial-flow hydrokinetic turbines. *Renewable Energy*, 109:332–345, 2017. doi: https://doi.org/10.1016/j.renene.2017.03.029.

C.P. Chen and P. Wood. A turbulent closure model for dilute gas-particle flows. *The Canadian Journal of Chemical Engineering*, 63:349–360, 1985. doi: https://doi.org/10.1002/cjce.5450630301.

L. Chen and WH. Lam. Methods for predicting seabed scour around marine current turbine. *Renew Sustain Energy Rev*, 29, 2013. doi: https://doi.org/10.1016/j.rser.2013.08.105.

L. Chen and WH. Lam. Slipstream between marine current turbine and seabed. *Energy*, 68:801–810, 2014. doi: https://doi.org/10.1016/j.energy.2014.02.083.

L. Chen, R. Hashim, F. Othman, and S. Motamedi. Experimental study on scour profile of pile-supported horizontal axis tidal current turbine. *Renewable Energy*, 114:744–754, 2017. doi: https://doi.org/10.1016/j.renene.2017.07.026.

Z. Cheng, Hsu T.-J., and J. Calantoni. Sedfoam: A multi- dimensional eulerian two-phase model for sediment transport and its application to momentary bed failure. *Coastal Engineering*, 119:2017, 2016. doi: https://doi.org/10.1016/j.coastaleng.2016.08.007.

Z. Cheng, T.J. Hsu, and J. Calantoni. Sedfoam: A multidimensional eulerian two-phase model for sediment transport and its application to momentary bed failure. *Coastal Engineering*, 119:32–50, 2017.

Z. Cheng, T.-J. Hsu, and J. Chauchat. An eulerian two-phase model for steady sheet flow using large-eddy simulation methodology. *Advances in Water Resources*, 111:205–223, 2018b.

T. Clark, T. Roc, S. Fisher, and N. Minns. Turbulence and turbulent effects in turbine and array engineering. a guide for the tidal power industry. *Turbulence In Marine Environment*, 21, 2015.

C. A. Consul, R. H. J. Willden, and S. C. McIntosh. Blockage effects on the hydrodynamic performance of a marine cross-flow turbine. *Phil Trans R Soc A*, 371:299, 2012. doi: https://doi.org/10.1098/rsta.2012.0299.

A.E. Copping, L.G. Hemery, D.M. Overhus, L. Garavelli, Freeman M.C., J.M. Whiting, A.M. Gorton, H.K. Farr, D.J. Rose, and L.G. Tugade. Potential environmental effects of marine renewable energy development—the state of the science. *Journal of Marine Science and Engineering*, 8:879, 2020. doi: https://doi.org/10.3390/jmse8110879.

A. Coynel, L. Gorse, C. Curti, J. Schafer, C. Grosbois, G. Morelli, E. Ducassou, G. Blanc, and M. Mojtahid. Spatial distribution of trace elements in the surface sediments of a major european estuary (loire estuary, france): Source identification and evaluation of anthropogenic contribution. *Journal of Sea Research*, 118, 2016. doi: https://doi.org/10.1016/j.seares.2016.08.005.

J. Ding and D. Gidaspow. A bubbling fluidization model using kinetic theory of granular flow. *AIChE journal*, 36:523–538, 1990.

Y. El khchine and M. Sriti. Tip loss factor effects on aerodynamic performances of horizontal axis wind turbine. 2017.

S. Elghobashi and W. Arab. A two-equation turbulence model for two-phase flows. *Physics of Fluids*, 26:349–360, 1983. doi: https://doi.org/10.1063/1.864243.

C. Escauriaza and F. Sotiropoulos. Lagrangian model of bed-load transport in turbulent junction flows. *Journal of Fluid Mechanics*, 666:36–76, 2011.

I. Fairley, I. Masters, and H. Karunarathna. The cumulative impact of tidal stream turbine arrays on sediment transport in the pentland firth. *Renewable Energy*, 80:755–769, 2015. doi: https://doi.org/10.1016/j.renene.2015.03.004.

Y. Forterre and O. Pouliquen. Flows of dense granular media. *Annual Review of Fluid Mechanics*, 40:1–24, 2008a. doi: https://doi.org/10.1146/annurev.fluid.40.111406.102142.

Y. Forterre and O. Pouliquen. Flows of dense granular media. *Annual Review of Fluid Mechanics*, 40:1–24, 2008b. doi: https://doi.org/10.1146/annurev.fluid.40.111406.102142.

C. Garrett and P. Cummins. The efficiency of a turbine in a tidal channel. *Journal of Fluid Mechanics*, 588:243–251, 2007. doi: https://doi.org/10.1017/S0022112007007781.

D. Gidaspow. Multiphase flow and fluidization. *Academic Press*, San Diego, 1994.

P. Gillibrand, R. Walters, and J. Mcilvenny. Numerical simulations of the effects of a tidal turbine array on near-bed velocity and local bed shear stress. *Energies*, 9:852, 2016. doi: https://doi.org/10.3390/en9100852.

M. Grondeau, J-C Poirier, S. Guillou, Y. Méar, P. Mercier, and E. Poizot. Modelling the wake of a tidal turbine with upstream turbulence: Lbm-les versus navier-stokes les. *International Marine Energy Journal*, 3(2):83–89, 2020. doi: https://doi.org/10.36688/imej.3.83âĂŘ89.

S. Guillou, J. Thiebot, J. Chauchat, R. Verjus, A. Besq, D. H. Nguyen, and K. Pouv. The filling dynamics of an estuary: From the process to the modelling, book: Sediment transport in aquatic environments. *intech*, 146:307–586, 2011. doi: https://doi.org/10.5772/19933.

C. Hill, M. Musa, L. P. Chamorro, C. Ellis, and M. Guala. Local scour around a model hydrokinetic turbine in an erodible channel. *Journal of Hydraulic Engineering*, 140: 04014037, 2014.

C. Hill, M. Musa, and M. Guala. Interaction between instream axial flow hydrokinetic turbines and unidirectional flow bedforms. *Renewable Energy*, 86:409–421, 2015. doi: https://doi.org/10.1016/j.renene.2015.08.019.

T.J. Hsu, J. Jenkins, and P. Liu. On two-phase sediment transport: Sheet flow of massive particles. *Proceedings of The Royal Society A: Mathematical, Physical and Engineering Sciences*, 460:2223–2250, 2004.

T.-J. Hsu, J. T. Jenkins, and Liu P. L.-F. On two-phase sediment transport: Dilute flow. *Journal of Geophysical Research*, 108(3057), 2003. doi: https://doi.org/10.1029/2001JC001276.

R. Jackson. The dynamics of fluidized particles. *Cambridge University Press*, 2000.

J. T. Jenkins and S. B. Savage. A theory for the rapid flow of identical, smooth, nearly elastic, spherical particles. *Journal of Fluid Mechanics*, 130:187–202, 1983.

C.P. Johnson and R. Jackson. Frictional-collisional constitutive relations for granular materials, with application to plane shearing. *Journal of Fluid Mechanics*, 176:67–93, 1987. doi: https://doi.org/10.1017/S0022112087000570.

K. Kaiser, H. Hohlen, and Langreder W. Turbulence correction for power curves. *Proceedings of European Wind Energy Conference, EWEC, Madrid*, 2003.

F. Khaled, S. Guillou, Y. Méar, and F. Hadri. Impact of blockage ratio on the transport of sediments in the presence of a hydrokinetic turbine: numerical modelling of the interaction sediments-turbine. *International Journal of Sediment Research*, 2021. doi: https://doi.org/10.1016/j.ijsrc.2021.02.003.

W.M. Kranenburg, T.J. Hsu, and J.S. Ribberink. Two-phase modeling of sheet-flow beneath waves and its dependence on grain size and streaming. *Advances in Water Resources*, 72:57–70, 2014. doi: https://doi.org/10.1016/j.advwatres.2014.05.008.

L. Ladokun, B. Sule, K.R Ajao, and N. Adeogun. Resource assessment and feasibility study for the generation of hydrokinetic power in the tailwaters of selected hydropower stations in nigeria. *Water Science*, 32, 2018. doi: https://doi.org/10.1016/j.wsj.2018.05.003.

J. Lawrence, H. Kofoed-Hansen, and C. Chevalier. High-resolution metocean modelling at emec's (uk) marine energy test sites. *Proceedings of the 8th European Wave and Tidal Energy Conference, Uppsala, Sweden*, 2009.

C. Lun. Kinetic theory for granular flow of dense, slightly inelastic,slightly rough spheres, j. *Fluid Mech.*, 233:539–559, 1991.

C. Lun and S. Savage. A simple kinetic theory for granular flow of rough, inelastic, spherical particles. *Journal Applied Mechanics*, 54:47–53, 1987.

A.J. MacLeod, S. Barnes, K. G. Rados, and Bryden I.G. Wake effects in tidal current turbine farms. *Proceedings of IMarEST, Journal of Marine Engineering*, 2002.

F. Maganga. Caractérisation numérique et expérimentale des effets d'interaction entre une hydrolienne et le milieu marin. *Université du Havre*, 2011.

R. Malki, A. J. Williams, T. N. Croft, M. Togneri, and I. Masters. A coupled blade element momentum – computational fluid dynamics model for evaluating tidal stream turbine performance. *Applied Mathematical Modelling*, 37:3006–3020, 2012. doi: https://doi.org/10.1016/j.apm.2012.07.025.

M. Musa, C. Hill, F. Sotiropoulos, and M. Guala. Performance and resilience of hydrokinetic turbine arrays under large migrating fluvial bedforms. *Nature Energy*, 3:839–846, 2018. doi: https://doi.org/10.1038/s41560-018-0218-9.

M. Musa, C. Hill, and M. Guala. Interaction between hydrokinetic turbine wakes and sediment dynamics: array performance and geomorphic effects under different siting strategies and sediment transport conditions. *Renewable Energy*, 138:738–753, 2019. doi: https://doi.org/10.1016/j.renene.2019.02.009.

P. Mycek, B. Gaurier, G. Germain, G. Pinon, and E. Rivoalen. Experimental study of the turbulence intensity effects on marine current turbines behaviour, part i: One single turbine. *Renewable Energy*, 66, 2014. doi: https://doi.org/10.1016/j.renene.2013.12.036.

T. Nagel. Numerical modelling of multi-scale flow-sediment-structure interactions using a multiphase approach. *University of Grenobles Alpes*, 2019.

S. Neill, E. Litt, S. Couch, and A. Davies. The impact of tidal stream turbines on large-scale sediment dynamics. *Renewable Energy*, 34(12):2803–2812, 2009. doi: https://doi.org/10.1016/j.renene.2009.06.015.

V.T. Nguyen. Modélisation de l'interaction entre hydroliennes et le courant dans un courant de marée comme celui du raz blanchard. *Université de Caen*, 2015.

V.T. Nguyen, S. Guillou, J. Thiebot, and A. Santa Cruz. Modelling turbulence with an actuator disk representing a tidal turbine. *Renewable Energy*, 97:625–635, 2016. doi: https://doi.org/1016/j.renene.2016.06.014.

D.L. Nicholas and Brenden P.E. Hydrokinetic energy conversion: Technology, research, and outlook. *Renewable and Sustainable Energy Reviews*, 57:1245–1259, 2016. doi: https://doi.org/10.1016/j.rser.2015.12.189.

T. Nishino and R. H. J. Willden. Effect of 3-d channel blockage and turbulent wake mixing on the limit of power extraction by tidal turbines. *International Journal of Heat Fluid Flow*, pages 123–135, 2012. doi: https://doi.org/10.1016/j.ijheatfluidflow.2012.05.002.

P. Ouro. Large-eddy simulation of tidal turbines. *Renewable and Sustainable Energy Reviews*, 2017. doi: https://doi.org/10.5281/zenodo.1340658.

P. Ouro, R. Luis, and H. Magnus. Analysis of array spacing on tidal stream turbine farm performance using large-eddy simulation. *Journal of Fluids and Structures*, 91, 2019. doi: https://doi.org/10.1016/j.jfluidstructs.2019.102732.

C. Paola and V. R. Voller. A generalized exner equation for sediment mass balance. *Journal Geophysical Research*, 110, 2005.

Antoine Rabain. Scénarii énergétiques et conditions de développement des emr. *Ecole thématique de CNRS, France*, 2019.

R. Ramirez-Mendoza. Laboratory study on the effects of hydro kinetic turbines on hydrodynamics and sediment dynamics, 2018.

H. Rusche. Computational fluid dynamics of dispersed two-phase flows at high phase fractions. *Ph.D. thesis*.

J. Schluntz and R. H. J. Willden. The effect of blockage on tidal turbine rotor design and performance, renewable energy, elsevier. 81:432–441, 2015. doi: https://doi.org/10.1016/j.renene.2015.02.050.

A. Sentchev, M. Thiébaut, and F. Schmitt. Impact of turbulence on power production by a free-stream tidal turbine in real sea conditions. *Renewable Energy*, 147:1932–1940, 2019. doi: https://doi.org/10.1016/j.renene.2019.09.136.

A. Shields. Application of similarity principles and turbulence research to bed-load movement. *California Institute of Technology , Pasadena, CA*, 1936.

A. Srivastava and S. Sundaresan. Analysis of a frictional-kinetic model for gas-particle flow. *Powder Technology*, 129:72–85, 2003.

T. Stallard, R. Collings, T. Feng, and J. Whelan. Interactions between tidal turbine wakes : experimental study of a group of three-bladed rotors. *Philosophical Transactions of the Royal Society A*, 22, 2013.

J. Thiebot, P. Bailly du Bois, and S. Guillou. Numerical modeling of the effect of tidal stream turbines on the hydrodynamics and the sediment transport – application to the alderney race (raz blanchard), france. *Renewable Energy*, 75:356–365, 2015. doi: https://doi.org/10.1016/j.renene.2014.10.021.

M. Uh Zapata, D. Pham Van Bang, and K.D. Nguyen. Parallel simulations for a 2d x/z two-phase flow fluid-solid particle model. *Computers and Fluids*, 2:103–110, 2018. doi: https://doi.org/10.1016/j.compfluid.2018.03.019.

UICN. Development of renewable marine energies and the preservation of biodiversity. *Synthesis for decision-makers, Paris*, 2014.

P. Balachandar Williams and T. R. Bolisetti. Examination of blockage effects on the progression of local scour around a circular cylinder. *Water*, 11(2631), 2019.

J. Q. Xia, R. A. Falconer, and B. Lin. Impact of different tidal renewable energy projects on the hydrodynamic processes in the severn estuary. *UK Ocean Model*, 32:86–104, 2010. doi: https://doi.org/10.1016/j.ocemod.2009.11.002.

X. Yang, A. Khosronejad, and F. Sotiropoulos. Large-eddy simulation of a hydrokinetic turbine mounted on an erodible bed. *Renewable Energy*, 113, 2017. doi: https://doi.org/10.1016/j.renene.2017.07.007.

Annex I

Journaux internationaux

1. Khaled F., Guillou S., Méar Y., Hadri F. (2019), Numerical modelling of the effect of the hydrokinetic turbines on the transport of sediments - Application to the Rhône site, MATEC Web of Conferences, DOI: 10.1051/matecconf/201926105003.

2. Khaled F., Guillou S., Méar Y., Hadri F. (2021), Impact of blockage ratio on the transport of sediments in the presence of a hydrokinetic turbine: numerical modelling of the interaction sediments-turbine, International Journal of Sediment Research (2021, In press) (IF 2.5).

3. Khaled F., Guillou S., Méar Y., Hadri F. (en révision), Numerical Investigation of the local impact of Hydrokinetic turbine on sediment transport - Comparison between two Actuator models, European Journal of Mechanics / B Fluids.

Conférences avec actes

1. Khaled F., Guillou S., Méar Y. and Hadri F., Numerical modelling of the impact of hydrokinetic turbine on the morphology of the near sandy bed, 13th European Wave and Tidal Energy Conference Proceeding, Naple, 1-6 sept. 2019, 8p.

2. Khaled F., Guillou S., Hadri F., Méar Y., Impact of Tidal Stream Turbines on the near sedimentary bed by using an Euler Two-phase modelling CFD approach, 16ième Journées de l'Hydrodynamique, Marseille 27-29 nov. 2018. 10p.

3. Khaled F., Guillou S., Hadri F., Méar Y., Numerical modelling of the effect of the hydrokinetic turbines on the transport of sediments - Application to The Rhone site, 5ième Congrès International Francophone de Mécanique Avancée, Beyrouth, CIFMA, 31/10 au 2/11 2018.

Conférences sans acte

1. Khaled F., Guillou S., Hadri F., Méar Y., Impact of Tidal Stream Turbines on the near sedimentary bed by using a Two-phase modelling CFD approach, 6th International Conference on Estuaries and Coasts, ICEC-2018, 20-23 August 2018, Caen, France, (2018).

2. Khaled F., Guillou S., Méar Y. and Hadri F., Modelling the local impact of hydrokinetic turbine on mobile sandy bed by two-phase Euler-Euler CFD approach, The 4th symposium on two-phase modeling for sediment dynamics in geophysical flows, THESIS-2019, 17-19 sept 2019, Newark, Delaware, USA.

Annex II: French report

7.1 Le besoin d'énergie

La population mondiale est estimée par les Nations Unies (ONU) à $7,6$ milliards en 2017 et devrait atteindre $9,7$ milliards en 2050 (UICN, 2014). Parallèlement, la demande en électricité croît deux fois plus vite que la consommation énergétique globale et devrait augmenter de plus de moitié d'ici 2040. Le défi est de satisfaire cette évolution tout en limitant autant que possible les émissions nocives de gaz à effet de serre. En 2020, les concentrations de dioxyde de carbone présentes dans l'atmosphère ont augmenté de 70 $\%$ par rapport à 2010 à cause de l'utilisation des énergies fossiles. Les différents modèles du Groupe d'Experts sur l'Evolution du Climat (GIEC) prévoient une augmentation de la température moyenne mondiale passant de $1,5$ à plus de $4°$ C d'ici la fin du 21 ème siècle. La conséquence est que le niveau moyen des océans pourrait augmenter d'un mètre au début du 22 ème siècle, ce qui pourrait impacter plus de 270 millions de personnes vivant dans les régions côtières.

Dans un contexte de demande croissante d'énergie et de réduction des émissions de gaz à effet de serre, la population a également besoin d'un air plus sain. Selon l'Organisation Mondiale de la Santé (OMS), les dangers de l'air pollué augmentent, ils estiment qu'environ sept millions de personnes meurent prématurément de la pollution de l'air. Les principales raisons en sont les sources industrielles telles que la production d'électricité et les émissions nocives des moyens de transport, qui pourraient également être évitées par l'utilisation de l'électricité.

Pour résoudre ce dilemme, plusieurs gouvernements se sont engagés. L'objectif est d'exploiter une source d'énergie alternative aux énergies fossiles. L'énergie nucléaire pourrait être une des solutions car elle a un impact mineur sur le réchauffement climatique, mais des préoccupations majeures subsistent sur la sûreté des centrales électriques, le stockage des déchets radioactifs et sa dépendance en uranium.

Dans ce contexte, les Energies Renouvelables (ER) sont au premier plan des préoccupations, ce qui amène les industriels à proposer une grande variété de solutions pour produire des énergies propres. Produites localement, elles limitent ainsi la dépendance

aux transports lointains et importations.

7.2 Energies renouvelables

Les Energies Renouvelables sont issues de processus naturels en perpétuel renouvellement. Actuellement, elles ne représentent que $11,7\%$ de la consommation d'énergie primaire et $17,2\%$ de consommation globale d'énergie en France en 2019 (fig. 1.2). La France s'est donc engagée à diviser par quatre ses émissions de gaz à effet de serre d'ici 2050 et à porter la production d'ER à 40% en 2030.

7.2.1 Types des énergies renouvelables

Il existe plusieurs formes d'ER, dont l'énergie produite par le soleil (photovoltaïque ou thermique), le vent (énergie éolienne), l'eau des rivières et des océans (hydroélectricité), la biomasse qui est solide (bois et déchets d'origine biologique), liquide (biocarburants) ou gazeuse (biogaz) ainsi que la chaleur de la terre (géothermie). Les énergies renouvelables purement électriques comprennent l'énergie hydrocinétique, l'énergie éolienne et le solaire photovoltaïque.

La France est, avec la Suède, l'un des principaux producteurs d'hydroélectricité de l'Union Européenne. En 2019, l'hydroélectricité représentait 51 $\%$ de la production brute d'électricité renouvelable en France. Les Énergies Renouvelables Marines et Fluviales en représentent la majorité dans le secteur de l'hydroélectricité, en raison de leurs nombreux avantages présentés dans la section suivante.

7.2.2 Énergie marine renouvelable (EMR)

L'énergie potentielle des océans est importante. En effet, à l'échelle mondiale, les océans couvrent 71% de la planète. En tant que source d'énergie dérivée localement, l'EMR générée par les vagues et les marées est plus prévisible, cohérente et continue en la comparant aux énergies éolienne et solaire.

À l'échelle mondiale, la puissance cinétique des courants de marée technologiquement exploitables est estimée entre 75 et 100 GW dans les eaux côtières peu profondes bordant le Canada, le Brésil, la Nouvelle-Zélande et le nord de l'Europe. Sur le plateau continental nord-européen, le Royaume-Uni et la France possèdent les sites les plus importants en ressource marémotrice exploitable. Elle est estimée à 11 GW. La France possède une fraction de l'un des plus gros gisements d'Europe, le Raz Blanchard, capitalisant 75% de la ressource potentielle nationale, est situé au centre de la Manche avec une vitesse de courant supérieure à 5 m/s dans des conditions de marée moyenne.

7.2.3 Energie des rivières

Le potentiel énergétique fluvial mondial est d'environ 50 GW. En France, de nombreux cours d'eau présentent des caractéristiques intéressantes pour l'installation de turbines hydrocinétiques. Le potentiel français est d'au moins 254 MW et se situe principalement en Rhône, Nouvelle Aquitaine, Pays de Loire, Bretagne.

Les conditions nécessaires pour installer des turbines hydrocinétiques dans les rivières sont une vitesse d'eau supérieure à $1,5$ m/s et une profondeur d'eau supérieure à un mètre. Pour bénéficier de l'effet de série (production d'énergie importante et réduction des coûts de fabrication), l'objectif est d'installer des parcs de plusieurs machines, parfois plusieurs centaines de machines. En conséquence, l'installation de fermes fluviales nécessitent des rivières à grandes sections et à forts courants.

7.3 Turbines hydrocinétiques

Le fonctionnement d'une turbine hydrocinétique est basé sur un principe similaire à celui des éoliennes. Là où ces dernières captent l'énergie cinétique du vent, les turbines hydrocinétiques utilisent le même processus pour capter l'énergie cinétique des courants de marée et des cours d'eau. La densité de l'eau étant 800 fois plus élevée que celle de l'air, les turbines installées dans les zones à courant fort sont plus petites que les éoliennes de même puissance.

La turbine capte l'énergie du flux d'eau et la transforme en mouvement mécanique qui est lui-même converti en énergie électrique. Les turbines peuvent prendre différentes formes : turbines à axe vertical ou horizontal (fig. 1.5), mais aussi des dispositifs oscillants.

7.4 Interactions avec l'environnement

Améliorer l'endurance des turbines utilisées pour capter des énergies renouvelables hydrocinétiques nécessite d'étudier les interactions entre la turbine et son environnement physique telles que la turbulence ambiante, le transport sédimentaire, les bruits et les vibrations produits par la turbine, ses effets de sillage, ainsi que les effets liés aux interactions entre turbines (effet de confinement).

7.4.1 Interaction turbine-sédiment

La turbine produit un sillage turbulent qui peut être suffisamment important pour perturber la stabilité des sédiments sur le fond marin et ainsi affecter le transport des sédi-

ments que ce soit sur le fond ou en suspension. Cela peut avoir un impact significatif sur la topographie des fonds. La présence de la turbine pourrait accélérer l'écoulement et conduire à un affouillement local (Xia et al., 2010). Pour un grand nombre d'hydroliennes, un effet à longue distance sur le transit des sédiments pourrait perturber les habitats benthiques à plusieurs kilomètres de distance. L'exploration des interactions turbine-sédiments nécessite des recherches intensives sous forme d'expériences, de simulations numériques ou encore de configurations *in situ.*

7.4.2 État de l'art

La modélisation est un outil intéressant pour le développement de l'industrie des turbines hydrocinétiques. Il existe de nombreuses recherches numériques ces dernières années concernant l'impact de la présence de turbines hydrocinétiques de l'échelle du parc à l'échelle régionale.

Le transport des sédiments est modélisé en utilisant une approche classique, comme Thiebot et al. (2015) qui ont modélisé l'effet d'une ferme de turbines sur le transport des sédiments dans le Raz Blanchard en utilisant un modèle hydrodynamique régional 2DH (Thiebot et al., 2015). Ils ont constaté que l'extraction d'énergie des courants de marée a un effet significatif sur le transport sédimentaire à l'échelle régionale. Fairley et al. (2015) ont étudié l'impact cumulatif de la turbine sur le transport des sédiments dans le Pentland Firth. Ils ont conclu que la mise en œuvre du réseau n'a qu'un effet minimal sur la morphodynamique du fond. Gillibrand et al. (2016) ont simulé des fermes de 1, 4 et 57 turbines marémotrices, chacune d'une capacité de 1,5 MW en utilisant un modèle hydrodynamique 3D (RiCOM). L'effet principal observé pour le réseau de 57 turbines est que l'augmentation de la contrainte de cisaillement du fond, conduit à un transport important de sable.

À ce jour, peu d'études existent sur la façon dont les turbines modifient les canaux érodables à l'échelle locale, malgré le fait qu'il soit important de développer une compréhension holistique de la façon dont ces dispositifs affectent tous les aspects de l'environnement physique à l'échelle locale.

7.5 Objectif de la thèse

Le but de ce travail de thèse est de modéliser l'interaction entre une turbine et un fond marin sableux à l'échelle locale. Pour cela nous avons développé des procédures utilisant la théorie des éléments de pales (BEMT) pour représenter l'hydrolienne. Le logiciel open source «OpenFOAM» : (Open Field Operation and Manipulation) est utilisé.

Le premier chapitre contient l'introduction et l'état de l'art sur le sujet.

Le deuxième chapitre s'intéresse aux théories mathématiques utilisées dans l'approche multiphasique d'Euler-Euler. Nous utilisons le module SEDFOAM développé par (Chauchat et al., 2017) à partir du module TwoPhaseEulerFoam.

Les modèles hydrodynamiques liés à la modélisation d'une turbine sont décrits dans le troisième chapitre, comme les modèles Actuator Disk et Blade Element Momentum Theory. L'implémentation des modèles d'interaction, combinant l'approche eulérienne et BEMT, dans OpenFOAM et les outils les plus appropriés pour le code sont sélectionnés. Le code combiné est ensuite validé avec les mesures expérimentales de Mycek et al. (2014) concernant les performances de la turbine et l'expension du sillage.

Au chapitre 4, nous validons le modèle combiné (présenté au chapitre 3) avec des mesures expérimentales issues de Hill et al. (2014) concernant l'effet de la présence de la turbine sur le fond sableux dans des conditions d'eau claire (pas d'érosion sans la turbine).

Le chapitre 5 est considéré comme une première application du modèle combiné, et étudie les effets de blocage sur le transport des sédiments en présence d'une ou de plusieurs turbines.

Au chapitre 6, l'interaction entre deux turbines dans un canal est considérée. En particulier, l'effet sur l'érosion / dépôt à proximité de la turbine, et l'effet global sur le mouvement général des sédiments.

7.6 Méthodologie

Un modèle de transport a été mis en place combinant la théorie des éléments des pales (BEMT) et l'Actuator Disk (AD), qui modélisent les efforts engendrés par les pales de la turbine, avec le modèle multiphasique Euler-Euler pour le transport sédimentaire. Ce modèle est basé sur la plateforme du logiciel OpenFoam.

7.6.1 Modèle multiphasique Euler-Euler

On commence d'abord à présenter les équations utilisées dans le modèle multiphasique développé par 'Imperial College'. Chauchat et al. (2017) et Nagel (2019) ont décrit les différents aspects du modèle et l'ont intégré numériquement dans OpenFOAM en tant que code source appelé 'SedFoam'. Les formules du modèle d'écoulement diphasique eulérien sont obtenues en moyennant des équations locales et instantanées de conservation de la masse et de la quantité de mouvement pour les deux phases fluide et particules

(Hsu et al., 2004). Les équations de conservation de masse sont :

$$\frac{\partial \phi}{\partial t} + \frac{\partial \phi u_i^s}{\partial x_i} = 0 \tag{7.1}$$

$$\frac{\partial (1-\phi)}{\partial t} + \frac{\partial (1-\phi) u_i^f}{\partial x_i} = 0 \tag{7.2}$$

tels que ϕ , et $1-\phi$ sont les fractions volumiques des particules et du fluide respectivement, u_i^s, u_i^f la vitesse des particules et du fluide respectivement, et l'indice i = 1, 2, 3 représente les trois composantes des vecteurs.

Basé sur (Cheng et al., 2017), les équations de conservation du moment pour chaque phase sont :

$$\frac{\partial \rho^s \phi u_i^s}{\partial t} + \frac{\partial \rho^s \phi u_i^s u_j^s}{\partial x_j} = -\phi \frac{\partial p}{\partial x_i} + \phi f_i - \frac{\partial p^s}{\partial x_i} + \frac{\partial \tau_{ij}^s}{\partial x_j} + \phi \rho^s g_i + M_i^{sf} + S_i^f \tag{7.3}$$

$$\begin{aligned} \frac{\partial \rho^f (1-\phi) u_i^f)}{\partial t} + \frac{\partial \rho^f (1-\phi) u_i^f u_j^f}{\partial x_j} = -(1-\phi)\frac{\partial p}{\partial x_i} + (1-\phi) f_i + \frac{\partial \tau_{ij}^f}{\partial x_j} \\ +(1-\phi)\rho^f g_i + M_i^{fs} + S_i^s \end{aligned} \tag{7.4}$$

où ρ^s , ρ^f sont les densités des sédiments et du fluide respectivement, g_i est l'accélération gravitationnelle, f_i la force volumique externe qui entraine l'écoulement, p la pression du fluide. τ_{ij}^f est la contrainte du fluide qui inclus la contrainte visqueuse et contrainte de Reynolds, p^s et τ_{ij}^s sont la contrainte normale et la contrainte de cisaillement respectivement des particules. M_i^{sf} et M_i^{fs} sont les moments de transfert de quantité entre les phases incluant les efforts de la traînée et la vitesse des particules (voir les équations 7.5 and 7.6). S_i^f et S_i^s sont les termes sources représentant les forces hydrodynamiques imposées à l'écoulement par la rotation de la turbine, ils seront décrit dans la section suivante.

$$M_i^{sf} = \phi(1-\phi)K(u_i^f - u_i^s) - \frac{1}{S_c}(1-\phi)K\nu_t^f \frac{\partial \phi}{\partial x_i} \tag{7.5}$$

$$M_i^{fs} = -\phi(1-\phi)K(u_i^f - u_i^s) - \frac{1}{S_c}(1-\phi)K\nu_t^f \frac{\partial \phi}{\partial x_i} \tag{7.6}$$

Les deux termes qui contiennent le paramètre de trainée K et le nombre de Schmidt S_c, représentent le moment de couplage entre les deux phases. ν_t^b est la viscosité turbulente qui est déterminée par un modèle de turbulence comme les modèles URANS à deux

équations $k-\epsilon$, $k-\omega$ and $k-\omega 2006$. Le paramètre de trainée K est modélisé par Schiller et Naumann (1933):

$$K = 0.75 C_d \frac{\rho^f}{d_{eff}} ||u^f - u^s|| \beta^{-h_{Exp}} \tag{7.7}$$

Le coefficient de trainée C_d dépend du nombre de Reynolds des particules $Re_p = (1-\phi) \parallel u^f - u^s \parallel d_{eff}/\nu^f$. Il est calculé par :

$$C_d = \begin{cases} \frac{24}{Re_p}(1 + 0.15 Re_p^{0.687}), & Re_p \leq 1000 \\ 0.44\,, & Re_p > 1000 \end{cases} \tag{7.8}$$

Il existe plusieurs théories dans la littérature qui déterminent les contraintes de cisaillement du fluide ainsi que les contraintes de la phase solide (Chauchat and Guillou, 2008; Bonamy et al., 2017; Cheng et al., 2017; Hsu et al., 2004; Chauchat et al., 2017).

7.6.2 Modèles Hydrodynamiques : BEMT et AD

On commence d'abord par la présentation de la théorie du disque d'action (AD), où le rotor est remplacé par un disque d'épaisseur nulle et de diamètre égal à celui du rotor. Le modèle de Blade Element Momentum Theory (BEMT) permet de déterminer les performances de la turbine ainsi que les forces appliquées par l'écoulement sur la turbine. Les forces volumiques sont calculées en utilisant la théorie des éléments de pale et sont réparties sur un ensemble d'anneaux d'épaisseur radiale dr. Les équations de Navier-Stokes moyennées sont utilisées. La vitesse incidente locale à chaque anneau de la turbine est déterminée ainsi que les forces hydrodynamiques appliquées au disque. Cette simplification est faite pour diminuer le temps et le coût du calcul en diminuant les nombres de noeuds du maillage utilisé.

7.6.2.1 La théorie du disque d'action AD

Le principe est de moyenner les effets induits par la turbine sur un disque qui représente la surface balayée par ses pales lors de sa rotation, et de la répartir sur le volume du disque (fig. 3.1). Ces effets sont représentés par une force volumique (eq. 7.9) en fonction d'une part de l'aire S du disque et d'autre part du saut de pression qui dépend de la vitesse en amont du disque U_∞, de la densité du fluide ρ et du coefficient de poussée C_T.

$$S_i = \frac{\rho K U_d^2}{2e} \tag{7.9}$$

7.6.2.2 La théorie des éléments des pales BEMT

Dans cette théorie, les forces agissant sur un élément de pale d_r sont calculées en utilisant les caractéristiques de portance et de traînée d'un profil bidimensionnel. Ces caractéristiques sont obtenues à partir de l'angle d'attaque déterminé à partir de la vitesse relative de l'écoulement (la vitesse V_r). On considère une turbine à axe horizontal de diamètre 2R avec n' pales, de corde c et d'angle de calage β mesuré entre la ligne de portance nulle du profil et le plan de rotation (fig. 3.3). La vitesse de rotation de la pale est ω, la vitesse amont est V_{axial}. ωr est la vitesse tangentielle de l'élément de pale tandis que les facteurs d'induction axiale a et tangentielle a' sont utilisés pour obtenir la vitesse relative de l'écoulement :

$$V_r = \sqrt{V_{axial}^2(1-a)^2 + r^2\omega^2(1+a')^2} \tag{7.10}$$

L'étude permet d'évaluer les forces hydrodynamiques résultantes de n éléments de pale dans la direction axiale du rayon r :

$$dN = \frac{1}{2}\rho V_r^2 nc(C_x sin\phi + C_z cos\phi)dr \tag{7.11}$$

Le couple appliqué sur les éléments de pale s'écrit :

$$dC = \frac{1}{2}\rho cn(C_z sin\phi - C_x cos\phi)V_r^2 r dr \tag{7.12}$$

Les termes source de quantité de mouvement ajoutés aux équations de quantité de mouvement sont déterminés à partir des forces de portance et de traînée agissant sur chaque pale. Le terme source S_i est projeté par rapport au système de coordonnées cylindriques S_x et S_θ tel que:

$$S_x = -\frac{nf_x}{2\pi re} \tag{7.13}$$

$$S_\theta = -\frac{nf_\theta}{2\pi re} \tag{7.14}$$

7.6.3 Implémentation numérique des modèles et validation.

7.6.3.1 Modèle diphasique

L'implémentation numérique du présent modèle eulérien de transport de sédiments à écoulement diphasique est intégrée par Chauchat et al. (2017) dans un code numérique appelé 'SedFoam' présent dans OpenFOAM. SedFoam est un code multidimensionnel eulérien à deux phases pour la modélisation du transport des sédiments. SedFoam est

développé par un équipe du 'Laboratoire d'Ecoulements Géophysique et Industriel' (France) et du 'Center for Coastal Applied Research' de l'Université du Delaware (USA). SedFoam est basé sur le code twoPhaseEulerFoam (Cheng et al., 2016) et il est compatible avec plusieurs versions d'OpenFOAM (Nagel, 2019). L'implémentation numérique est décrite dans Chauchat et al. (2017).

La capacité du code a été testée sur plusieurs cas de validation à une et deux dimensions dans la littérature (Nagel, 2019).

7.6.3.2 Modèle hydrodynamique

L'implémentation de la théorie des éléments de pales (BEMT) dans OpenFOAM est réalisée via les librairies 'fvOptions' qui consistent à modéliser les efforts hydrodynamiques engendrés par les éléments de la pale du rotor. Des modifications sont apportées au code source 'rotorDiskSourceTemplates.C' pour calculer correctement les forces axiales et tangentielles ainsi que les coefficients de performance.

Le modèle a été validé via les expériences de Mycek et al. (2014) autour d'une seule turbine et réalisées par IFREMER (fig. 3.6). Un accord est obtenu entre les résultats numériques et les mesures expérimentales en terme de coefficient de performance (fig. 3.10) et des caractéristiques du sillage engendré derrière la turbine (voir les profiles de vitesse axiale et d'intensité de turbulence sur la figure 3.13).

7.6.3.3 Couplage entre les deux modèles

Les deux modèles décrits ci-dessus sont couplés pour modéliser l'interaction turbine-sédiment. La théorie de BEMT et le code 'rotorDiskSourceTemplates.C' sont implémentés et compilés numériquement dans le code 'SedFoam'.

Le code combiné a été validé par les expériences de Hill et al. (2015) concernant l'effet local d'une turbine à axe horizontal sur un fond sableux. Une concordance est obtenue entre les résultats numériques et les mesures expérimentales en terme d'affouillement local juste au-dessous de la turbine (fig. 5.4). Une seconde étude a été menée pour comparer l'effet local de la turbine modélisée par le disque d'action simple AD et le disque d'action avec BEMT sur le fond sableux. Les résultats ont montré que l'affouillement induit sous la turbine représenté par BEMT est plus important que celui sous la turbine modélisé par AD (fig. 4.6). Le modèle est utilisé dans ce qui suit pour plusieurs études.

7.7 Effets du confinement sur l'interaction turbine/fond sédimentaire

Six configurations différentes ont été mises en place avec différents rapports de blocage pour déterminer l'effet du confinement sur l'interaction turbine-sédiment. Les tableaux 5.4, 5.2 and 5.3 présentent les propriétés hydrodynamiques et sédimentaires utilisées dans les simulations. L'évolution temporelle (fig. 5.16) et spatiale (fig. 5.17) de l'affouillement au dessous de la turbine sont présentées. Les résultats ont montré un impact significatif du taux de blocage sur l'évolution de la morphologie du fond en aval de la turbine ; plus le rapport est faible, plus l'impact de la turbine dans le sillage proche est plus flagrant. Ces résultats, quoique contre intuitifs, sont en accord avec les résultats expérimentaux de Williams and R. Bolisetti (2019) qui ont analysé l'affouillement autour d'un cylindre. Ils ont étudié l'effet du rapport entre le diamètre du cylindre et la largeur du canal sur l'érosion produite à l'emplacement du cylindre. Les auteurs ont ainsi montré qu'il y a un effet important de la proximité des paroies latérales sur l'érosion du fond sédimentaire et que plus le blocage est fort, plus les parois latérales ont un impact sur l'érosion dans certains cas spécifiques de confinement et de tailles de particules.

7.8 Effet de la distance inter-turbines sur l'évolution du fond sableux

La deuxième application consiste à étudier l'interaction de deux turbines sur le fond sableux. L'étude constitue à simuler quatre configurations, chacune ayant différentes distances inter-turbines. L'interaction de sillage entre les deux turbines est étudiée en premier. La distribution du sillage derrière la deuxième turbine est altérée par le sillage de la turbine amont, et elle est caractérisée en fonction de sa distance par rapport à la première turbine. Un affouillement se produit sous chaque turbine pour toutes les configurations, et un dépôt est généré derrière les turbines. L'affouillement est plus important sous la première turbine puisque les conditions hydrodynamiques en amont sont supérieures à celles de la turbine en aval. Ainsi, le fond sableux sous la deuxième turbine évolue différemment suivant les configurations. L'érosion est plus prononcée lorsque la distance inter-turbine est égale à $7d$ et elle est presque similaire à celle sous la turbine amont (fig. 6.12).

7.9 Conclusion générale et perspectives.

Ce travail de thèse vise à coupler le modèle multiphasique en formulation Euler-Euler à un modèle BEMT d'hydrolienne tripale à écoulement axial pour étudier les interactions entre la turbine et le transport sédimentaire d'un lit sableux.

Les développements ont été réalisés à partir de OpenFOAM. Nous utilisons la librairie SedFOAM pour la prise en compte du transport sédimentaire en formulation à deux phases eau-particules. Les modèles de disques d'action simples et basés sur la théorie des éléments des pales ont été introduit dans le code SedFOAM. Leur validation a été réalisée sur la base d'expériences de la littérature en termes de performances et de distribution de la vitesse axiale dans le sillage.

Ensuite, nous avons vérifié la capacité du modèle couplé à étudier l'interaction turbine-sédiment en comparant les résultats numériques avec les mesures expérimentales de Hill et al. (2014) dans des conditions d'eau claire.

Une première étude a mis en évidence les effets du confinement dans la relation entre la turbine et l'évolution morphologique du lit sableux. L'analyse est faite en comparant l'impact de différents taux de blocage sur le transport des sédiments avec la présence de la turbine. A proximité de l'hydrolienne, des phénomènes d'affouillement et des zones de dépôts apparaissent. Plus la turbine est confinée, moins son impact sur le fond est prononcé donc le processus d'érosion est moins important.

La deuxième étude s'intéresse à l'impact de la distance entre deux turbines placées l'une derrière l'autre sur l'évolution du fond sableux. L'affouillement se produit en dessous de chaque turbine pour toutes les configurations, cependant il est plus important sous la première turbine. Ainsi, le fond sous la deuxième turbine évolue différemment entre les configurations, l'érosion est plus prononcée lorsque la distance inter-turbine est égale à $7d$ et elle est presque similaire à celle sous la turbine amont.

Ces changements morphologiques devraient avoir un impact sur les processus écologiques. A l'échelle locale, les quantités importantes de sédiments transportés pourraient affecter la qualité de l'eau environnante et augmenter le niveau de turbidité en réduisant la pénétration de la lumière dans l'eau et en perturbant l'habitat aquatique.

L'évolution morphologique à grande échelle reste encore à étudier comme la migration des rides qui pourraient modifier la couche limite turbulente et provoquer des structures turbulentes variant dans le temps. Cela pourrait alors affecter les activités humaines quotidiennes (Awang et al., 2017) et peut entraîner des pertes économiques et des dommages à long terme ...

D'autres études sont à réaliser comme la relation entre la turbine et le fond sédimentaire en fonction de la hauteur du moyeu de la turbine, du rapport de vitesse ... (fig.7.1). Les futurs projets de recherche devraient se focaliser sur l'étude de ces paramètres de

manière approfondie pour mieux comprendre comment ils affectent la performance des turbines, ainsi que le déficit de vitesse de sillage proche et lointain de la turbine.

Modélisation de l'interaction hydrolienne et environnement sédimentaire. Utilisation de la méthode Blade Element.

Résumé

Les énergies des courants de marée ou de rivière constituent une alternative aux énergies fossiles. A ce jour, leur développement s'est accéléré même si le passage à l'échelle industrielle semble encore compliqué. L'exploration de l'interaction entre hydrolienne (outils de captation des courants marins ou fluviaux) et fond sédimentaire nécessite des recherches intensives. D'un coté, la présence de la turbine peut modifier la morphologie du fond sableux, et les sédiments, en particulier le sable peut d'un autre coté affecter les pales de la turbine et contribuer à la détérioration de la turbine. Les études numériques sur l'interaction turbine-sédiment à l'échelle locale sont très rares. L'objectif de cette thèse est de modéliser l'impact local de la turbine à axe horizontal sur le fond sédimentaire composé de sable homogène de même taille. Un modèle de transport a été mis en place combinant la théorie des éléments des pales (BEMT) et l'Actuator Disk (AD), qui modélisent les efforts engendrés par les pales de la turbine, avec le modèle multiphasique Euler-Euler pour le transport sédimentaire. Ce modèle est basé sur la plateforme du logiciel OpenFoam. Après une phase de validation des modifications apportées, le code est appliqué à l'étude de diverses configurations des interactions entre une turbine et le fond sédimentaire. Dans un premier temps, une étude de l'effet du confinement sur l'érosion est réalisée. Elle a mis en évidence un phénomène contre intuitif mais corroboré par une expérience (Khaled et al., Sediment Research, 2021). Dans un deuxième temps, nous avons comparé les effets de la modélisation avec le modèle AD simple avec celle du modèle AD-BEMT en termes d'impact sur le fond sableux. Enfin, nous appliquons le modèle à l'étude de l'impact de l'écartement entre deux turbines l'une derrière l'autre sur la dynamique sédimentaire. Cette dernière étude met en évidence une interaction entre la dynamique de génération de rides sous-marines et les effets de sillage des turbines.

Mots clés *: Simulation numérique, Euler-Euler multiphase, turbine hydrocinétique, transport sédimentaire, BEMT, AD, OpenFOAM.*

Modeling of the interactions between turbine and sediment transport, using the Blade Element Momentum Theory.

Abstract

The energies of tidal or river currents constitute an alternative to fossil fuels. So far, their development has accelerated even if the transition to industrial scale still seems complicated. The exploration of the interaction between tidal turbine (tools for capturing marine or river currents) and the sedimentary bottom requires intensive research. On the one hand, the presence of the turbine can modify the morphology of the sandy bottom, in particular sand, on the other hand can affect the blades of the turbine and contribute to the deterioration of the turbine. Numerical studies on the turbine-sediment interaction at the local scale are very rare. The objective of this thesis is to model the local impact of the horizontal axis turbine on the sedimentary bottom composing sand of the same size. A transport model combining blade element theory (BEMT), the Actuator Disk (AD) which models the forces generated by the turbine blades, and the Euler-Euler multiphase model for sediment transport, has been implemented, based on the OpenFoam software platform. After a phase of validation of the modifications made, the code is applied to study various configurations of interaction between a turbine and the sedimentary bottom. First, a study of the effect of confinement on erosion is carried out. She highlighted a phenomenon that is corroborated by an experiment (Khaled et al., Sediment Research, 2021). Secondly, we compared the effects of modeling the turbine by AD model with that of the AD-BEMT model in terms of impact on the sandy bottom. Finally, we apply the model to the study of the impact of the interaction between two turbines one behind the other on the sediment dynamics. This last study highlights an interaction between the dynamics of ripples generation and the wake effects of turbines.

Keywords*: Numerical simulation, Euler-Euler multiphasic, Hydrokinetic turbine, sediment transport, BEMT, AD, OpenFOAM.*